

# Disentangling Carbon Concentration Changes Along Pathways of North Atlantic Subtropical Mode Water

Daan Reijnders<sup>1</sup>, Dorothee C. E. Bakker<sup>2</sup>, and Erik Van Sebille<sup>1</sup>

<sup>1</sup>Utrecht University

<sup>2</sup>University of East Anglia

April 18, 2024

## Abstract

North Atlantic Subtropical Mode Water (NASTMW) serves as a major conduit for dissolved carbon to penetrate into the ocean interior by its wintertime outcropping events. Prior research on NASTMW has concentrated on its physical formation and destruction, as well as Lagrangian pathways and timescales of water into and out of NASTMW. In this study, we examine how dissolved inorganic carbon (DIC) concentrations are modified along Lagrangian pathways of NASTMW on subannual timescales. We introduce Lagrangian parcels into a physical-biogeochemical model and release these parcels annually over two decades. For different pathways into, out of, and within NASTMW, we calculate changes in DIC concentrations along the path ( $\Delta$ DIC), distinguishing contributions from vertical mixing and biogeochemical processes. While the mean  $\Delta$ DIC for parcels that persist within NASTMW in one year is relatively small at  $+6 \mu\text{mol/L}$ , this masks underlying dynamics: individual parcels undergo interspersed DIC depletion and enrichment, spanning several timescales and magnitudes. The strongest  $\Delta$ DIC is during subduction of water parcels ( $+101 \mu\text{mol/L}$  in one year), followed by transport out of NASTMW due to increases in density in water parcels ( $+10 \mu\text{mol/L}$ ). Most DIC enrichment and depletion regimes span timescales of weeks, related to phytoplankton blooms. However, mixing and biogeochemical processes often oppose one another at short timescales, so the largest net DIC changes occur at timescales of more than 30 days. Our new Lagrangian approach complements bulk Eulerian approaches, which average out this underlying complexity, and is relevant to other biogeochemical studies, for example on marine carbon dioxide removal.

1        **Disentangling Carbon Concentration Changes Along**  
2        **Pathways of North Atlantic Subtropical Mode Water**

3                **Daan Reijnders<sup>1</sup>, Dorothee C. E. Bakker<sup>2</sup>, Erik van Sebille<sup>1</sup>**

4        <sup>1</sup>Institute for Marine and Atmospheric research Utrecht, Utrecht University, Utrecht, the Netherlands

5        <sup>2</sup>Centre for Ocean and Atmospheric Sciences, School of Environmental Sciences, University of East  
6                Anglia, Norwich, United Kingdom

7                **Key Points:**

- 8                • Carbon transformations along pathways of North Atlantic Subtropical Mode Wa-  
9                ter are split into mixing and biogeochemical contributions.  
10              • Along paths into, within, and out of this mode water, mixing and biogeochemistry  
11              alter carbon in water parcels over a range of timescales.  
12              • Enrichment is highest during mixed layer subduction, which few parcels undergo  
13              annually; persistence in mode water is the dominant pathway.

---

Corresponding author: Daan Reijnders, [b.j.h.r.reijnders@uu.nl](mailto:b.j.h.r.reijnders@uu.nl)

**Abstract**

North Atlantic Subtropical Mode Water (NASTMW) serves as a major conduit for dissolved carbon to penetrate into the ocean interior by its wintertime outcropping events. Prior research on NASTMW has concentrated on its physical formation and destruction, as well as Lagrangian pathways and timescales of water into and out of NASTMW. In this study, we examine how dissolved inorganic carbon (DIC) concentrations are modified along Lagrangian pathways of NASTMW on subannual timescales. We introduce Lagrangian parcels into a physical-biogeochemical model and release these parcels annually over two decades. For different pathways into, out of, and within NASTMW, we calculate changes in DIC concentrations along the path ( $\Delta$ DIC), distinguishing contributions from vertical mixing and biogeochemical processes. While the mean  $\Delta$ DIC for parcels that persist within NASTMW in one year is relatively small at  $+6 \mu\text{mol L}^{-1}$ , this masks underlying dynamics: individual parcels undergo interspersed DIC depletion and enrichment, spanning several timescales and magnitudes. The strongest  $\Delta$ DIC is during subduction of water parcels ( $+101 \mu\text{mol L}^{-1}$  in one year), followed by transport out of NASTMW due to increases in density in water parcels ( $+10 \mu\text{mol L}^{-1}$ ). Most DIC enrichment and depletion regimes span timescales of weeks, related to phytoplankton blooms. However, mixing and biogeochemical processes often oppose one another at short timescales, so the largest net DIC changes occur at timescales of more than 30 days. Our new Lagrangian approach complements bulk Eulerian approaches, which average out this underlying complexity, and is relevant to other biogeochemical studies, for example on marine carbon dioxide removal.

**Plain Language Summary**

Mode waters are relatively thick water masses with homogeneous properties, such as temperature and salinity. The North Atlantic Subtropical Mode Water (NASTMW), found in the Sargasso Sea, is one such water mass. Lying underneath the ocean surface, it comes into contact with the atmosphere during winter, when the surface layer is vigorously mixed due to strong winds, causing the mixed layer to connect with NASTMW. This way, NASTMW can buffer atmospheric temperature and carbon anomalies during the summer, when there is no surface connection. It is also a conduit for carbon to penetrate beneath the ocean's upper mixed layer, with the potential to sequester it. We study NASTMW from the viewpoint of a water parcel that moves with the currents and see how carbon concentrations in the water parcels change along different NASTMW pathways. For each pathway, the carbon concentration changes due to an interplay of vertical mixing and biogeochemical processes, for example related to plankton growth and decay. These processes can unfold over different timescales and may counteract or enhance themselves or one another. The largest change in carbon concentration is found when a parcel moves from the upper ocean mixed layer into NASTMW, mostly due to vertical mixing.

**1 Introduction**

The ocean is an integral component of the natural carbon cycle, as well as a large sink for anthropogenic carbon emissions. Since 1850, it has taken up 26% of anthropogenic  $\text{CO}_2$  from the atmosphere (Friedlingstein et al., 2022). To understand the ocean carbon sink, now and in the future, it is important to understand how the ocean moves carbon from the upper ocean mixed layer through the permanent thermocline, from where it can be further sequestered on timescales of years, decades, or centuries. A major conduit through which this ocean surface-interior exchange occurs is the North Atlantic Subtropical Mode Water (NASTMW). It links the interior to the surface on an annual basis during winter convective events and is responsible for 20% of the carbon uptake by the solubility pump in the 14–50°N latitude band of the North Atlantic (Bates, 2012).

64 NASTMW, also referred to as Eighteen Degree Water, is a classical example of mode  
65 water (Hanawa & Talley, 2001), featuring a thick vertical layer characterized by near-  
66 homogeneous properties including temperature, salinity, and oxygen concentration. It  
67 has a typical thickness of 200–300 m, located at 300 m depth (Worthington, 1958; Derem-  
68 ble & Dewar, 2013). It is formed during winter, when surface buoyancy loss leads to con-  
69 vection events that deepen the mixed layer in the Sargasso Sea, and through cross-frontal  
70 mixing in the southern flanks of the Gulf Stream (Joyce et al., 2013; Davis et al., 2013).  
71 Spring stratification caps off NASTMW again, causing it to act as an interannual buffer  
72 of wintertime atmospheric anomalies of temperature and carbon (Bates et al., 2002). Gyre  
73 circulation and eddy-induced advection allow NASTMW to spread horizontally south-  
74 wards, causing it to occupy an area much larger than its formation location (Gary et al.,  
75 2014). This makes NASTMW also a key regulator of temperature (Sugimoto et al., 2017),  
76 organic carbon (Sugimoto et al., 2017), and nutrients (Palter et al., 2005) in the inte-  
77 rior of the subtropical gyre. Subsequent destruction of NASTMW occurs primarily through  
78 vertical mixing at the top of the layer, but also through diapycnal mixing and along-isopycnal  
79 stirring (Billheimer & Talley, 2016).

80 Current understanding of the role of NASTMW in oceanic carbon uptake is either  
81 based on sparse observations (Bates et al., 2002; Bates, 2012; Billheimer et al., 2021) or  
82 is inferred from insights into physical mechanisms such as its formation, ventilation and  
83 pathways (Davis et al., 2013; Gary et al., 2014; Kwon et al., 2015; Li et al., 2022; Gan  
84 et al., 2023). However, a process-based view of how dissolved inorganic carbon (DIC)  
85 is transported along pathways from the ocean surface through NASTMW into the ocean  
86 interior is lacking.

87 We investigate how DIC concentrations change along pathways of NASTMW dur-  
88 ing its formation, persistence, ventilation, and physical export to higher-density water  
89 masses to better understand which processes alter carbon concentrations along this con-  
90 duct between the atmosphere and the ocean interior. To do so, we trace virtual parcels  
91 of water along pathways into, out of, and within NASTMW using a coupled physical-  
92 biogeochemical, eddy-permitting ocean model. Along the pathways of these flow-following  
93 Lagrangian parcels, we disentangle the influence of different vertical mixing and biogeo-  
94 chemical processes on the local DIC concentration. Specifically, we split biogeochemi-  
95 cal processes into soft-tissue and carbonate components. We then quantify the timescales  
96 and magnitudes of DIC depletion and enrichment regimes, defined between local min-  
97 ima and maxima in DIC anomaly time series. Rather than only looking at the bulk change  
98 in DIC concentrations along each pathway, we also consider how these changes are dis-  
99 tributed between processes and pathways, as well as in time and between a range of timescales.  
100 This allows us to better understand the complexity by which vertical mixing and bio-  
101 geochemical processes affect the DIC content of NASTMW at different moments and timescales.

102 We focus on timescales of the order of years and less, as observations and model-  
103 ing studies show that most NASTMW parcels have residence times shorter than a year  
104 (Fratantoni et al., 2013; Gary et al., 2014). We consider parcels that subduct into NASTMW,  
105 ventilating parcels, persisting NASTMW parcels, and parcels that are exported due to  
106 increases in density. Parcels in this last class are relevant candidates for longer seques-  
107 tration on timescales of years to decades (the timescale of the gyre interior; Levine et  
108 al., 2011).

## 2 Data and Methods

### 2.1 Ocean Model Data

To compute Lagrangian parcel trajectories and along-trajectory DIC changes, we use gridded ocean physics and biogeochemistry output data from a global hindcast ocean model at  $1/4^\circ$  horizontal resolution, comprised of the FREEGLORYS2V4 physics and FREEBIORYS2V4 biogeochemistry products developed by Mercator Ocean International (MOi) for the Copernicus Marine Service. These coupled products have an eddy-permitting resolution, resolving part of the mesoscale eddy regime, which plays a role in mode water formation (Xu et al., 2014; Davis et al., 2013). Ideally, we would use a model set that resolves the full mesoscale, to better represent NASTMW (Gan et al., 2023), or even parts of the submesoscale, as these play important roles in biogeochemical cycles (Lévy et al., 2024). However, an eddy-permitting resolution accommodates the high computational and storage demands from the physical-biogeochemical run (similar to Atkins et al., 2022), and can provide us with a mesoscale process-level understanding. The horizontal resolution of  $1/4^\circ$  is representative of that used in state-of-the-art earth system models (Hewitt et al., 2020), and thus also bears relevance to their dynamics. We use versions of both data products on their native Arakawa C-grid, allowing for more precise Lagrangian trajectory computations (Delandmeter & van Sebille, 2019).

Ocean physics obeys conservation of mass, momentum, and biogeochemical budgets and the hindcast ocean model does not include data assimilation. We use a time series between 1995 and 2017, excluding earlier spin-up years. The length of the time series allows us to take into account interannual variability. Since the model is not constrained by observations after its initialization, it may exhibit drift from observed conditions over time. Thus, we use the model in the context of process understanding rather than precise reproduction of observational data.

Ocean physics in FREEGLORYS2V4 are simulated with NEMO version 3.1 (Madec et al., 2013) with the ORCA025 configuration, having a 22 km horizontal resolution at Cape Hatteras and 75 vertical levels (Bernard et al., 2006). Vertical mixing is parameterized using an adaptation of the turbulent closure model by Blanke and Delecluse (1993). Physics are initialized from the EN4 data product (Good et al., 2013) and atmospheric forcings come from 3-hourly ERA-interim reanalysis products from ECMWF (Dee et al., 2011). FREEGLORYS2V4 has an assimilated counterpart, GLORYS2V4, which is extensively described in Garric and Parent (2017). A comparison of the model with observations is found in Supporting Information (SI) Text S1.

Biogeochemistry in FREEBIORYS2V4 is modeled using the intermediate complexity PISCES-v2 model (Aumont et al., 2015). PISCES simulates the carbon cycle, carbonate chemistry, main nutrients (P, N, Fe, and Si), and the lower trophic levels of marine ecosystems (phytoplankton, microzooplankton, and mesozooplankton) using 24 prognostic variables in total. These tracers are advected and vertically mixed using the hydrodynamics from FREEGLORYS2V4, without horizontal diffusive mixing. Nitrate, phosphate, oxygen, and silicate are initialized using data from the World Ocean Atlas (National Oceanographic Data Center (U.S.) Ocean Climate Laboratory et al., 2002) and DIC and alkalinity are initialized with the GLODAP climatology (Key et al., 2004). The model includes atmospheric deposition and riverine input of Fe, Si, N and P, as well as Fe input from sediment. Although PISCES-v2 imposes a stoichiometric ratio of C:N:P = 122:16:1, cycles of phosphorus and nitrogen are different due to nitrogen fixation, denitrification, and differences in atmospheric deposition of N and P. Atmospheric  $p\text{CO}_2$  is prescribed at the air-sea interface, computed from monthly global  $\text{CO}_2$  mole fractions (Lan et al., 2023). A biogeochemical model verification at the global scale is found Perruche et al. (2019).

159 Near the Bermuda Atlantic Time-series Study (BATS) site ( $32^{\circ}10'N$ ,  $64^{\circ}10'$ ) FREE-  
 160 BIORYS2V4 exhibits a trend of increasing salinity-normalized DIC at 10 m depth, by  
 161  $+0.2 \mu\text{mol/L/year}$  (SI Fig. S12). This is roughly a factor 5 smaller than the observed  
 162 salinity-normalized DIC trend of  $+1.08 \pm 0.05 \mu\text{mol/kg/year}$  (Bates et al., 2012). There-  
 163 fore, the input of the biogeochemical model does not accurately represent the observed  
 164 decadal increase of upper ocean DIC concentrations due to climate change in the Sar-  
 165 gasso Sea. We thus only consider the two decades of model data in the context of inter-  
 166 annual variability and focus on a process-based understanding of DIC changes along NASTMW  
 167 pathways. Due to a bias in the model upper ocean salinity trend, the DIC trend at the  
 168 surface of the Sargasso Sea is mostly between 0 and  $-1 \mu\text{mol/L/year}$  (SI Text S1), which  
 169 is small compared to the high background DIC concentrations of  $\sim 2055 \mu\text{mol L}^{-1}$ .

## 170 2.2 Definition of NASTMW

171 NASTMW was first identified by Worthington (1958) as a water mass with a uni-  
 172 form temperature around  $18^{\circ}\text{C}$ , giving it the moniker Eighteen Degree Water. It is most  
 173 commonly classified using a temperature range centered around  $18^{\circ}\text{C}$ , typically  $17\text{--}19^{\circ}\text{C}$   
 174 (Kwon & Riser, 2004; Maze et al., 2009; Forget et al., 2011), with an added stratifica-  
 175 tion constraint that delineates the vertical homogeneity of mode water (Klein & Hogg,  
 176 1996; Kwon & Riser, 2004). Alternatively, it is defined through a potential density range  
 177 with a threshold to delimit low potential vorticity (PV) (Talley & Raymer, 1982; Bill-  
 178 heimer & Talley, 2016).

179 We choose the following constraints for marking Lagrangian parcels as part of NASTMW:

- 180 1. Temperature at the location of the parcels is bounded between  $17\text{--}20.5^{\circ}\text{C}$ . The  
 181 upper bound is higher than the typical  $19^{\circ}\text{C}$ , since the temperature stratification  
 182 is slightly stronger in the NASTMW region in the model than in observations, due  
 183 to model biases (see SI Text S1), similar to the model study of Gary et al. (2014).
- 184 2. The local temperature stratification  $\partial T/\partial z$  is smaller than  $0.01^{\circ}\text{C m}^{-1}$ . This strat-  
 185 ification limit is weaker than the constraint of  $\partial T/\partial z < 0.006^{\circ}\text{C m}^{-1}$  stratifi-  
 186 cation of Kwon and Riser (2004), but the same as in Gary et al. (2014).
- 187 3. Parcels reside in NASTMW layers of at least 50 m thickness, to exclude thin mixed  
 188 layers
- 189 4. Parcels reside in a contiguous volume of NASTMW of at least  $1 \times 10^{11} \text{ m}^3$ . While  
 190 this is only on the order of  $10^{-4}$  times the typical winter NASTMW volume, it  
 191 excludes many small volumes that are shed off from the main NASTMW volume.
- 192 5. We only consider NASTMW west of  $35^{\circ}\text{W}$ , to exclude Madeira Mode Water, which  
 193 has similar properties to NASTMW (Siedler et al., 1987).

194 Constraints 1–3 are similar to those used in Gary et al. (2014) and Kwon et al. (2015),  
 195 who also investigate Lagrangian pathways of NASTMW in an ocean model, except that  
 196 they use a slightly lower temperature upper bound of  $20^{\circ}\text{C}$ . A sensitivity analysis of the  
 197 NASTMW constraints is found in SI Text S2. With the constraints used, we find an av-  
 198 erage yearly maximum volume of  $9.0 \times 10^{14} \text{ m}^3$ , close to the NASTMW volume of  $9.1 \times$   
 199  $10^{14} \text{ m}^3$  found by Joyce (2012) based on observations (SI Text S2). Although the vol-  
 200 ume of NASTMW exhibits strong seasonal and interannual variability, we find a strong  
 201 decrease in NASTMW volume starting in 2010, which agrees with the observed decrease  
 202 in mode water formation found by Stevens et al. (2020).

203 Figure 1 shows March and September snapshots of modeled NASTMW thicknesses  
 204 defined using the above criteria. The imprint of mesoscale eddies on the NASTMW struc-  
 205 ture can be clearly observed (Fratantoni et al., 2013; Gary et al., 2014). Due to model  
 206 biases, the modeled NASTMW has its core located farther eastward with respect to ob-  
 207 servations (SI Text S1), but the modeled NASTMW is used here to gain a process-level  
 208 understanding of how DIC concentrations change along NASTMW pathways.

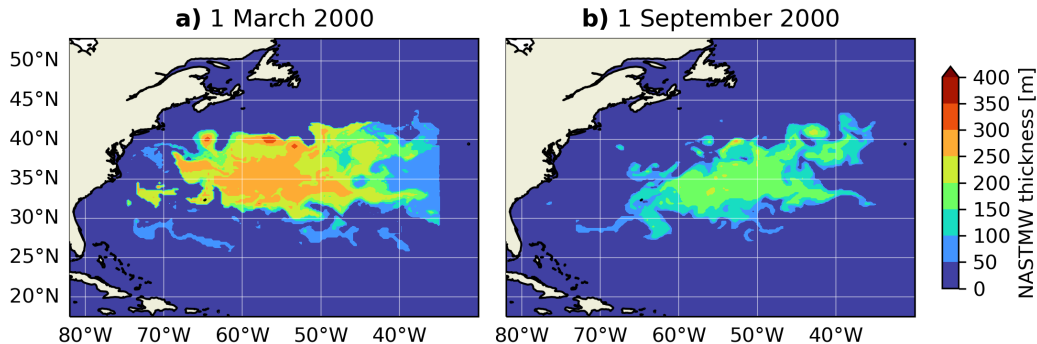


**Figure 1.** Modeled NASTMW thickness snapshots on (a) 1 March 2000, and (b) 1 September 2000. Note that Madeira Mode Water, east of 35°W, is excluded.

209

### 2.3 Initialization and Simulation of Lagrangian Parcels

210

211

212

213

214

215

216

217

218

219

To compute DIC changes along Lagrangian pathways, we simulate the movement of virtual Lagrangian parcels using the Parcels Lagrangian framework (Delandmeter & van Sebille, 2019) (version 2.4.1). These Lagrangian parcels have no defined size and behave like point particles that are advected using ocean model output velocities, while tracer concentrations are equal to those of the ambient water. Along the Lagrangian pathways, we sample molar concentrations of DIC and its precomputed vertical mixing flux, as well as alkalinity, nitrate, phosphate, and their mixing fluxes (section 2.5). We also sample temperature, salinity, mixed and mixing layer depth, and NASTMW criteria (stratification and contiguity criteria) as these help us distinguish the different NASTMW pathways.

220

221

222

223

224

225

We homogeneously initialize parcels in all parts of NASTMW yearly on 1 September between 1995 and 2015, using the criteria of section 2.2. Parcels are horizontally spaced apart 0.25° in the zonal and meridional directions, matching the horizontal model resolution. Vertically, parcels are released at fixed depths in NASTMW at 30 m intervals starting at 100 m and reaching down to 460 m (the minimum and maximum summer NASTMW depths in the model).

226

227

228

229

230

231

232

233

234

235

236

237

238

239

240

Parcels are advected forward and backward in time: forward simulations serve to investigate ventilating parcels, persisting NASTMW parcels, and parcels that are exported due to increases in water density. Backward simulations allow us to investigate which parcels have subducted from the mixed layer since the previous summer. Simulations use time steps of  $\Delta t = 90$  minutes. For maximum velocities of the order  $\sim 1 \text{ m s}^{-1}$  and a nominal grid resolution of 20 km, this is well below the limit of  $\Delta t = \Delta x / U = 6$  hours during which a parcel may travel distances at the grid scale. Parcels are simulated for 3 years, although for most of the analysis in this study, we use only the first year of integration data. Parcel locations and biogeochemical concentrations are saved at daily intervals. In total, we simulate a total of  $2 \times 861,164$  trajectories ( $2 \times 20,504 \pm 6,487$  per year, depending on the NASTMW volume), with the factor 2 indicating forward and backward trajectories. The parcel spacing and temporal output are chosen to balance statistical accuracy with the large computational and storage demands from sampling many biogeochemical fields and identifying individual DIC enrichment and depletion regimes (see section 2.6).

241

242

243

Parcel trajectories are computed without adding any stochastic displacements that simulate vertical mixing or subgrid-scale isoneutral dispersion (Reijnders et al., 2022). Instead, the parcels represent the (grid-scale) mean flow. We can then see how subgrid-

244 scale vertical mixing fluxes, which are sampled at parcel locations, influence carbon con-  
 245 centrations at the larger grid-scale.

## 246 2.4 NASTMW Pathway Definition

247 Parcels may enter and exit NASTMW at infinite points in space and time. We de-  
 248 lineate four specific pathways into, within, and out of NASTMW that are typical to its  
 249 life cycle. Rather than accounting for all possible NASTMW pathways, our study focuses  
 250 on DIC transformations along these characteristic pathways, acknowledging their poten-  
 251 tial overlap and non-exhaustiveness. To determine which pathway a parcel follows, we  
 252 use the daily output snapshots of the parcel trajectory computation. We restrict our-  
 253 selves to pathways starting on 1 September, as this date coincides with a low NASTMW  
 254 volume and ensures that the NASTMW maximum in March occurs midway through our  
 255 simulations. Figure 2 shows the four pathways used in this study. They are defined as  
 256 follows:

- 257 1. *Subduction*: Parcels were in the mixed layer on 1 September in the previous year  
 258 and end up in NASTMW on the following 1 September. Here, the mixed layer in  
 259 NEMO is defined as the layer where the temperature is within  $0.2^\circ\text{C}$  of the tem-  
 260 perature at 10 m depth. We use the mixed layer rather than the mixing layer (Brainerd  
 261 & Gregg, 1995) since it is sufficient that a parcel has recently been mixed in sum-  
 262 mer. Relatively few parcels are expected to subduct on timescales of a year. How-  
 263 ever, using a longer time scale allows parcels to travel larger horizontal distances,  
 264 thus widening the domain of parcel origin, possibly far beyond the NASTMW for-  
 265 mation region. We opt for specifically investigating short subduction time scales  
 266 of 1 year in order to keep the parcel origin close to the NASTMW region. SI Text  
 267 S3 discusses results using longer subduction timescales of two and three years.
- 268 2. *Persistence*: Parcels persist in NASTMW throughout the year until next Septem-  
 269 ber. If a parcel temporarily exits the NASTMW—for instance, for a duration shorter  
 270 than the interval between two consecutive daily snapshots—and then re-enters,  
 271 it is still considered to have persisted, provided it is in NASTMW at all daily snap-  
 272 shots.
- 273 3. *Ventilation*: Parcels from September NASTMW at one point reach the mixing layer,  
 274 defined by the turbocline depth, and are present in NASTMW again next Septem-  
 275 ber. The turbocline depth in NEMO is computed by a transition in vertical mix-  
 276 ing regimes, where the vertical eddy diffusivity drops below a predefined thresh-  
 277 old (Madec et al., 2013). Air-sea heat and carbon fluxes act in the model’s up-  
 278 per layer and propagate by vertical mixing throughout the mixing layer. Note that  
 279 the mixing layer can partially overlap with NASTMW. A portion of persisting NASTMW  
 280 parcels may thus ventilate as well, meaning parcels may be double-counted.
- 281 4. *Export*: Parcels leave NASTMW and acquire a potential density that is higher than  
 282 their last value within NASTMW ( $\sigma > \sigma_{\text{NASTMW}}$ ). Leaving NASTMW can thus  
 283 also be the result of not meeting the stratification criterion anymore when NASTMW  
 284 is destroyed. We are particularly interested in parcels that persistently maintain  
 285 their higher densities for a full year, to exclude parcels that only densify temporar-  
 286 ily. Since not all parcels will densify immediately when the simulation starts, we  
 287 here require that parcels have been densified out of NASTMW for at least a con-  
 288 tinuous year, two years after their initialization. We view these parcels as candi-  
 289 dates for sequestration since they represent previous NASTMW parcels that are  
 290 transformed and exported to higher-density waters. When parcels leave NASTMW,  
 291 their densities may undergo slightly negative fluctuations. We relax the criterion  
 292 slightly to allow for this:  $\sigma > \sigma_{\text{NASTMW}} - \Delta\sigma$ , with  $\Delta\sigma = 0.01 \text{ kg m}^{-3}$ .  $\sigma$  is  
 293 computed using TEOS-10 (McDougall & Barker, 2011). We discuss variations of  
 294  $\Delta\sigma$  in SI Text S4.

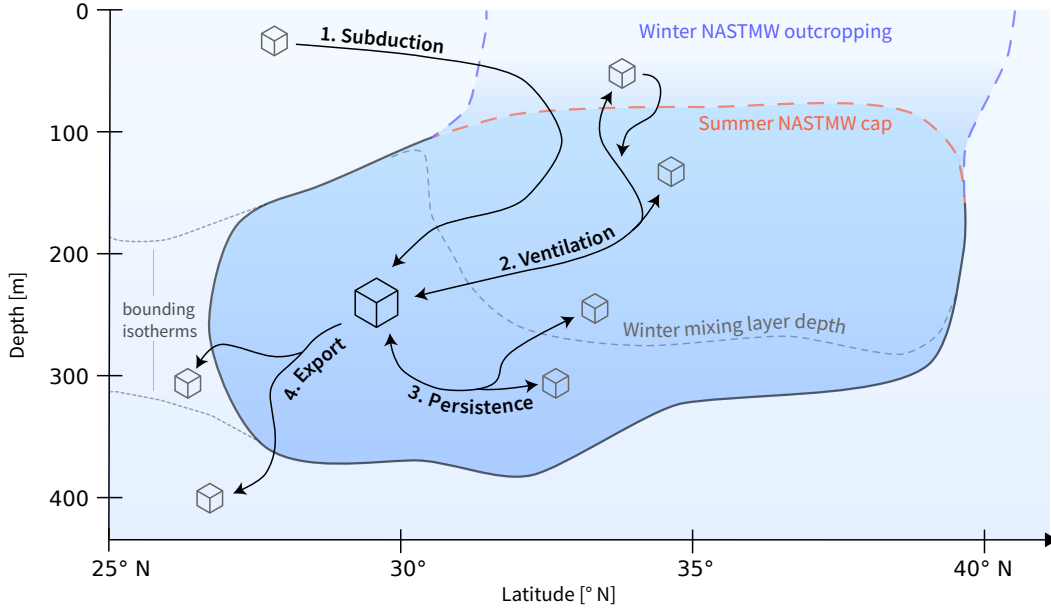


**Figure 2.** Sketch of the four Lagrangian pathways in, within, and out of NASTMW as covered in this study in latitude-depth space. NASTMW is indicated by the dark blue blob. Actual NASTMW boundaries and outcropping locations also exhibit longitudinal, seasonal, and interannual variation.

295 Note that we focus on the total, time-integrated, change in DIC along a Lagrangian  
 296 pathway, indicated by  $\Delta$ DIC, and on timescale distributions of DIC concentration changes  
 297 along these pathways. The Lagrangian pathways of NASTMW parcels have already been  
 298 extensively described from a physical perspective by Gary et al. (2014) and Kwon et al.  
 299 (2015).

300 As mentioned, the above four pathways are not exhaustive. For example, between  
 301 consecutive summers a parcel may temporarily leave NASTMW for a few days without  
 302 reaching the mixing layer. Such a parcel would not fall into any of the above categories.  
 303 Other examples are parcels that densify but do not remain denser than their NASTMW  
 304 exit density for a full year or parcels that subduct over timescales longer than one year.  
 305 However, the clear definitions of the four pathways in this study helps create a process-  
 306 based understanding of carbon fluctuations throughout the life cycle of NASTMW.

## 307 2.5 Disentangling DIC Changes

308 The total change in DIC concentrations along a Lagrangian trajectory can be de-  
 309 composed as follows:

$$\underbrace{\frac{\partial[\text{DIC}]}{\partial t} + \mathbf{u} \cdot \nabla[\text{DIC}]}_{\text{total}} = \frac{\partial[\text{DIC}]}{\partial t}_{\text{mixing}} + \frac{D[\text{DIC}]}{Dt}_{\text{bio}} + \frac{\partial[\text{DIC}]}{\partial t}_{\text{air-sea}} + \frac{\partial[\text{DIC}]}{\partial t}_{\text{residual}}. \quad (1)$$

310 Here, the left-hand side is the Lagrangian or total derivative of DIC along the pathway,  
 311  $\frac{D[\text{DIC}]}{Dt}$ . [DIC] in this study is expressed as a molar concentration of DIC, with units  $\mu\text{mol L}^{-1}$ ,  
 312 so that seawater density changes do not affect DIC concentrations in a control volume.  
 313 The Lagrangian derivative evolves due to vertical mixing into and out of the water par-

314 cel, along-trajectory biogeochemical sources and sinks (indicated by a Lagrangian deriva-  
315 tive), air-sea exchange (only in the surface layer), and residual terms.

316 The vertical mixing fluxes are computed from the model output vertical diffusiv-  
317 ity coefficient  $k_z$  and vertical gradients in DIC:

$$\frac{\partial[\text{DIC}]}{\partial t}_{\text{mixing}} = \partial_z(k_z \partial_z[\text{DIC}]). \quad (2)$$

318 We compute these as daily Eulerian fields and sample them along Lagrangian pathways.  
319 Because the model includes a horizontal diffusive mixing parameterization only for tem-  
320 perature and salinity, but not for biogeochemical tracers, we do not include a horizon-  
321 tal mixing term.

322 Not all PISCES state variables are stored as output in FREEBIORYS2V4: only  
323 chlorophyll, nitrate, phosphate, silicate, DIC, total alkalinity, and dissolved oxygen are  
324 available. Therefore, we need to approximate the biogeochemical sources and sinks from  
325 the available variables. We follow Sarmiento and Gruber (2006) and compute the bio-  
326 geochemical term as

$$\frac{D[\text{DIC}]}{Dt}_{\text{bio}} = \underbrace{r_{C:P} \frac{D[\text{PO}_4^{3-}]}{Dt}_{\text{bio}}}_{\text{soft-tissue}} + \frac{1}{2} \underbrace{\left( \frac{D[\text{TA}]}{Dt}_{\text{bio}} + \frac{D[\text{NO}_3^-]}{Dt}_{\text{bio}} \right)}_{\text{carbonate}}. \quad (3)$$

327 Here, the first term on the right-hand side corresponds to soft-tissue production and rem-  
328 ineralization. These values are estimated from changes in phosphate concentrations, with  
329  $r_{C:P}$  being the stoichiometric ratio of carbon to phosphorus in PISCES. The second term  
330 estimates changes in DIC due to calcite formation and dissolution from changes in to-  
331 tal alkalinity, correcting for changes in total alkalinity due to changes in nitrate origi-  
332 nating from soft-tissue processes (Brewer et al., 1975). The right-hand side of Equation  
333 (3) again consists of Lagrangian derivatives. Note that vertical mixing can also increase  
334 or decrease concentrations of phosphate, alkalinity, and nitrate along a Lagrangian tra-  
335 jectory. Rather than a biogeochemical effect, this is a physical effect on the DIC con-  
336 centrations, as already captured in the mixing term in Equation (1). The Lagrangian  
337 derivatives of the tracers in Equation (3) are therefore calculated by subtracting their  
338 precomputed diffusive mixing fluxes from the total along-trajectory change in tracer con-  
339 centrations, such that biogeochemical effects are isolated. For example:

$$\frac{D[\text{PO}_4^{3-}]}{Dt}_{\text{bio}} = \frac{D[\text{PO}_4^{3-}]}{Dt} - \partial_z(k_z \partial_z[\text{PO}_4^{3-}]), \quad (4)$$

340 with similar equations for total alkalinity and nitrate.

341 Explicit air-sea exchange in the ocean model occurs only in the uppermost layer  
342 (1 m). Changing DIC concentrations in this uppermost layer will influence the concen-  
343 trations below by vertical diffusive mixing, as in Equation (2). In our Lagrangian sim-  
344 ulations, parcels generally do not reach the uppermost layer: no parcels do so when sim-  
345 ulated forward in time, and an annual average of 0.027% does so backward in time. This  
346 means that parcels do not experience explicit air-sea exchange. Instead, air-sea exchange  
347 only indirectly affects parcel DIC concentrations through strong diffusive mixing in the  
348 mixing layer. The air-sea exchange term from Equation (1) in our analysis thus becomes  
349 part of the vertical mixing term and is not treated separately. We also cannot differen-  
350 tiate between natural DIC and anthropogenic carbon ( $C_{\text{ant}}$ ; Gruber et al., 1996) since  
351 it is not included as a separate tracer in FREEBIORYS2V4.

352 The residual term captures changes in DIC concentrations that cannot be accounted  
353 for by the mixing and biogeochemical terms in Equation (1). We compute it by subtract-  
354 ing the biogeochemical and vertical mixing terms in Equation (1) from the total DIC deriva-

355 tive along the trajectory. The residual contains the discrepancies between the biogeo-  
 356 chemical DIC term computed from Equation (3) and the actual biogeochemical contri-  
 357 bution as it occurs in PISCES. For the very few parcels that reach the upper model level,  
 358 missing air-sea exchange will be captured by the residual. It also accounts for unconstrained  
 359 numerical mixing of DIC and other biogeochemical state variables. Atmospheric and river-  
 360 ine deposition of phosphorus and nitrogen are neglected when computing their biogeo-  
 361 chemical changes, thus also leaving an imprint on the residual. We cannot isolate the  
 362 effects of local freshening or evaporation along Lagrangian parcel trajectories, because  
 363 these terms cannot be constrained: usually, these can be estimated from salinity, but salin-  
 364 ity is explicitly horizontally mixed, unlike biogeochemical tracers. Thus, we do not nor-  
 365 malize DIC by local salinity in our analysis because horizontal mixing of salinity would  
 366 cause a drift in the budget over time. In addition, we are explicitly interested in the ef-  
 367 fect of vertical mixing on DIC concentrations. Evaporation- and precipitation-related  
 368 freshening directly impact nutrient concentrations only in the model surface layer. Be-  
 369 low the first meter, the effect of mixing of fresher and more saline waters on DIC con-  
 370 centrations is part of the mixing term (Equation 2).

371 With the implicit treatment of air-sea exchange in the vertical mixing flux, and with  
 372 the division of biogeochemical contributions into a soft-tissue term and a carbonate term,  
 373 the total DIC derivative is then decomposed as:

$$\frac{D[\text{DIC}]}{Dt}_{\text{total}} = \frac{\partial[\text{DIC}]}{\partial t}_{\text{mixing}} + \frac{D[\text{DIC}]}{Dt}_{\text{soft-tissue}} + \frac{D[\text{DIC}]}{Dt}_{\text{carbonate}} + \frac{\partial[\text{DIC}]}{\partial t}_{\text{residual}}. \quad (5)$$

374 To obtain an illustrative comparison of the contribution of each term to  $\frac{D[\text{DIC}]}{Dt}$ , we com-  
 375 pute the sum of the magnitudes of each component in the right-hand side Equation (5)  
 376 for each trajectory. Figure 3a shows the percentage by which each component contributes  
 377 to the sum of their magnitudes, computed from forward-in-time 1-year trajectories from  
 378 all years (30-day segments of disentangled time series in the year 2000 are found in SI  
 379 Fig. S35). Note that the net biogeochemical contribution may be lower than the sum  
 380 of its constituents, as these may have opposite signs. We aim to discern the significance  
 381 of each term in determining the  $\Delta\text{DIC}$  across entire trajectories. To achieve this, we ex-  
 382 clude time steps that cumulatively account for less than 5% of the sum of magnitudes,  
 383 thereby focusing on the time steps for which the total rate of change predominantly in-  
 384 fluences  $\Delta\text{DIC}$ . This method effectively screens out instances with minimal  $\frac{D[\text{DIC}]}{Dt}$  val-  
 385 ues, since these are susceptible to disproportionate impacts from numerical inaccuracies,  
 386 thus distorting the residual's impact. The residual accounts for about 19% of the sum  
 387 of magnitudes of each term, which per timestep is higher than the contribution of the  
 388 mixing and carbonate terms. However, our main analysis will show that the residual will  
 389 fluctuate in sign between timesteps and trajectories, such that its overall influence is lim-  
 390 ited. Figure 3a shows that biogeochemical terms are the dominant contributor to the to-  
 391 tal rate of change at each time step, with soft-tissue processes in turn being the main  
 392 constituent. As expected, mixing fluxes become increasingly important in the mixing layer,  
 393 where the contribution is twice as high as in the mixed layer and 13 times higher than  
 394 below the mixing layer. Carbonate terms are roughly six times smaller than soft-tissue  
 395 terms.

396 Because the residual term is composed of multiple unconstrained constituents (see  
 397 above), we computed correlations between the residual term and other terms. This can  
 398 shed light on whether the residual is systematically linked to one of the other processes.  
 399 Figure 3b shows that the residual is uncorrelated with the other constituents, meaning  
 400 none of these are systematically over- or underestimated. There is a weak correlation be-  
 401 tween the total DIC rate of change and the residual, which, as discussed earlier, could  
 402 be related to some unconstrained process that is missing in the budget. We note that  
 403 the soft-tissue contribution has a very high correlation with the total biogeochemical term,

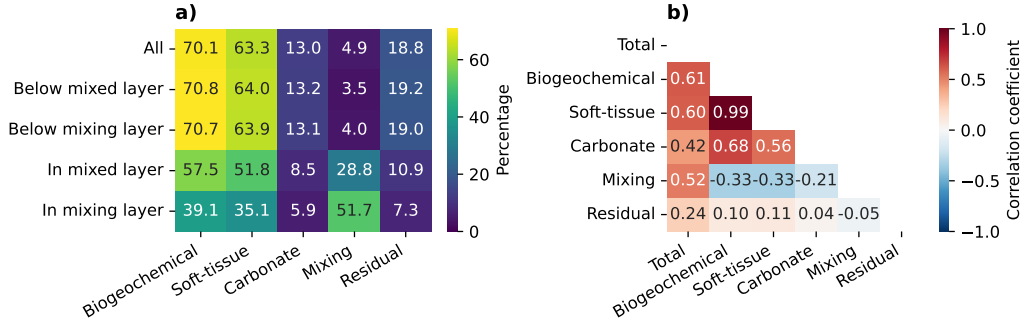


**Figure 3.** a) Percentage at which each term in Equation (5) contributes to the sum of their magnitudes, averaged over each time step. Percentages are computed using forward trajectories in all years, selecting only the time steps for which the total rate of change is responsible for at least 95% of the sum of all total magnitudes. We also examine the total biogeochemical rate of change, composed of soft-tissue and carbonate terms, which may have opposite signs. b) Correlations between each of the terms, including the total derivative  $\frac{D[DIC]}{Dt}$ .

404 meaning that it almost always dominates this term. The mixing term more often than  
 405 not is of the opposite sign as the biogeochemical terms, indicating net counteraction.

406 For each water parcel trajectory, we use the disentangled rates of change to recon-  
 407 struct time series of DIC anomalies with respect to the initial concentration for soft-tissue  
 408 processes, carbonate processes, vertical mixing, and residual processes.

409 **2.6 Identifying Enrichment and Depletion Regimes and Timescales**

410 One of our aims is to investigate the timescales and strengths at which DIC con-  
 411 centrations are depleted or enriched along NASTMW pathways. We examine both the  
 412 cumulative  $\Delta DIC$  along the pathway and intermittent DIC enrichment and depletion *regimes*  
 413 affecting DIC concentrations.

414 We have opted for a straightforward approach to define DIC enrichment and de-  
 415 pletion regimes. Specifically, these regimes are defined by the intervals in the time se-  
 416 ries between local minima, which indicate the start of enrichment, and local maxima,  
 417 which indicate the start of depletion. Thus, the duration of regimes corresponds to the  
 418 time intervals between these local minima and maxima, whereas the regime’s magnitude  
 419 is the change in DIC concentration during these intervals. In our analyses, we do not trun-  
 420 cate regimes that have their start date before the pathway’s end date: we analyze tra-  
 421 jectories from 1 September till 1 September in the subsequent year (or two years, in case  
 422 of export), but if a regime starts before this end date, we still include its entire timescale  
 423 in our analysis.

424 To reduce the impact of minor fluctuations occurring over short periods (a few days  
 425 or less), we apply a centered moving average to the time series after its disentanglement  
 426 into constituent terms. Although this approach smooths the series, it does not completely  
 427 eliminate short-time variability. Instead, it emphasizes significant changes in DIC con-  
 428 centration, minimizing the influence of brief, minor fluctuations at time scales shorter  
 429 than the window size. Therefore, the window size partially sets the scale for which regimes  
 430 are deemed significant.

431 The primary advantage of this methodology lies in its simplicity, offering a clear  
 432 lens to assess the main dynamics of DIC variations over time. Given our model’s nom-

433 inal resolution of  $1/4^\circ$ , it does not resolve the submesoscale, which is associated with nu-  
434 trient transport and biogeochemical structuring at timescales of the order of days (Lévy  
435 et al., 2012). Instead, we will apply a window length of 10 days, which is still much shorter  
436 than the lifetimes of mesoscale eddies (months) by which nutrients are supplied (McGillicuddy  
437 et al., 1998), and instead is of the same order as typical remineralization timescales (Siegel  
438 et al., 1999). This allows us to resolve processes on timescales of the order of a week and  
439 higher. Additionally, SI Text S5 repeats our analysis without any smoothing, and with  
440 smoothing using window sizes of 6 and 20 days. Especially when no smoothing is applied,  
441 the bulk of the regime lengths are shorter than 10 days, while their magnitudes are also  
442 much smaller. This illustrates the need for smoothing to shed light on processes at longer  
443 timescales.

### 3 Results: DIC Enrichment and Depletion along NASTMW Pathways

Table 1 summarizes the mean  $\Delta$ DIC for each pathway, averaged over all years, and the mean fraction of parcels that follow each pathway. This shows that parcels undergo the largest change in DIC while subducting from the mixed layer over the course of a year, while at the same time, only 1.2% of parcels make up this pathway. Forward in time, the most prominent pathway is persistence, accounting for 25.9% of the trajectories, followed by export and ventilation. Since the  $\Delta$ DIC does not follow a normal distribution, we do not include statistics of variance in Table 1. Instead, these distributions are provided and discussed directly in the following subsections.

Pathway	$\Delta$ DIC in model [ $\mu\text{mol L}^{-1}$ ]	Average % of parcels in one simulation
1. Subduction	100.8	1.2 % <sup>†</sup>
2. Persistence	6.0	25.9 %
3. Ventilation	0.7	9.1 %
4. Export	9.9 <sup>‡</sup>	15.3 %

**Table 1.** Yearly mean  $\Delta$ DIC for each pathway in the hindcast model, including mean occurrences. <sup>†</sup> This percentage increases if we consider long timescales for subduction, with the associated  $\Delta$ DIC still having a similar magnitude ( $110 \mu\text{mol L}^{-1}$  if subduction occurs over 2 or 3 years; see Section 3.1). <sup>‡</sup> DIC changes mostly occur before the parcel is exported (Section 3.4).

The above pathways are non-exhaustive and non-exclusive (Section 2.4), but the trajectories that are not accounted for can follow a myriad of paths, hindering their analysis. For comparison, SI Text S6 gives a brief overview of the total  $\Delta$ DIC and timescale distributions for all trajectories emanating from NASTMW in the forward and backward simulations. In summary, for all trajectories starting in the mode water,  $\Delta$ DIC =  $5.4 \mu\text{mol L}^{-1}$  over the following year, while for all trajectories that ended up in the mode water,  $\Delta$ DIC =  $4.3 \mu\text{mol L}^{-1}$  over the previous year.

Each pathway is discussed individually in the following subsections. We plot the distribution of total  $\Delta$ DIC and show the relative contribution of biogeochemical, mixing, and residual processes for different total  $\Delta$ DIC magnitudes. The integrated monthly strength of each process is also discussed. Lastly, we examine distributions of enrichment and depletion events spread across timescales and processes.

#### 3.1 The Subduction Pathway

As can be seen from Figure 4, subduction of parcels into NASTMW has a large impact on DIC concentrations in the water parcels: the mean increase is  $\sim 100 \mu\text{mol L}^{-1}$ , though with a large spread for different parcels (Fig. 4a). The dominant contribution comes from vertical mixing, which acts chiefly when the parcel is in the mixing layer. The mixing contribution grows from September until December, after which it decreases to near-zero around May, where it remains steady for the rest of the year (Fig. 4f). This increased mixing coincides with increased downwelling (not shown): upon initialization, parcels experience downwelling at a mean rate of 0.1 m per day in September, increasing steadily to a maximum of approximately 1 m per day in March, after which downwelling velocities reduce again to 0.1 m per day in May. The strength of the vertical mixing flux is then proportional to the downwelling rate and the vertical gradient at the depth of the parcel (SI Fig. 9). Most parcels exit the mixed layer in April when the mixing layer

478 shoals again and mixing decreases drastically. In the winter months, when the mixing  
 479 layer deepens and entrains nutrients, there is a small negative soft-tissue carbon contri-  
 480 bution from primary productivity (Fig. 4e). Although the spring bloom is visible as a  
 481 minimum in the mean yearly fifth percentile, subducting NASTMW parcels experience  
 482 a mean increase in DIC in April, as they move below the mixing layer again. Reminer-  
 483 alization continues over the course of the following months, as subducting NASTMW  
 484 is rich in semi-labile dissolved organic carbon that can be remineralized (Carlson et al.,  
 1994; Kr meur et al., 2009).

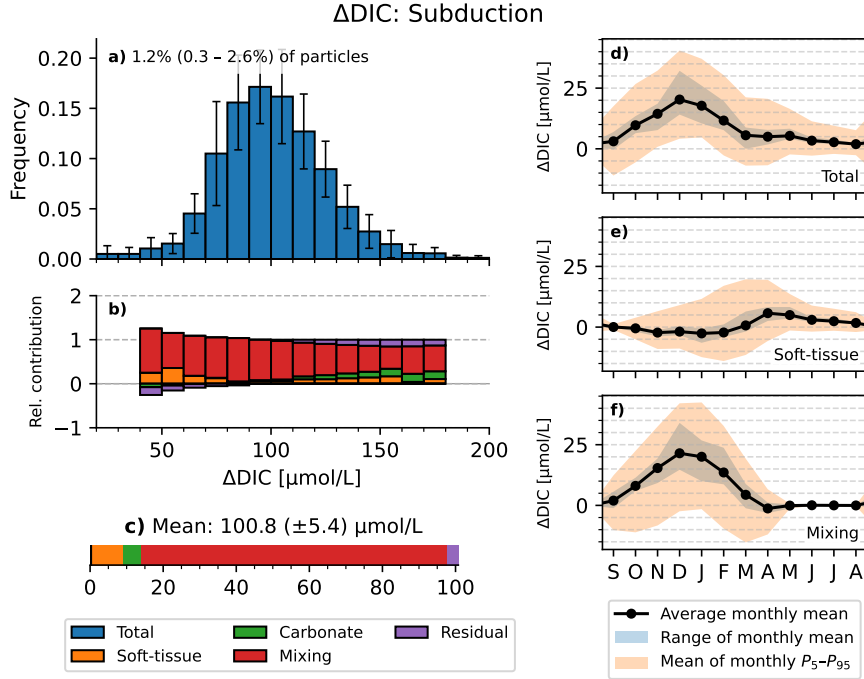


**Figure 4.** Transformation of DIC concentrations along pathways of parcels that subduct and reach NASTMW. (a) Distribution of total  $\Delta\text{DIC}$  per trajectory for all initialization years 1995-2015. Error bars indicate standard deviation for each bin per year. The average number of trajectories of this pathway is indicated as a percentage of all simulated trajectories per year, with min-max ranges indicated in brackets. (b) Relative contribution of each process to the average  $\Delta\text{DIC}$ , for different  $\Delta\text{DIC}$  strengths. The sum of contributions is always 1, meaning that contributions greater than 1 are balanced by contributions of the opposite sign. The relative contribution is computed only for bins with their edges between the 1st and 99th percentile of  $\Delta\text{DIC}$ . (c) Mean of yearly average  $\Delta\text{DIC}$  of trajectories, with the standard deviation across years in brackets. (d-f) Mean monthly integrated DIC changes, averaged across years, as well as its interannual range and the average of monthly 5th and 95th percentiles across years, for the total DIC rate of change (d), soft-tissue processes (e), and mixing fluxes (f). Carbonate and residual terms are much smaller and are shown in SI Fig. S40 a & b.

485

486 We investigate the timescales and magnitudes associated with the enrichment and  
 487 depletion regimes in Figure 5. Vertical mixing is the dominant contributor across regime  
 488 timescales (Fig 5a). Only at timescales of 10 days or less, the net  $\Delta\text{DIC}$  is slightly neg-  
 489 ative. DIC depletion regimes at timescales of 30 days or less primarily occur around March  
 490 (not shown), during peak primary production. The regime distribution has a long pos-

491 itive tail with around 43% of DIC changes associated with timescales of more than 100  
 492 days, mostly associated with vertical mixing. When regime detection is applied specif-  
 493 ically to the mixing-related DIC anomaly time series, almost 90% of the  $\Delta$ DIC is asso-  
 494 ciated with regimes with these long timescales (SI Fig. S41). This shows that vertical  
 495 mixing steadily increases DIC concentrations as parcels subduct into NASTMW, adjust-  
 496 ing to the ambient vertical DIC distribution, with larger DIC concentrations at depth  
 that can supply the parcel with DIC from below (SI Fig. S9).

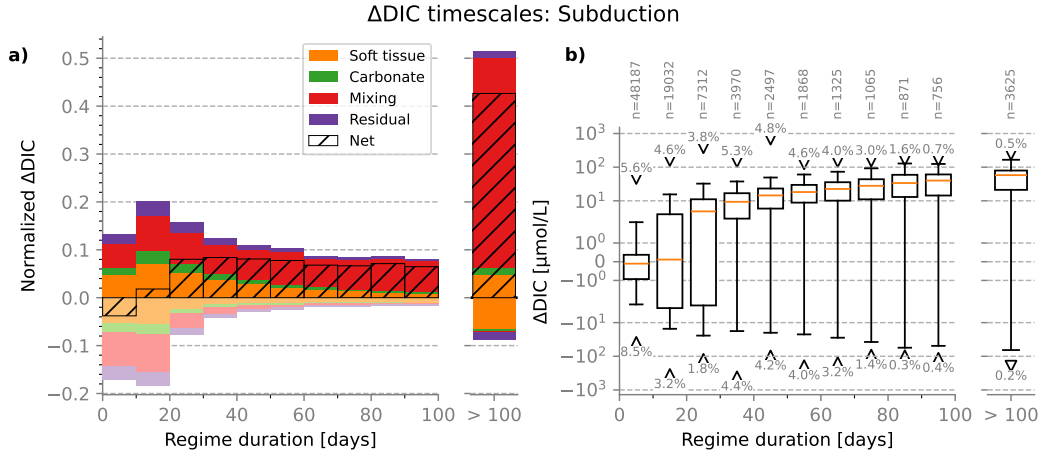


**Figure 5.**  $\Delta$ DIC contribution of each timescale for parcels that subduct and reach NASTMW. (a) Relative  $\Delta$ DIC of regimes of each timescale. This quantity is computed by summing the magnitudes of each positive and negative regime for all trajectories across years and then normalizing by the sum of  $\Delta$ DIC of each whole trajectory. ‘Net’ shows the positive minus negative normalized  $\Delta$ DIC. Because the distribution has a long tail, regimes longer than 100 days are grouped together. (b) Boxplot of  $\Delta$ DIC magnitudes for each regime for each timescale. Maxima and minima of outliers are indicated by triangles. The number of positive and negative outliers is indicated as a percentage of the total number of regimes, which is indicated above. The boxplot follows the classical definition: whiskers are defined as  $Q_1 - 1.5 * IQR$  and  $Q_3 + 1.5 * IQR$ . Outliers are defined as regimes with magnitudes that fall outside the whisker ranges.

497

498 While the soft-tissue, carbonate, and residual terms have a relatively minor con-  
 499 tribution to the total  $\Delta$ DIC (Fig. 4c), their contributions are of similar order to the to-  
 500 tal  $\Delta$ DIC of the other pathways (shown later). The residual and carbonate processes here  
 501 exhibit the largest contribution (and spread) when parcels are in the mixing layer (SI  
 502 Fig. 36a & b).

503 A yearly average of 1.2% of backtracked parcels originate from the mixed layer on  
 504 the previous September 1st. We also investigated subduction occurring over two and three  
 505 years. As this allows parcels to subduct over longer timescales, more parcels meet this  
 506 criterion (3.7% and 5.8% respectively). This is discussed in SI Text S3. In summary, these  
 507 parcels on average experience a total  $\Delta$ DIC of similar order ( $110 \mu\text{mol L}^{-1}$  in both cases;  
 508 see Figs. S13 and S15). While vertical mixing is still the dominant contributor in both  
 509 cases, soft-tissue processes progressively make up a higher share of the mean total  $\Delta$ DIC:  
 510 for subduction over 1 year, these make up 9% of  $\Delta$ DIC, with this contribution increas-  
 511 ing to 20% and 30% when subduction occurs over 2 and 3 years, respectively. These soft-  
 512 tissue contributions are an important factor in shaping the vertical distribution of DIC  
 513 (Sarmiento & Gruber, 2006). The longer a parcel takes to subduct, the more time soft-

514 tissue remineralization processes have to directly increase the parcel's DIC, whereas dur-  
515 ing quick subduction the parcel will instead adapt its DIC to ambient conditions through  
516 mixing.

517

### 3.2 The Persistence Pathway

518

519

520

521

522

523

524

525

526

527

528

529

Figure 6, shows the total transformation of DIC concentrations within parcels that persist in NASTMW throughout a full year. On average, this accounts for 25.9% of all parcels and thus agrees with the model study of Gary et al. (2014), where 74% of NASTMW parcels exit the mode water within a year. Note, however, the large interannual range of parcels that comprise this pathway (Fig. 6a). The minimum of 2.9% is associated with parcels initialized in September 2013, where the following year 2014 marked a strong decline in the modeled NASTMW volume toward its minimum in the summer of 2014 (SI Figure S14). Interannual variability in NASTMW formation and volume is commonly observed (Billheimer & Talley, 2013; Stevens et al., 2020). Generally, we find that the percentage of parcels that persist in NASTMW is correlated with the volume in the next year, with a Pearson-R of 0.88 ( $p < 0.001$ ); fewer parcels can persist in NASTMW if its volume shrinks from one year to the next.

530

531

532

533

534

535

536

537

538

539

540

541

Figure 6b shows that positive contributions are dominated by soft-tissue remineralization, which has a slightly positive monthly mean contribution year-round (Fig. 6e). Vertical mixing leaves a distinctly negative imprint on the  $\Delta$ DIC of persisting NASTMW parcels, meaning that it depletes parcels of carbon. This occurs specifically in winter (Fig. 6f), when the mixing layer deepens, and causes 19% of parcels to have a negative  $\Delta$ DIC. Because winter mixing is a primary driver of NASTMW formation, some parcels that persist in NASTMW may in fact reside in well-mixed newly formed NASTMW. Vertical mixing can then act to deplete DIC from these parcels as it is supplied to the euphotic zone. We find that the vertical displacement of a parcel is a predictor for the total  $\Delta$ DIC (Pearson-R of 0.51,  $p < 0.001$ ): parcels that move deeper, are more likely to have increased DIC concentrations. This can be due to a smaller likelihood of being temporarily entrained in NASTMW regions that are in contact with the mixing layer.

542

543

544

545

While the net residual term is smaller than the soft-tissue and mixing terms, the carbonate term is smaller than these residual terms, so we neglect it in our discussion for this pathway. Both the carbonate and residual terms show no clear yearly cycle (SI Fig. S40c & d).

546

547

548

549

550

551

From Figure 7 we see that net depletion is associated with timescales of 30 days and less. For timescales between 10 and 30 days, about half of the depletion is attributed to vertical mixing. This is largely associated with the winter convection. The contribution of photosynthesis, a soft-tissue process, has its mode at the 10-20 day timescale. The associated timescales of the order of weeks correspond to observations of the spring bloom in the Sargasso Sea (Nelson et al., 2004).

552

553

554

555

556

557

558

559

560

561

562

Soft-tissue DIC enrichment, associated with remineralization, has its mode at the 20-30 day timescale, but its tail extends over longer timescales than DIC depletion, with a contribution of almost half the total net  $\Delta$ DIC at timescales longer than 100 days (see the timescales associated with the soft-tissue DIC anomaly, SI Fig. S42). Figure 7b shows that for timescales less than 20 days, the mode  $\Delta$ DIC of each individual regime is close to zero at timescales less than 20 days and gradually increases to  $6.2 \mu\text{mol L}^{-1}$  for timescales longer than 100 days. The net negative  $\Delta$ DIC at timescales less than 30 days then suggests that strongly negative ‘outliers’ are responsible for a net decrease at this timescale. For regimes with durations of around a month, we find that these outliers are largely concentrated around March, coinciding with the spring bloom. The spring bloom can thus be linked to strong anomalous DIC depletion for parcels residing in NASTMW.

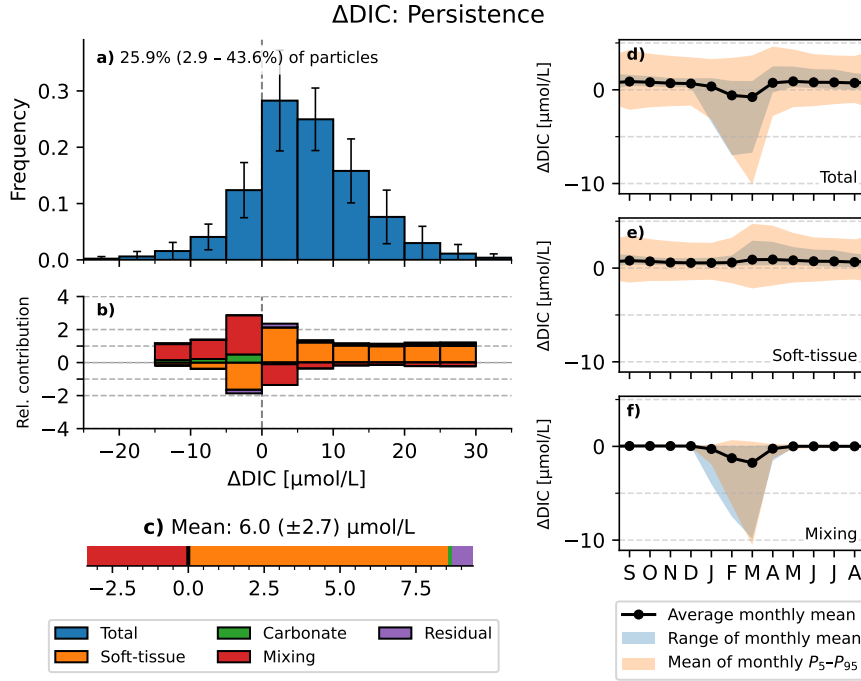


**Figure 6.** Similar to Figure 4, but for parcels that persistently remain in NASTMW. (a) Distribution of total  $\Delta\text{DIC}$  per trajectory, averaged over initialization years 1995-2015. (b) Relative contribution of each process to the average  $\Delta\text{DIC}$ , for different  $\Delta\text{DIC}$  strengths. Note that when the average  $\Delta\text{DIC}$  is negative, positive contributions to  $\Delta\text{DIC}$  (e.g. soft-tissue remineralization) have a negative relative contribution. (c) Mean of yearly average  $\Delta\text{DIC}$  of all trajectories. (d-f) Mean monthly integrated DIC changes averaged across years for the total DIC rate of change (d), soft-tissue processes (e), and mixing fluxes (f). Carbonate and residual terms are much smaller and are shown in SI Fig. S40c & d.

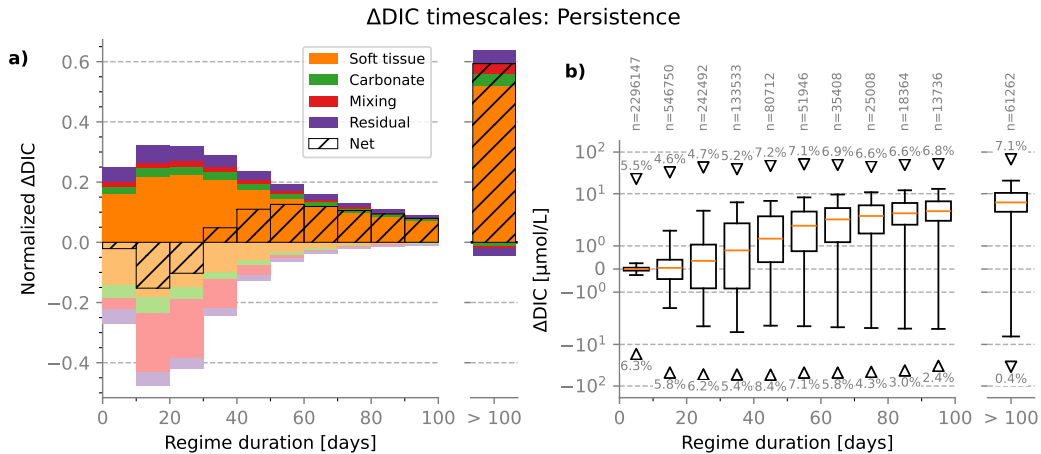


**Figure 7.**  $\Delta\text{DIC}$  contribution of each timescale for persisting NASTMW parcels. (a) Relative  $\Delta\text{DIC}$  of regimes of each timescale. (b) Boxplot of magnitudes of each regime for each timescale.

563

### 3.3 The Ventilation Pathway

564

565

566

567

568

569

570

571

572

On average, parcels that ventilate by temporarily reaching the mixing layer undergo a negligible net  $\Delta$ DIC (Figure 8). The mean total  $\Delta$ DIC of  $0.7 \mu\text{mol L}^{-1}$  is smaller than the interannual standard deviation. On aggregate, this means that the ventilation of existing NASTMW parcels does not influence the NASTMW carbon content appreciably. However, the  $\Delta$ DIC distribution for individual trajectories in Fig. 8a shows a wide spread between positive and negative values. We find that the total  $\Delta$ DIC along this pathway is correlated with the net downward displacement in the water column with a Pearson-R of 0.60 ( $p < 0.001$ ). Thus, over one yearly ventilation cycle, the net deepening of a parcel is a predictor of its increase in DIC.

573

574

575

576

577

578

579

580

581

582

583

584

585

586

587

588

589

590

Figure 8b and c show a strong counteraction of DIC enrichment from soft-tissue remineralization and a negative contribution for vertical mixing. Figure 8f shows how winter mixing is responsible for the decrease in DIC, as the parcel exchanges its DIC with the mixing layer, supplying nutrients for primary production in the euphotic zone, as well as equilibrating with the upper layer in which air-sea fluxes allow for atmospheric gas exchange. Although the mean monthly soft-tissue term never becomes negative, the mean 5th percentile has a minimum around February and March. This coincides with a modeled maximum in net primary production of phytoplankton, associated with the spring bloom. Only some parcels experience this negative soft-tissue contribution directly, as not all parcels can reach the euphotic zone where primary production occurs. Instead, many parcels are linked to the spring bloom indirectly, supplying it with nutrients from the deeper parts of the mixing layer. Following this, the mean soft-tissue term has a slight positive maximum in April (Fig. 8e), as the mixing layer shoals and moves above the parcel, allowing organic carbon to remineralize. The net DIC term remains positive over the following months (Fig. 8d,e). Carbonate processes have a small positive yearly contribution, also peaking in April, after most parcels have left the mixing layer (Fig. S22e). Note that residual processes have no net effect on the  $\Delta$ DIC for this pathway since they effectively cancel each other out (Fig. 9a and SI Fig. S40f).

591

592

593

594

595

596

597

598

599

600

601

602

603

604

605

Mixing is the main contributor to the net depletion of DIC at timescales shorter than 40 days (Fig. 9a). The distribution of DIC enrichment and depletion regimes for ventilating parcels is somewhat similar to that of persisting NASTMW parcels, albeit with a larger contribution from mixing at the short timescales. Fig. 9b shows that the interquartile range and whiskers are symmetric with the median around 0 for timescales less than 20 days, with the median becoming positive at longer timescales. However, since the normalized  $\Delta$ DIC for regimes at timescales less than 30 days is negative, this net negative contribution must be due to strongly depleting outlier regimes, associated with vigorous mixing. In SI Fig. S43, we identify regime timescales and magnitudes based on the DIC anomaly due to mixing processes. Interestingly, we find that about 40% of the net contribution of mixing processes has regime timescales of more than 100 days. When assuming a regime-based view of the total DIC anomaly, the relatively steady DIC depletion due to mixing during wintertime ventilation can be temporarily counteracted by local soft-tissue remineralization, such that mixing is not able to cause the total DIC anomaly to persistently decrease for such long timescales.

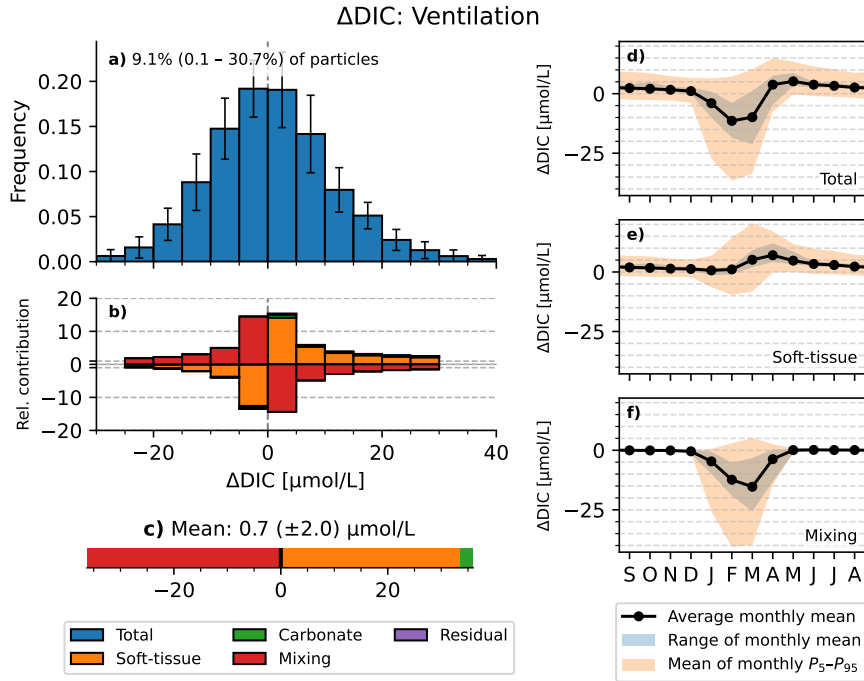


**Figure 8.** Similar to Figure 4, but for ventilating NASTMW parcels. (a) Distribution of total  $\Delta\text{DIC}$  per trajectory, averaged over initialization years 1995-2015. (b) Relative contribution of each process to the average  $\Delta\text{DIC}$ , for different  $\Delta\text{DIC}$  strengths. (c) Mean of yearly average  $\Delta\text{DIC}$  of all trajectories. (d-f) Mean monthly integrated DIC changes averaged across years for the total DIC rate of change (d), soft-tissue processes (e), and mixing fluxes (f). Carbonate and residual terms are much smaller and are shown in SI Fig. S40e & f.

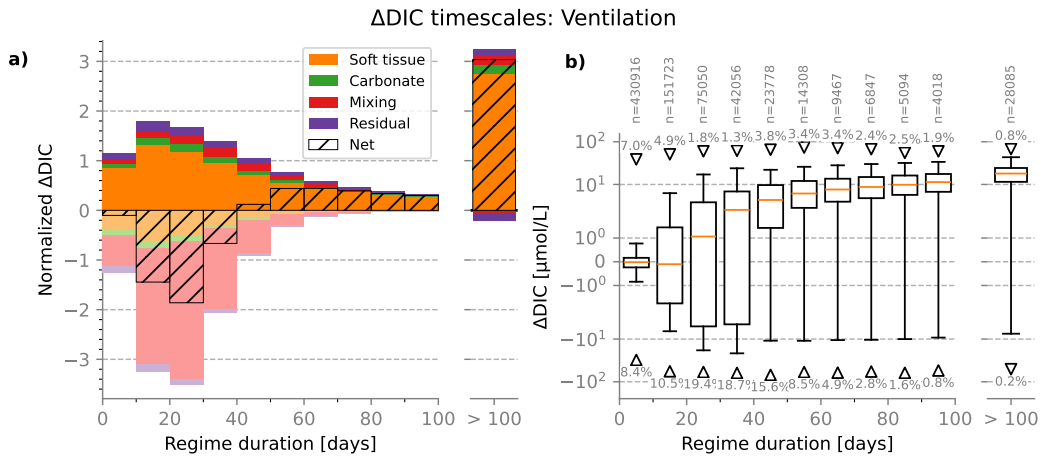


**Figure 9.**  $\Delta\text{DIC}$  contribution of each timescale for ventilating NASTMW parcels. (a) Relative  $\Delta\text{DIC}$  of regimes of each timescale. (b) Boxplot of magnitudes of each regime for each timescale.

606

### 3.4 The Export Pathway

607

608

609

610

611

612

613

614

615

616

617

618

619

620

621

622

623

624

NASTMW parcels that get exported to denser surroundings mostly undergo a net positive  $\Delta\text{DIC}$  (Fig. 10), with a yearly mean of  $9.9\ \mu\text{mol L}^{-1}$ . We recall that here, parcels are integrated for a total of two years, during which their potential density remains, for at least the entire second year, higher than their potential density upon exiting NASTMW (Section 2.4).

The distribution of  $\Delta\text{DIC}$  is asymmetric, with a longer tail in the positive direction (Fig. 10a). Soft-tissue processes make up the bulk of the  $\Delta\text{DIC}$  for trajectories in the positive tail (Fig. 10b). Note that for small and negative  $\Delta\text{DIC}$ , the residual becomes more prominent, indicating that the DIC budget becomes less well constrained by our disentanglement method (section 2.5). Mixing fluxes again are concentrated in the winter months of the first year. Due to the way we select exported parcels, some may be temporarily entrained into the mixing layer in the first year of integration. However, outside of the first winter months, the mean DIC changes are solely governed by soft-tissue processes. Note that after the first year, these are effectively zero, albeit with the 5th and 95th percentile ranging between values of around  $\pm 2\ \mu\text{mol L}^{-1}$  (Fig. 10e), while the residual has a range of  $\pm 1\ \mu\text{mol L}^{-1}$  (SI Fig. S40 g & h). Since these ranges are of the same order, while the mean is close to zero, we conclude that after the NASTMW parcels remain exported, they undergo no clear net DIC depletion or enrichment in the second year; the change in  $\Delta\text{DIC}$  occurs before.

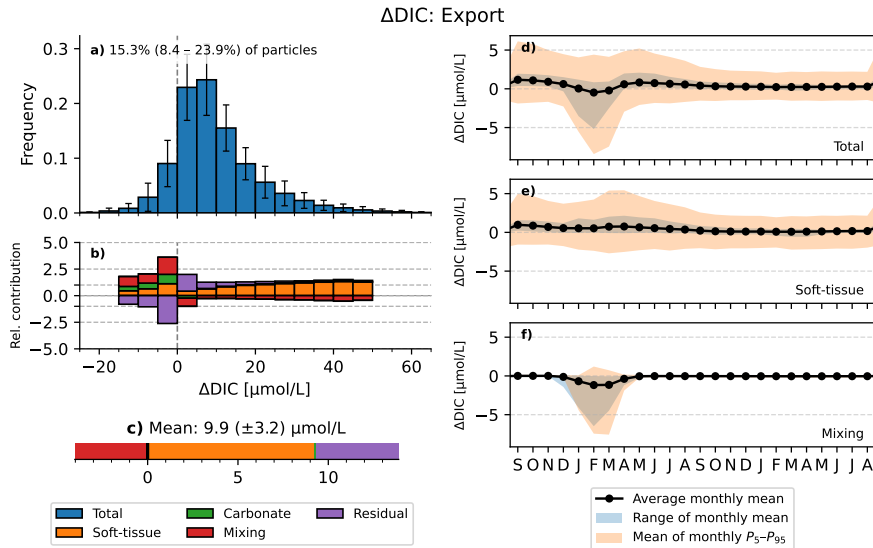


**Figure 10.** Similar to Figure 4, but for exported NASTMW parcels. (a) Distribution of total  $\Delta\text{DIC}$  per trajectory, averaged over initialization years 1995-2015. (b) Relative contribution of each process to the average  $\Delta\text{DIC}$ , for different  $\Delta\text{DIC}$  strengths. (c) Mean of yearly average  $\Delta\text{DIC}$  of all trajectories. (d-f) Mean monthly integrated DIC changes averaged across years for the total DIC rate of change (d), soft-tissue processes (e), and mixing fluxes (f). Carbonate and residual terms are much smaller and are shown in SI Fig. S40g & h.

625

626

627

628

629

Looking at enrichment and depletion regimes and timescales (Figure 11), we see that at short timescales of less than a month, positive and negative  $\Delta\text{DIC}$  regimes nearly balance one another. The net  $\Delta\text{DIC}$  of regimes with longer timescales becomes positive, dominated by soft-tissue remineralization. Mixing mainly acts to deplete exporting NASTMW

630 parcels of their DIC at timescales of around a month and less, while, photosynthesis and  
 631 remineralization balance each other out at timescales up to two weeks. At short timescales,  
 632 the enrichment and depletion magnitudes show a symmetric distribution, also in terms  
 633 of outliers (Fig. 11b), meaning that at these timescales, there is a balanced counterac-  
 tion.

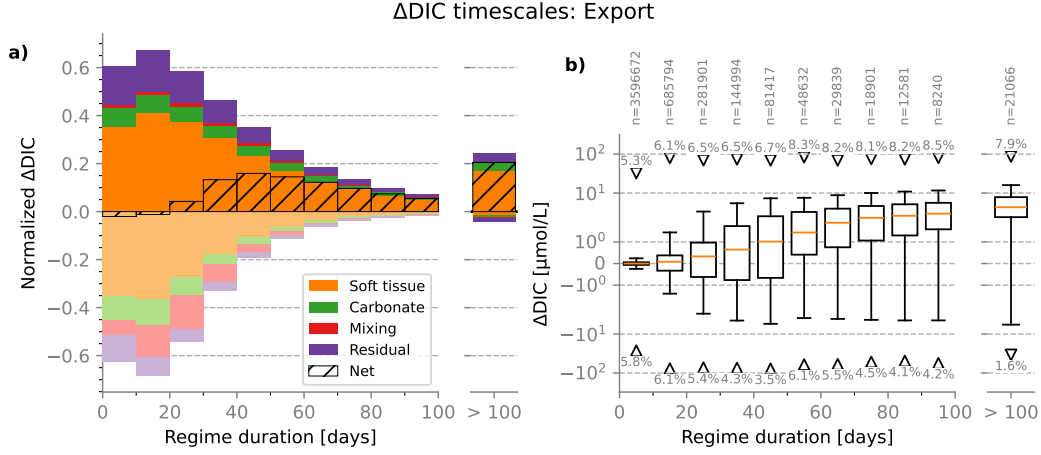


**Figure 11.**  $\Delta$ DIC contribution of each timescale for exported NASTMW parcels. (a) Relative  $\Delta$ DIC of regimes of each timescale. (b) Boxplot of magnitudes of each regime for each timescale.

634

635 Exported parcels remain in waters of higher density than the local NASTMW and  
 636 thus are situated at deeper depths. Compared to the persistence pathway (Fig. 7a), it  
 637 can therefore seem counter-intuitive that exported parcels experience more photosynthesis-  
 638 dominated regimes at timescales of a few weeks, even if these regimes are balanced by  
 639 remineralization (Fig. 11a). However, note that in the thinner flanks of NASTMW (Fig.  
 640 1b), parcels are less likely to persist if the NASTMW shrinks between years, such that  
 641 they get exported instead. On average, exported parcels in such regions may then be lo-  
 642 cated at shallower depths and experience more photosynthesis than parcels that in such  
 643 years persist in the central core of NASTMW, which extends to deeper depths.

644 While the number of parcels that we consider exported depends on the potential  
 645 density threshold,  $\Delta\sigma$ , these parcels qualitatively exhibit similar total  $\Delta$ DIC, regime mag-  
 646 nitudes, and timescales (SI Text S4).

## 647 4 Summary & Discussion

648 We adopted a Lagrangian frame of reference to study how dissolved inorganic carbon  
 649 concentrations are altered along different NASTMW pathways in an eddy-permitting  
 650 model that reproduces NASTMW for process study purposes. Of the four pathways con-  
 651 sidered, parcels experience the largest increase in DIC during subduction from the mixed  
 652 layer into NASTMW, with an order of magnitude of  $\sim 100 \mu\text{mol L}^{-1}$ . However, only 1.2%  
 653 of parcels subduct over the course of a year. This percentage increases to 3.7% and 5.8%  
 654 if we allow parcels to subduct over longer timescales of 2 and 3 years respectively, while  
 655 the increase in DIC remains similar at  $\sim 110 \mu\text{mol L}^{-1}$ . This implies that parcels gener-  
 656 ally take longer to move from the summer mixed layer to summer NASTMW, while  
 657 the total enrichment along the subduction path is roughly unaffected. The persistence  
 658 pathway makes up the largest fraction at 25.9%, which is in agreement with the find-  
 659 ings of Gary et al. (2014). The subduction, ventilation, and export pathways had not  
 660 been previously explored, and no previous study had yet investigated DIC concentra-  
 661 tions along mode water pathways. Kwon et al. (2015) explore the timescales between the  
 662 re-outcropping of NASTMW parcels, which somewhat resembles our ventilation path-  
 663 way. However, the main differences are that our study requires parcels to be directly in  
 664 the mixing layer instead of in an outcropping NASTMW column, and to reside in NASTMW  
 665 for two consecutive summers, which complicates direct comparisons. While our results  
 666 do not apply directly to other subtropical mode waters, they may provide initial qual-  
 667 itative hints of their DIC dynamics until further research is available.

668 Generally, a downward displacement of parcels is associated with net DIC enrich-  
 669 ment. This is in line with the positive downward gradient of observed DIC in the wa-  
 670 ter column, set by the remineralization of organic material. It then makes sense that the  
 671 net  $\Delta\text{DIC}$  for each of the four pathways is positive (Table 1), as the Subtropical Gyre  
 672 is associated with net sinking (Spall, 1992; Berglund et al., 2022). Subducting parcels  
 673 adjust to the vertical DIC gradient mostly through vertical mixing, but as longer sub-  
 674 duction times are allowed (SI Text S3), the contribution from mixing shrinks in favor  
 675 of direct remineralization within the parcel. Following the spring bloom, downward-moving  
 676 persisting NASTMW parcels and exported NASTMW parcels also experience enrichment  
 677 by remineralization directly. Ventilating parcels on the whole experience only a small  
 678 appreciable net DIC enrichment during one year, which is of a similar order of magni-  
 679 tude as the surface ocean model DIC trend (SI Fig. S12). This could indicate that ven-  
 680 tilating trajectories propagate DIC increases at the surface towards the NASTMW in-  
 681 terior. Unfortunately, model biases (SI Text S1) prevent us from directly comparing these  
 682 values to the observed Eulerian DIC trend at the BATS-site ( $1.5 \mu\text{mol kg}^{-1} \text{yr}^{-1}$ ; Bates,  
 683 2012). These ventilating parcels follow a cycle where they first supply DIC to the eu-  
 684 photic zone by vertical mixing in late winter, followed by remineralization of organic ma-  
 685 terial in the following months. The net sinking distance over a ventilation cycle is also  
 686 correlated with enrichment.

687 The timescales at which photosynthesis depletes parcels of DIC are of the order of  
 688 weeks, corresponding to observations of the spring bloom in the Sargasso Sea (Nelson  
 689 et al., 2004). This depletion is most prominent in persisting, ventilating, and exported  
 690 parcels. For these pathways, mixing also has a depleting component at similar timescales,  
 691 which is associated with an upward supply of DIC toward the surface. Mixing-associated  
 692 depletion peaks in March when the mixed layer depth is at its maximum, re-establishing  
 693 a link between NASTMW and the surface. This highlights the importance of NASTMW  
 694 as a reservoir that can store and resupply carbon to the ocean surface (Bates et al., 2002),  
 695 with relevance to ocean biology and ocean-atmosphere carbon exchange.

696 While the four pathways chosen for this study are non-exclusive and non-exhaustive,  
 697 they still provide a good picture of carbon cycling in NASTMW. This is corroborated  
 698 by the fact that when all trajectories are analyzed together (SI Text S6), they qualita-  
 699 tively resemble the persistence pathway and aspects of the ventilation and export path-

ways. Backward-in-time trajectories also resemble the persistence pathway, with the minor contribution from the subduction pathway superimposed on this. We think that the trajectories that are unaccounted for will often resemble the persistence pathway, because the aggregate of all trajectories qualitatively resembles the persistence pathway strongly, while it only accounts for about a quarter of all pathways. These ‘unaccounted trajectories’ can for instance be parcels leaving NASTMW only temporarily while not being ventilated or exported, or parcels that remain in the direct vicinity of NASTMW where carbon dynamics may be somewhat similar.

In the context of carbon sequestration in the Sargasso Sea, our findings show that once NASTMW parcels are exported, they experience only small changes in DIC concentrations, which average out each other for at least one year. Some of these parcels may re-outcrop during strong convection in the following winters (Kwon et al., 2015), which re-liberates their carbon (Bates et al., 2002). However, exported parcels may also further sink and travel out of the NASTMW ventilation region to the Subpolar Gyre over timescales  $> 10$  years (Gary et al., 2014). Berglund et al. (2022) show that transport between the Subtropical Gyre and Subpolar Gyre occurs in a downward-spiraling fashion over timescales of several decades. The long-term fate of carbon sequestered through the export of NASTMW parcels provides a direction for future research. We find that before such sequestration, DIC concentrations are set primarily due to mixing and to a lesser extent due to remineralization during a parcel’s journey from the mixed layer to NASTMW.

While this study did not consider NASTMW trends in the face of global (ocean) warming, we know that NASTMW is influenced by climate change. Observations show that ventilation and formation of NASTMW have decreased due to surface warming (Stevens et al., 2020). Under a strong warming scenario (SSP5-8.5), CMIP6 models report a shallowing of the winter mixed layer in the NASTMW formation region (Fox-Kemper et al., 2021), which would further decrease the ventilation of NASTMW parcels. This would decrease NASTMW formation and thus volume, decreasing the amount of heat and carbon that it can buffer, in the latter case allowing less carbon to potentially sequester through export of NASTMW parcels. We did not investigate these effects due to model biases (SI Text S1) and because of the limited temporal extent in the face of high interannual and decadal NASTMW variability (Kwon & Riser, 2004; Deremble & Dewar, 2013; Stevens et al., 2020). However, a future similar study using trajectories in a state-of-the-art Earth system model could shed light on this.

Of the four processes considered, soft-tissue processes and vertical mixing dominate DIC concentration changes. Carbonate processes play a much smaller role at these NASTMW depths and sub-annual timescales (Williams & Follows, 2011), sometimes with a smaller contribution than the residual. We note that here we estimated the carbonate term from alkalinity, while in reality it is also affected by nitrification. Still, we could not detect a systematic bias in the carbonate term (Section 2.5). Future studies that are interested in how carbonate processes influence DIC concentrations along Lagrangian trajectories would benefit from using a biogeochemical model where all the required state variables are stored for constraining the carbonate term. Exact calculation of the carbonate term can for example become important when studying Lagrangian carbon dynamics in the deep ocean where carbonate dissolution plays a more prominent role.

Time series of carbon along Lagrangian trajectories have previously been studied by Brady et al. (2021) in the context of upwelling in the Southern Ocean. Like Cetina-Heredia et al. (2018) did for nitrate, Brady et al. (2021) characterized DIC timescales by the Lagrangian decorrelation timescale. However, decorrelation metrics assume that Lagrangian biogeochemical time series are stationary, while in reality biogeochemical depletion and enrichment are highly dependent on the spatial (vertical and horizontal) and temporal location of the water parcel. For example, the DIC time series of a parcel can be influenced by the entrainment into an eddy that experiences high primary produc-

753 tivity, or by a quick decrease in vertical mixing after subduction through the thermo-  
754 cline. These processes are highly non-linear and non-stationary. This is why we intro-  
755 duced a straightforward approach where we define enrichment and depletion regimes be-  
756 tween local minima and maxima in smoothed Lagrangian DIC anomaly time series. Also,  
757 unlike methods based on spectral analysis, our method reveals regime timescales while  
758 staying agnostic about any periodicity, which may not be present.

759 Model data constraints prevent us from investigating the full mesoscale spectrum  
760 or submesoscale processes and variability, as higher resolution model data is not avail-  
761 able for large regions over the span of decades. To deal with model biases in our eddy-  
762 permitting set-up, we tuned our NASTMW definition criteria for a realistic model vol-  
763 ume and thickness, but, for example, our winter NASTMW core is too shallow (SI Text  
764 S1), possibly leading to an underestimation of the export pathway, which would be in-  
765 fluenced by larger vertical excursions of NASTMW depths between summer and winter.  
766 Gan et al. (2023) show that an eddy-rich model would more faithfully reproduce the  
767 observed NASTMW spread and volume. Moreover, the unresolved submesoscale dynam-  
768 ics have large implications for biogeochemistry, for example by creating fronts that pro-  
769 vide short-lived nutrient pulses of just a few days (Lévy et al., 2012; Mahadevan, 2016).  
770 The findings in this study instead are chiefly related to mesoscale ocean dynamics, with  
771 a resolution similar to physical ocean components of state-of-the-art earth system mod-  
772 els (Hewitt et al., 2020). While a similar study at a submesoscale resolution is at present  
773 computationally unfeasible, more process-based submesoscale Lagrangian studies, such  
774 as by Freilich et al. (2022) on phytoplankton growth rates, provide first steps in under-  
775 standing Lagrangian carbon dynamics at smaller scales.

776 Our findings highlight that individual parcels undergo DIC enrichment and deple-  
777 tion regimes over a range of timescales and magnitudes, due to a complex interplay of  
778 vertical mixing and biogeochemical processes. We find that on short timescales of the  
779 order of weeks, enrichment and depletion often oppose one another, which for the sub-  
780 duction, persistence, and export pathways leads to a relatively small net  $\Delta$ DIC at these  
781 timescales, which is why the largest net changes in DIC occur on longer timescales. Bulk  
782 Eulerian studies average out this underlying complexity of enrichment and depletion un-  
783 folding over different timescales. Our approach can thus complement Eulerian approaches  
784 when investigating the carbon cycle. This also applies beyond the context of NASTMW  
785 or mode waters entirely; our Lagrangian process and timescale decomposition can be ap-  
786 plied to any study aimed at better understanding carbon dynamics along water path-  
787 ways. For example, while Eulerian approaches are the dominant method to study ma-  
788 rine carbon dioxide removal through ocean alkalinity enhancement (Fennel et al., 2023),  
789 our methods may be used to study how alkalinity enhancement interventions influence  
790 DIC at different timescales along pathways of water downstream from intervention sites.  
791 Similarly, one could disentangle influences on  $p\text{CO}_2$ , phytoplankton, or even ecosystems  
792 if more model state variables are available.

## Open Research Section

The code to reproduce the results and figures from this paper is available at <https://github.com/OceanParcels/NASTMW.DIC>. Upon acceptance, it will be uploaded to YODA, Utrecht University's persistent data repository, where it will be assigned a DOI. The physical hindcast product FREEGLORYS2V4 was made available by Mercator Ocean International on request, and the biogeochemical hindcast product FREEBIORYS2V4 is available at <https://doi.org/10.48670/moi-00019> (E.U. Copernicus Marine Service Information (CMEMS), 2023). Bottle and DIC data used for model-data comparison in Supporting Information Text S1 are available through the CLIVAR and Carbon Hydrographic Data Office at <https://cchdo.ucsd.edu> (Pickard, 2022; Toole & MacDonald, 2022; Swift et al., 2022). WOA18 data is available at <https://www.ncei.noaa.gov/access/world-ocean-atlas-2018/> (Boyer et al., 2018). WOA23 data is available at <https://www.ncei.noaa.gov/access/world-ocean-atlas-2023/> (Reagan & NOAA National Centers for Environmental Information, 2023). The Parcels Lagrangian framework version 2.4.1 is available at [doi.org/10.5281/ZENODO.7680187](https://doi.org/10.5281/ZENODO.7680187) (Van Sebille et al., 2023).

## Acknowledgments

DR and EvS were supported through funding from the Netherlands Organization for Scientific Research (NWO), Earth and Life Sciences, through project OCENW.KLEIN.085. DCEB was supported by UKRI's (UK Research and Innovation) CHALKY project NE/Y004388/1. We thank Siren Rühls and Jamie Palter for useful discussions and feedback, and Coralie Perruche for help with the FREEBIORYS2V4 product. This study has been conducted using E.U. Copernicus Marine Service Information. Bottle and CTD data along A20 in 2003 and 2012 was supported by the NSF/NOAA funded U.S Global Ocean Carbon and Repeat Hydrography Program.

## References

- Atkins, J., Andrews, O., & Frenger, I. (2022). Quantifying the contribution of ocean mesoscale eddies to low oxygen extreme events. *Geophysical Research Letters*, *49*(15), e2022GL098672. doi: 10.1029/2022GL098672
- Aumont, O., Ethé, C., Tagliabue, A., Bopp, L., & Gehlen, M. (2015). PISCES-v2: An ocean biogeochemical model for carbon and ecosystem studies. *Geoscientific Model Development*, *8*(8), 2465–2513. doi: 10.5194/gmd-8-2465-2015
- Bates, N. R. (2012). Multi-decadal uptake of carbon dioxide into subtropical mode water of the North Atlantic Ocean. *Biogeosciences*, *9*(7), 2649–2659. doi: 10.5194/bg-9-2649-2012
- Bates, N. R., Best, M. H. P., Neely, K., Garley, R., Dickson, A. G., & Johnson, R. J. (2012). Detecting anthropogenic carbon dioxide uptake and ocean acidification in the North Atlantic Ocean. *Biogeosciences*, *9*(7), 2509–2522. doi: 10.5194/bg-9-2509-2012
- Bates, N. R., Pequignat, A. C., Johnson, R. J., & Gruber, N. (2002). A short-term sink for atmospheric CO<sub>2</sub> in subtropical mode water of the North Atlantic Ocean. *Nature*, *420*(6915), 489–493. doi: 10.1038/nature01253
- Berglund, S., Döös, K., Groeskamp, S., & McDougall, T. J. (2022). The downward spiralling nature of the North Atlantic Subtropical Gyre. *Nature Communications*, *13*(1), 2000. doi: 10.1038/s41467-022-29607-8
- Bernard, B., Madec, G., Penduff, T., Molines, J.-M., Treguier, A.-M., Le Sommer, J., ... De Cuevas, B. (2006). Impact of partial steps and momentum advection schemes in a global ocean circulation model at eddy-permitting resolution. *Ocean Dynamics*, *56*(5-6), 543–567. doi: 10.1007/s10236-006-0082-1
- Billheimer, S., & Talley, L. D. (2013). Near cessation of Eighteen Degree Water renewal in the western North Atlantic in the warm winter of 2011–2012. *Journal of Geophysical Research: Oceans*, *118*(12), 6838–6853. doi:

- 844 10.1002/2013JC009024
- 845 Billheimer, S., & Talley, L. D. (2016). Annual cycle and destruction of eighteen de-  
846 gree water. *Journal of Geophysical Research: Oceans*, *121*(9), 6604–6617. doi:  
847 10.1002/2016JC011799
- 848 Billheimer, S., Talley, L. D., & Martz, T. R. (2021). Oxygen seasonality, utiliza-  
849 tion rate, and impacts of vertical mixing in the Eighteen Degree Water Region  
850 of the Sargasso Sea as observed by profiling biogeochemical floats. *Global*  
851 *Biogeochemical Cycles*, *35*(3). doi: 10.1029/2020GB006824
- 852 Blanke, B., & Delecluse, P. (1993). Variability of the tropical atlantic ocean  
853 simulated by a general circulation model with two different mixed-layer  
854 physics. *Journal of Physical Oceanography*, *23*(7), 1363–1388. doi:  
855 10.1175/1520-0485(1993)023<1363:VOTTAO>2.0.CO;2
- 856 Boyer, T. P., García, H. E., Locarnini, R. A., Zweng, M. M., Mishonov, A. V.,  
857 Reagan, J. R., . . . Smolyar, I. V. (2018). [Dataset] *World Ocean Atlas*  
858 *2018, Mixed Layer Depth - statistical mean on 1/4° grid for 2005-2017*.  
859 NOAA National Centers for Environmental Information. Retrieved from  
860 <https://www.ncei.noaa.gov/archive/accession/NCEI-WOA18> (Accessed on  
861 1 March 2023)
- 862 Brady, R. X., Maltrud, M. E., Wolfram, P. J., Drake, H. F., & Lovenduski,  
863 N. S. (2021). The influence of ocean topography on the upwelling of car-  
864 bon in the Southern Ocean. *Geophysical Research Letters*, *48*(19). doi:  
865 10.1029/2021GL095088
- 866 Brainerd, K. E., & Gregg, M. C. (1995). Surface mixed and mixing layer depths.  
867 *Deep Sea Research Part I: Oceanographic Research Papers*, *42*(9), 1521–1543.  
868 doi: 10.1016/0967-0637(95)00068-H
- 869 Brewer, P. G., Wong, G. T., Bacon, M. P., & Spencer, D. W. (1975). An oceanic  
870 calcium problem? *Earth and Planetary Science Letters*, *26*(1), 81–87. doi: 10  
871 .1016/0012-821X(75)90179-X
- 872 Carlson, C. A., Ducklow, H. W., & Michaels, A. F. (1994). Annual flux of dissolved  
873 organic carbon from the euphotic zone in the northwestern Sargasso Sea. *Na-*  
874 *ture*, *371*(6496), 405–408. doi: 10.1038/371405a0
- 875 Cetina-Heredia, P., van Sebille, E., Matear, R. J., & Roughan, M. (2018). Nitrate  
876 sources, supply, and phytoplankton growth in the Great Australian Bight: An  
877 Eulerian-Lagrangian Modeling approach. *Journal of Geophysical Research:*  
878 *Oceans*, *123*(2), 759–772. doi: 10.1002/2017JC013542
- 879 Davis, X. J., Straneo, F., Kwon, Y.-O., Kelly, K. A., & Toole, J. M. (2013). Evolu-  
880 tion and formation of North Atlantic Eighteen Degree Water in the Sargasso  
881 Sea from moored data. *Deep Sea Research Part II: Topical Studies in Oceanog-*  
882 *raphy*, *91*, 11–24. doi: 10.1016/j.dsr2.2013.02.024
- 883 Dee, D. P., Uppala, S. M., Simmons, A. J., Berrisford, P., Poli, P., Kobayashi, S., . . .  
884 Vitart, F. (2011). The ERA-Interim reanalysis: configuration and performance  
885 of the data assimilation system. *Quarterly Journal of the Royal Meteorological*  
886 *Society*, *137*(656), 553–597. doi: <https://doi.org/10.1002/qj.828>
- 887 Delandmeter, P., & van Sebille, E. (2019). The Parcels v2.0 Lagrangian framework:  
888 New field interpolation schemes. *Geoscientific Model Development*, *12*(8),  
889 3571–3584. doi: 10.5194/gmd-12-3571-2019
- 890 Deremble, B., & Dewar, W. K. (2013). Volume and Potential Vorticity Budgets of  
891 Eighteen Degree Water. *Journal of Physical Oceanography*, *43*(11), 2309–2321.  
892 doi: 10.1175/JPO-D-13-052.1
- 893 E.U. Copernicus Marine Service Information (CMEMS). (2023). [Dataset] *FREE-*  
894 *BIORYS2V4 Global Ocean Biogeochemistry Hindcast*. Marine Data Store  
895 (MDS). (Accessed on 1 March 2023) doi: 10.48670/moi-00019
- 896 Fennel, K., Long, M. C., Algar, C., Carter, B., Keller, D., Laurent, A., . . .  
897 Whitt, D. B. (2023). Modelling considerations for research on ocean al-  
898 kalinity enhancement (OAE). *State of the Planet, 2-oae2023*, 9. doi:

- 899 10.5194/sp-2-oae2023-9-2023
- 900 Forget, G., Maze, G., Buckley, M., & Marshall, J. (2011). Estimated Seasonal  
901 Cycle of North Atlantic Eighteen Degree Water Volume. *Journal of Physical*  
902 *Oceanography*, *41*(2), 269–286. doi: 10.1175/2010JPO4257.1
- 903 Fox-Kemper, B., Hewitt, H., Xiao, C., Adalgeirsdóttir, G., Drijfhout, S., Edwards,  
904 T., ... Yu, Y. (2021). Ocean, cryosphere and sea level change [Book Section].  
905 In V. Masson-Delmotte et al. (Eds.), *Climate change 2021: The physical sci-*  
906 *ence basis. Contribution of working group I to the sixth assessment report of*  
907 *the intergovernmental panel on climate change* (pp. 1211–1362). Cambridge,  
908 United Kingdom and New York, NY, USA: Cambridge University Press. doi:  
909 10.1017/9781009157896.011
- 910 Fratantoni, D. M., Kwon, Y.-O., & Hodges, B. A. (2013). Direct observation of sub-  
911 tropical mode water circulation in the western North Atlantic Ocean. *Deep Sea*  
912 *Research Part II: Topical Studies in Oceanography*, *91*, 35–56. doi: 10.1016/j  
913 .dsr2.2013.02.027
- 914 Freilich, M. A., Flierl, G., & Mahadevan, A. (2022). Diversity of Growth Rates  
915 Maximizes Phytoplankton Productivity in an Eddying Ocean. *Geophysical Re-*  
916 *search Letters*, *49*(3). doi: 10.1029/2021GL096180
- 917 Friedlingstein, P., O’Sullivan, M., Jones, M. W., Andrew, R. M., Gregor, L., Hauck,  
918 J., ... Zheng, B. (2022). Global Carbon Budget 2022. *Earth System Science*  
919 *Data*, *14*(11), 4811–4900. doi: 10.5194/essd-14-4811-2022
- 920 Gan, B., Yu, J., Wu, L., Danabasoglu, G., Small, R. J., Baker, A. H., ... Chen,  
921 Z. (2023). North Atlantic subtropical mode water formation controlled  
922 by Gulf Stream fronts. *National Science Review*, *10*(9), nwad133. doi:  
923 10.1093/nsr/nwad133
- 924 Garric, G., & Parent, L. (2017). *Quality information document for global ocean*  
925 *reanalysis products GLOBAL-REANALYSIS-PHY-001-025* (Tech. Rep. No.  
926 CMEMS-GLO-QUID-001-025). Copernicus Marine Service. Retrieved 2023-  
927 09-18, from [https://catalogue.marine.copernicus.eu/documents/QUID/](https://catalogue.marine.copernicus.eu/documents/QUID/CMEMS-GLO-QUID-001-025.pdf)  
928 [CMEMS-GLO-QUID-001-025.pdf](https://catalogue.marine.copernicus.eu/documents/QUID/CMEMS-GLO-QUID-001-025.pdf)
- 929 Gary, S. F., Lozier, M. S., Kwon, Y.-O., & Park, J. J. (2014). The fate of North  
930 Atlantic Subtropical Mode Water in the FLAME model. *Journal of Physical*  
931 *Oceanography*, *44*(5), 1354–1371. doi: 10.1175/JPO-D-13-0202.1
- 932 Good, S. A., Martin, M. J., & Rayner, N. A. (2013). EN4: Quality controlled ocean  
933 temperature and salinity profiles and monthly objective analyses with uncer-  
934 tainty estimates: THE EN4 DATA SET. *Journal of Geophysical Research:*  
935 *Oceans*, *118*(12), 6704–6716. doi: 10.1002/2013JC009067
- 936 Gruber, N., Sarmiento, J. L., & Stocker, T. F. (1996). An improved method for de-  
937 tecting anthropogenic CO<sub>2</sub> in the oceans. *Global Biogeochemical Cycles*, *10*(4),  
938 809–837. doi: 10.1029/96GB01608
- 939 Hanawa, K., & Talley, L. D. (2001). Mode Waters. In G. Siedler, J. Church,  
940 & W. J. Gould (Eds.), *Ocean circulation and climate: Observing and mod-*  
941 *elling the global ocean* (pp. 373–386). San Diego: Academic Press. doi:  
942 10.1016/S0074-6142(01)80129-7
- 943 Hewitt, H. T., Roberts, M., Mathiot, P., Biastoch, A., Blockley, E., Chassignet,  
944 E. P., ... Zhang, Q. (2020). Resolving and Parameterising the Ocean  
945 Mesoscale in Earth System Models. *Current Climate Change Reports*, *6*(4),  
946 137–152. doi: 10.1007/s40641-020-00164-w
- 947 Joyce, T. M. (2012). New perspectives on Eighteen-Degree Water formation in the  
948 North Atlantic. *Journal of Oceanography*, *68*(1), 45–52. doi: 10.1007/s10872  
949 -011-0029-0
- 950 Joyce, T. M., Thomas, L. N., Dewar, W. K., & Girton, J. B. (2013). Eighteen De-  
951 gree Water formation within the Gulf Stream during CLIMODE. *Deep Sea Re-*  
952 *search Part II: Topical Studies in Oceanography*, *91*, 1–10. doi: 10.1016/j.dsr2  
953 .2013.02.019

- 954 Key, R. M., Kozyr, A., Sabine, C. L., Lee, K., Wanninkhof, R., Bullister, J. L., . . .  
 955 Peng, T.-H. (2004). A global ocean carbon climatology: Results from global  
 956 data analysis project (GLODAP). *Global Biogeochemical Cycles*, *18*(4). doi:  
 957 10.1029/2004GB002247
- 958 Klein, B., & Hogg, N. (1996). On the variability of 18 Degree Water forma-  
 959 tion as observed from moored instruments at 55°W. *Deep Sea Re-*  
 960 *search Part I: Oceanographic Research Papers*, *43*(11-12), 1777–1806. doi:  
 961 10.1016/S0967-0637(96)00069-6
- 962 Krémeur, A.-S., Lévy, M., Aumont, O., & Reverdin, G. (2009). Impact of the  
 963 subtropical mode water biogeochemical properties on primary production in  
 964 the North Atlantic: New insights from an idealized model study. *Journal of*  
 965 *Geophysical Research*, *114*(C7), C07019. doi: 10.1029/2008JC005161
- 966 Kwon, Y.-O., Park, J.-J., Gary, S. F., & Lozier, M. S. (2015). Year-to-year  
 967 reoutcropping of Eighteen Degree Water in an eddy-resolving ocean sim-  
 968 ulation. *Journal of Physical Oceanography*, *45*(4), 1189–1204. doi:  
 969 10.1175/JPO-D-14-0122.1
- 970 Kwon, Y.-O., & Riser, S. C. (2004). North Atlantic Subtropical Mode Water: A his-  
 971 tory of ocean-atmosphere interaction 1961–2000. *Geophysical Research Letters*,  
 972 *31*(19), L19307. doi: 10.1029/2004GL021116
- 973 Lan, X., Tans, P., Thoning, K., & NOAA Global Monitoring Laboratory. (2023).  
 974 *Trends in globally-averaged CO<sub>2</sub> determined from NOAA Global Monitoring*  
 975 *Laboratory measurements*. NOAA GML. doi: 10.15138/9N0H-ZH07
- 976 Levine, N. M., Doney, S. C., Lima, I., Wanninkhof, R., Bates, N. R., & Feely, R. A.  
 977 (2011). The impact of the North Atlantic Oscillation on the uptake and accu-  
 978 mulation of anthropogenic CO<sub>2</sub> by North Atlantic Ocean mode waters. *Global*  
 979 *Biogeochemical Cycles*, *25*, GB3022. doi: 10.1029/2010GB003892
- 980 Lévy, M., Couespel, D., Haëck, C., Keerthi, M., Mangolte, I., & Prend, C. J.  
 981 (2024). The impact of fine-scale currents on biogeochemical cycles in a  
 982 changing ocean. *Annual Review of Marine Science*, *16*(1). Retrieved from  
 983 <https://doi.org/10.1146/annurev-marine-020723-020531> (PMID:  
 984 37352844) doi: 10.1146/annurev-marine-020723-020531
- 985 Lévy, M., Ferrari, R., Franks, P. J. S., Martin, A. P., & Rivière, P. (2012). Bringing  
 986 physics to life at the submesoscale. *Geophysical Research Letters*, *39*, 13. doi:  
 987 10.1029/2012GL052756
- 988 Li, K., Maze, G., & Mercier, H. (2022). Ekman transport as the driver of extreme  
 989 interannual formation rates of Eighteen Degree Water. *Journal of Geophysical*  
 990 *Research: Oceans*, *127*(1). doi: 10.1029/2021JC017696
- 991 Madec, G., Benschila, R., Bricaud, C., Coward, A., Dobricic, S., Furner, R., & Oddo,  
 992 P. (2013). NEMO ocean engine (Computer software manual No. 27). Zenodo.  
 993 doi: 10.5281/zenodo.1464817
- 994 Mahadevan, A. (2016). The impact of submesoscale physics on primary productivity  
 995 of plankton. *Annual Review of Marine Science*, *8*(1), 161–184. doi: 10.1146/  
 996 annurev-marine-010814-015912
- 997 Maze, G., Forget, G., Buckley, M., Marshall, J., & Cerovecki, I. (2009). Using trans-  
 998 formation and formation maps to study the role of air–sea heat fluxes in North  
 999 Atlantic Eighteen Degree Water formation. *Journal of Physical Oceanography*,  
 1000 *39*(8), 1818–1835. doi: 10.1175/2009JPO3985.1
- 1001 McDougall, T. J., & Barker, P. M. (2011). *Getting started with TEOS-10 and the*  
 1002 *Gibbs Seawater (GSW) Oceanographic Toolbox*. SCOR/IAPSO WG127.
- 1003 McGillicuddy, D. J., Robinson, A. R., Siegel, D. A., Jannasch, H. W., Johnson,  
 1004 R., Dickey, T. D., . . . Knap, A. H. (1998). Influence of mesoscale eddies  
 1005 on new production in the Sargasso Sea. *Nature*, *394*(6690), 263–266. doi:  
 1006 10.1038/28367
- 1007 National Oceanographic Data Center (U.S.) Ocean Climate Laboratory, Conkright,  
 1008 M. E., Locarnini, R. A., Garcia, H. E., O’Brien, T. D., Boyer, T. P., . . .

- 1009 Antonov, J. I. (2002). *World Ocean Atlas 2001 : objective analyses, data*  
 1010 *statistics, and figures: CD-ROM documentation* [Technical Report]. Retrieved  
 1011 from <https://repository.library.noaa.gov/view/noaa/1174>
- 1012 Nelson, N., Siegel, D., & Yoder, J. (2004). The spring bloom in the northwest-  
 1013 ern Sargasso Sea: Spatial extent and relationship with winter mixing. *Deep Sea*  
 1014 *Research Part II: Topical Studies in Oceanography*, *51*(10-11), 987–1000. doi:  
 1015 10.1016/S0967-0645(04)00096-7
- 1016 Palter, J. B., Lozier, M. S., & Barber, R. T. (2005). The effect of advection on the  
 1017 nutrient reservoir in the North Atlantic subtropical gyre. *Nature*, *437*(7059),  
 1018 687–692. doi: 10.1038/nature03969
- 1019 Perruche, C., Szczypta, C., Paul, J., & Drévilion, M. (2019). *Quality information*  
 1020 *document global production centre GLOBAL\_REANALYSIS\_BIO\_001\_029*  
 1021 (Tech. Rep. No. CMEMS-GLO-QUID-001-029). Copernicus Marine Service.  
 1022 Retrieved 2023-09-19, from [https://catalogue.marine.copernicus.eu/](https://catalogue.marine.copernicus.eu/documents/QUID/CMEMS-GLO-QUID-001-029.pdf)  
 1023 [documents/QUID/CMEMS-GLO-QUID-001-029.pdf](https://catalogue.marine.copernicus.eu/documents/QUID/CMEMS-GLO-QUID-001-029.pdf)
- 1024 Pickard, R. (2022). [Dataset] *CTD and DIC bottle data from Cruise 316N151.3,*  
 1025 *WHP netCDF*. Version: WHP netCDF. CCHDO. Retrieved from [https://](https://cchdo.ucsd.edu/cruise/316N151.3)  
 1026 [cchdo.ucsd.edu/cruise/316N151.3](https://cchdo.ucsd.edu/cruise/316N151.3) (Accessed on 1 March 2023)
- 1027 Reagan, J. R., & NOAA National Centers for Environmental Information. (2023).  
 1028 [Dataset] *World Ocean Atlas 2023, NCEI Accession 0282728, Temperature*  
 1029 *- statistical mean on 1/4° grid for 1991-2020*. NOAA National Centers for  
 1030 Environmental Information. Retrieved from [https://www.ncei.noaa.gov/](https://www.ncei.noaa.gov/archive/accession/0282728)  
 1031 [archive/accession/0282728](https://www.ncei.noaa.gov/archive/accession/0282728) (Accessed on 1 March 2023)
- 1032 Reijnders, D., Deleersnijder, E., & Sebille, E. (2022). Simulating lagrangian subgrid-  
 1033 scale dispersion on neutral surfaces in the ocean. *Journal of Advances in Mod-*  
 1034 *eling Earth Systems*, *14*(2). doi: 10.1029/2021MS002850
- 1035 Sarmiento, J. L., & Gruber, N. (2006). *Ocean biogeochemical dynamics*. Princeton:  
 1036 Princeton university press.
- 1037 Siedler, G., Kuhl, A., & Zenk, W. (1987). The Madeira Mode Water. *Journal*  
 1038 *of Physical Oceanography*, *17*(10), 1561–1570. doi: 10.1175/1520-0485(1987)  
 1039 017(1561:TMMW)2.0.CO;2
- 1040 Siegel, D. A., McGillicuddy, D. J., & Fields, E. A. (1999). Mesoscale eddies, satellite  
 1041 altimetry, and new production in the Sargasso Sea. *Journal of Geophysical Re-*  
 1042 *search: Oceans*, *104*(C6), 13359–13379. doi: 10.1029/1999JC900051
- 1043 Spall, M. A. (1992). Cooling Spirals and Recirculation in the Subtropical  
 1044 Gyre. *Journal of Physical Oceanography*, *22*(5), 564–571. doi: 10.1175/  
 1045 1520-0485(1992)022(0564:CSARIT)2.0.CO;2
- 1046 Stevens, S. W., Johnson, R. J., Maze, G., & Bates, N. R. (2020). A recent decline  
 1047 in North Atlantic subtropical mode water formation. *Nature Climate Change*,  
 1048 *10*(4), 335–341. doi: 10.1038/s41558-020-0722-3
- 1049 Sugimoto, S., Hanawa, K., Watanabe, T., Suga, T., & Xie, S.-P. (2017). Enhanced  
 1050 warming of the subtropical mode water in the North Pacific and North At-  
 1051 lantic. *Nature Climate Change*, *7*(9), 656–658. doi: 10.1038/nclimate3371
- 1052 Swift, J., Feely, R., & Wanninkhof, R. (2022). [Dataset] *CTD and DIC bottle data*  
 1053 *from Cruise 33AT20120419, WHP netCDF*. Version: WHP netCDF. CCHDO.  
 1054 Retrieved from <https://cchdo.ucsd.edu/cruise/33AT20120419> (Accessed  
 1055 on 1 March 2023)
- 1056 Talley, L. D., & Raymer, M. E. (1982). Eighteen Degree Water variability. *Journal*  
 1057 *of Marine Research*, *40*, 757–775.
- 1058 Toole, J., & MacDonald, A. (2022). [Dataset] *CTD and DIC bottle data from Cruise*  
 1059 *316N200309, WHP netCDF*. Version: WHP netCDF. CCHDO. Retrieved from  
 1060 <https://cchdo.ucsd.edu/cruise/316N200309> (Accessed on 1 March 2023)
- 1061 Van Sebille, E., Kehl, C., Lange, M., Delandmeter, P., & The Parcels contrib-  
 1062 utors. (2023). [Software] *parcels 2.4.1*. Zenodo. Retrieved from  
 1063 <https://doi.org/10.5281/zenodo.7680187> doi: 10.5281/zenodo.7680187

- 1064 Williams, R. G., & Follows, M. (2011). *Ocean Dynamics and the Carbon Cycle*.  
1065 Cambridge University Press.
- 1066 Worthington, L. (1958). The 18° water in the Sargasso Sea. *Deep Sea Research*  
1067 (1953), 5(2-4), 297–305. doi: 10.1016/0146-6313(58)90026-1
- 1068 Xu, L., Xie, S.-P., McClean, J. L., Liu, Q., & Sasaki, H. (2014). Mesoscale eddy ef-  
1069 fects on the subduction of North Pacific mode waters. *Journal of Geophysical*  
1070 *Research: Oceans*, 119(8), 4867–4886. doi: 10.1002/2014JC009861

# Supporting Information for “Disentangling Carbon Concentration Changes Along Pathways of North Atlantic Subtropical Mode Water”

Daan Reijnders<sup>1</sup>, Dorothee C. E. Bakker<sup>2</sup>, Erik van Sebille<sup>1</sup>

<sup>1</sup>Institute for Marine and Atmospheric research Utrecht, Utrecht University, Utrecht, the Netherlands

5      <sup>2</sup>Centre for Ocean and Atmospheric Sciences, School of Environmental Sciences, University of East Anglia, Norwich, United Kingdom

## Contents of this file

1. Text S1. Model–Observation Comparison
2. Text S2. NASTMW Definition Sensitivity Analysis
- 10 3. Text S3. Subduction at Longer Integration Times
4. Text S4. Sensitivity of  $\Delta\rho$  for Export
5. Text S5. Varying Smoothing Window Widths
6. Text S6. Statistics for All Trajectories
7. Figures S1 to S43

## 15 **Text S1. Model–Observation Comparison**

To compare the FREEGLORYS2V4 and FREEBIORYS2V4 products to observations, we compare modeled temperature, salinity, temperature stratification, and DIC concentrations to observed bottle (DIC) and CTD (temperature, salinity, and temperature strat-

---

ification) data from the WOCE/CLIVAR A20 section along  $\sim 52^\circ\text{W}$  (see Figure S1). This approach is similar to that of Kwon, Park, Gary, and Lozier (2015). These observational data come from three cruises across two decades: in 1997 (Pickard, 2022), 2003 (Toole & MacDonald, 2022), and 2012 (Swift et al., 2022). In this section, we also compare locations of modeled and observed NASTMW. The criteria used to define modeled NASTMW are partly motivated by these findings, as well as on the sensitivity analysis in Text S2.

We focus on the region between  $15^\circ\text{N}$  to  $40^\circ\text{N}$ , considering depths up to 600 m. Figures S2, S3, and S4 show model-observation comparisons for temperature, salinity, and temperature stratification for A20 sections in 1997, 2003, and 2012 respectively. Here we also indicate NASTMW using a temperature and stratification constraint (section 2.2 of the main text defines the criteria used in the rest of this study). Here the maximum stratification criterion for observations is somewhat increased, and thus ‘relaxed’, with respect to the weaker maximum stratification of  $0.006^\circ\text{C m}^{-1}$  used by Kwon et al. (2015). This is because with  $0.006^\circ\text{C m}^{-1}$  we barely detected NASTMW for observations in 2003 and 2012. We apply a 20 m rolling mean to the observed temperature stratification to smooth out small measurement errors.

As can be seen, the model includes NASTMW with a typical minimum in temperature stratification. Overall, model temperature biases are reasonably small, with slightly positive biases north of  $30^\circ\text{N}$  and negative biases south of this latitude. Salinity biases in the observed NASTMW region are generally negative. The model also exhibits a higher temperature stratification in the observed NASTMW region. Stratification minima coinciding with NASTMW are at slightly shallower depths. Note that the observed NASTMW here exhibits a wedge-like structure. The warm bias south of  $30^\circ\text{N}$  and higher temperature

stratification are the main motivations for relaxing the temperature and stratification constraints in the model NASTMW definition. In Figure S2a & g, a cool bias in the region of low stratification would suggest that including temperature above 16 or 16.5 °C would better capture NASTMW in the model. However, in Figures S3a & g and Figures S4a & g, the 16–17 °C range is not included in the low stratification zone, while the range 19–20 °C is, coinciding with the model warm bias. Our choice to define the temperature range of 17–20.5 °C is a trade-off in choosing a relaxed temperature range that will most often coincide with the low-stratification criterion while ensuring the temperature range stays small enough to represent a homogeneous water mass. This is further motivated by the sensitivity analysis in Text S2. Overall, this yields realistic NASTMW volumes, thicknesses, and spatial extents.

We also compare modeled temperature and NASTMW with data from the World Ocean Atlas 2023 (WOA23; Reagan & NOAA National Centers for Environmental Information, 2023). We compute a model climatology for March and September between the years 1995 and 2017 – the model years used in this study. We compare this to the WOA23 climatology at 1/4° resolution, produced for the years 1991-2020. Figure S5 shows model temperature biases at 5, 200, and 500 m depths. It can readily be seen that the model does not correctly reproduce the Gulf Stream separation around Cape Hatteras, leading to a warm bias near the coastline further north. This is a known issue in ocean modeling (Bryan et al., 2007; Chassignet & Marshall, 2008). This also manifests itself in a model cold bias around 500 m depth just south of the modeled Gulf Stream. In the Sargasso Sea, temperature biases are slightly positive at 200 m depth and become slightly negative

at 500 m. This indicates a bias towards an increased temperature stratification, as was  
65 also found in the WOCE transects.

Additionally, the model exhibits an overall negative salinity bias in the region, which is especially pronounced in the surface layer (Fig. S6). Negative surface salinity biases are more commonly observed in coarse climate models (Flato et al., 2013; Park et al., 2016). A fresher upper ocean may lead to decreased DIC concentrations because freshwater  
70 input can locally dilute the DIC pool. Since we are interested in how mixing influences DIC concentrations, we do not apply salinity corrections in our main analyses (main text section 2.5), yet such a correction is warranted when comparing DIC concentrations between the model and observations.

To further investigate how the location of modeled NASTMW may differ from obser-  
75 vations, we plot the location of the climatological mixed layer depth (MLD) in March in Figure S7. Observations here are taken from WOA18 (Boyer et al., 2018). Regions of deep mixed layers in the northern part of the Sargasso Sea are possible NASTMW formation regions. As can be seen, the modeled mixed layer maximum in the Sargasso Sea is shallower than in observations. This is in line with the higher temperature stratification  
80 found in the previous model-observation comparisons. We expect model NASTMW to be mainly produced in the region of the 250-300 m maximum between 65°W and 50°W. In observations, mixed layer maxima around this depth extend further West, up to 70°W, meaning our NASTMW formation region is biased slightly eastward.

In Figure S8, we compare the climatological location of NASTMW in our model data  
85 (1995-2017) with climatological NASTMW in WOA23 (1991-2020). For WOA23 (S8a & b), we again use the NASTMW criterion of  $17^{\circ}\text{C} < T < 19^{\circ}\text{C}$  and  $\partial T/\partial z < 0.01^{\circ}\text{C m}^{-1}$ .

For the model, we use the adjusted temperature criterion of  $17^{\circ}\text{C} < T < 20.5^{\circ}\text{C}$ , applied to the climatological temperature (S8c & d) and applied to daily temperature fields, after which a climatological NASTMW is computed (S8e & f). In this case, we do not use  
90 any constraints for contiguity or specific layer thickness but do cut off NASTMW at  $35^{\circ}\text{W}$  to exclude Madeira mode water (main text section 2.2). The spatial distribution of NASTMW thickness computed from model climatological temperatures and computed from daily values here broadly agree, so we will use the NASTMW computed from the WOA temperature climatology as a proxy for the climatology of NASTMW itself. First,  
95 we can see that the model NASTMW has a core that is located more eastward, especially in September. In both the model and WOA case, the core is located south of the March MLD maximum (Figure S7a). Latitudinal extents of the model and WOA NASTMW agree. The NASTMW computed from WOA is thicker at the core (compared to Figure S7e), which again can be explained through the increased stratification in the model. Note that  
100 the WOA NASTMW is computed from fewer data points (for example transects and Argo-floats) than our climatological NASTMW, and this undersampling of a mean state makes the WOA NASTMW seem more controlled by mesoscale features. The summer spatial extent and thicknesses between WOA and the model broadly agree, which is important for initializing parcels over representative areas and depth ranges.

105 In summary, the FREEGLORYS2V4 NASTMW is produced through convective events associated with shallower MLD maxima and a slightly stronger vertical temperature stratification. This causes the modeled NASTMW to be thinner. The strong winter convection and NASTMW production site is located further eastward in comparison to observations. While ideally the locations between modeled and observed NASTMW would match, we

110 still use the modeled NASTMW for a process-level understanding of how DIC concentrations change along NASTMW pathways.

Lastly, we compare modeled DIC in FREEBIORYS2V4 to observed DIC concentrations using bottle data from the three A20 cruises, shown in Figure S9. Here, we also show salinity-normalized values of DIC (nDIC). This normalization is done by multiplying the 115 DIC by a factor  $S/S_{\text{ref}}$ , where  $S$  is the salinity and  $S_{\text{ref}} = 36$  psu. Quality-controlled bottle DIC values are converted from molality ( $\mu\text{mol kg}^{-1}$ ) to molar concentrations ( $\mu\text{mol L}^{-1}$ ), as used in this study. For this we use CTD temperatures and salinities in conjunction with the Thermodynamic Equation of Seawater 2010 (TEOS-10; McDougall & Barker, 2011). Note that the model and observations are both subject to variations of DIC 120 concentrations at fixed positions, due to internal variability. We therefore do not expect modeled concentrations to match one-on-one with observations. Instead, we are interested in the general distribution of DIC concentrations. While in 1997, there is good agreement of modeled and observed DIC concentration in the NASTMW region, observed DIC is higher in subsequent years. The salinity normalization causes an overall better agreement 125 between the model and observations taken in 2003 and 2012, as well as for the upper 200 meters in 1997. Overall, the vertical structure of increasing (n)DIC with depth is captured. Figure S10 compares the bottle and observed DIC values. While the mean DIC bias in 1997 is almost equal to a typical measurement precision of  $\sim 1 \mu\text{mol L}^{-1}$  (Sarmiento & Gruber, 2006), the bias between bottle and modeled DIC becomes more 130 negative over time, while the Pearson correlation coefficient remains steady at 0.92. This increase in model bias is partially due to the model salinity bias. Figure S11 shows a bottle-model comparison for nDIC. Figure S11a–c shows a smaller overall negative bias

for 2003 and 2012, while the bias for 1997 becomes positive. The distribution shows a wider spread for nDIC than for DIC (Fig. S10), meaning that salinity correction can lead to larger outliers due to bias multiplication when salinity and DIC biases have different causes. The linear regressions for nDIC (Fig. S11d–f) all have slopes smaller than 1, showing a model underestimation for high nDIC, while the overall correlation remains high with the Pearson-R ranging between 0.91-0.93. In the case of both DIC and nDIC, the model bias becomes more negative over time.

To further illustrate how FREEBIORYS2V4 responds to the prescribed increase of atmospheric  $p\text{CO}_2$ , Figure S12a shows the trend of DIC concentrations at 10 m depth. Trends are computed between 1995 and 2017 by applying a seasonal decomposition based on moving averages, followed by a linear regression. This shows an overall decrease in upper-ocean DIC, with a trend between 0 and  $-1 \mu\text{mol/L/year}$  in most of the Sargasso Sea. However, Figure S12b & c show that this is due to a modeled salinity decrease. Adjusting for this, the nDIC trend becomes positive in the Sargasso Sea and exhibits pronounced spatial variability.

Between 1988 and 2011, seasonally-detrended nDIC observations show a trend of  $+1.08 \pm 0.05 \mu\text{mol/kg/year}$  at the Bermuda Atlantic Time-series Study (BATS) site at  $31^\circ 40' \text{ N}$ ,  $64^\circ 10' \text{ W}$  and Hydrostation S at  $32^\circ 10' \text{ N}$ ,  $64^\circ 10' \text{ W}$  (Bates et al., 2012). Figure S12d shows a time series of model nDIC near the BATS site at 10 m depth, which exhibits a much smaller deseasonalized trend of  $0.2 \mu\text{mol/L/yr}$  while exhibiting notable interannual variability. Since the model's nDIC response to increasing atmospheric  $p\text{CO}_2$  in the Sargasso Sea is about a factor 5 weaker than observed, our dataset is not suitable for investigating changes in carbon fluctuations along NASTMW pathways due to rising

anthropogenic carbon emissions. Instead, we apply a process-based view that takes into account interannual variability without focusing on trends.

### **Text S2. NASTMW Definition Sensitivity Analysis**

We test the sensitivity of the modeled NASTMW in March and September to the following changes:

1. Lowering the maximum temperature stratification criterion, comparing  $0.01\text{ }^{\circ}\text{C m}^{-1}$  and  $0.006\text{ }^{\circ}\text{C m}^{-1}$ .

2. Varying the maximum temperature criterion, comparing  $19\text{ }^{\circ}\text{C}$ ,  $20\text{ }^{\circ}\text{C}$ ,  $20.5\text{ }^{\circ}\text{C}$  and  $21\text{ }^{\circ}\text{C}$ . The lowest value in this range is typical in literature (Kwon & Riser, 2004; Joyce et al., 2013), while  $20\text{ }^{\circ}\text{C}$  has been used in the modeling study by Kwon et al. (2015). The highest two values are included due to the model's warm bias in certain regions, as discussed in Text S1.

3. Lowering the minimum temperature criterion, comparing  $17\text{ }^{\circ}\text{C}$  and  $16.5\text{ }^{\circ}\text{C}$ , motivated by the model's cold bias in certain regions, as discussed in Text S1.

Since it is computationally expensive to compute climatologies of NASTMW for each of these combinations, we instead apply these criteria to climatologies of the model temperature for March and September (1995-2017). The results are shown in Figure S13. As in Figure S8, we do not consider individual layer thickness or contiguity here. It can immediately be seen that a maximum stratification criterion of  $0.006\text{ }^{\circ}\text{C m}^{-1}$  yields NASTMW that is too thin when compared to observed core thickness of around 300–400 m in the literature (Kwon & Riser, 2004; Fratantoni et al., 2013; Billheimer & Talley, 2016). This emphasizes the need to increase the maximum stratification criterion to  $0.01\text{ }^{\circ}\text{C m}^{-1}$ . The effect of increasing the upper temperature boundary can be seen as the NASTMW region

increases towards the south-west. This means that the temperature criterion provides  
180 the main limiting factor for being defined as NASTMW in this southwestern sector. The  
difference between the lower temperature boundaries of  $16.5^{\circ}\text{C}$  and  $17^{\circ}\text{C}$  is rather small,  
as is the difference between the upper boundaries  $20.5^{\circ}\text{C}$  and  $21^{\circ}\text{C}$ . The temperature  
range of  $17^{\circ}\text{C} < T < 20.5^{\circ}\text{C}$  indeed seems a good trade-off between often coinciding with  
the low-stratification region, while at the same time keeping the total temperature range  
185 somewhat limited to reflect the homogeneity of NASTMW.

The contiguity and individual layer thickness constraints (main text Section 2.2), also  
affect the total NASTMW volume. To test the sensitivity of the NASTMW volume to  
these constraints, we compute the volume using only the temperature and stratification  
criteria and compare this to the volume when adding the thickness and contiguity cri-  
190 teria. Figure S14 shows that the volume experiences a pronounced seasonal cycle. The  
average yearly minimum volume is  $4.1 \times 10^{14} \text{ m}^3$ , while the average yearly maximum is  
 $9.0 \times 10^{14} \text{ m}^3$ . This is close to the value of  $9.1 \times 10^{14} \text{ m}^3$  found by Joyce (2012) using a  
temperature and salinity constraint. The seasonal NASTMW production of  $4.9 \times 10^{14} \text{ m}^3$   
is higher than the  $2.7 \times 10^{14} \text{ m}^3$  (8.6 Svy, where  $1 \text{ Svy} \approx 3.15 \times 10^{13} \text{ m}^3$ ) found by Forget,  
195 Maze, Buckley, and Marshall (2011), which was found without a stratification constraint.  
When that constraint is absent, NASTMW production and destruction happen mostly  
through cooling and warming due to air-sea heat fluxes and vertical mixing, while the  
pronounced seasonal effects of stratification creation and destruction are ignored. In gen-  
eral, NASTMW volumes are highly sensitive to the criteria used (Joyce, 2012). Note,  
200 however, that the added thickness and contiguity criteria can help us eliminate small,

spurious NASTMW volumes, without changing the total volume much when compared to the seasonal cycle.

### **Text S3. Subduction at Longer Integration Times**

In the main text, we discussed NASTMW parcels that subducted within the previous year. Here we investigate the effect of including NASTMW parcels that have subducted from the mixed layer on September 1st over the course of two (Figs. S15 & S16), and three years (Figs. S17 & S18), such that they end up in NASMTW again at September 1st. In both cases, the order of magnitude of the total  $\Delta\text{DIC}$  is similar to that of subduction over the course of one year ( $110\ \mu\text{mol L}^{-1}$  for two and three years, compared to  $101\ \mu\text{mol L}^{-1}$  for one year). While we see an increase in the contribution of soft-tissue, carbonate, and residual terms, mixing fluxes are still dominant in setting the DIC concentration. This suggests that also at larger time scales, adjustment to the ambient water column condition is the main determinant for setting DIC concentrations of subducting NASTMW parcels. However, the increased contribution of biogeochemistry indicates that the parcel's DIC concentrations are to a larger extent influenced directly by soft-tissue remineralization, which shapes the ambient vertical structure of DIC in the water column.

The distribution of total  $\Delta\text{DIC}$  (Figs. S15a & S17a) has a tail that extends to larger extremes than during subduction over 1 year (main text Fig. 4). When considering longer subduction timescales, backward-tracked parcels can come from a much larger region. Parcels in the right tail of the distribution are found to come from areas where mixed-layer DIC concentrations are generally lower, including for example the Caribbean Sea.

Looking at the timescales of enrichment and depletion regimes (Figs. S16 & S18), we notice that distributions of regime timescales are similar, although with a thinner tail at longer timescales: as subduction occurs over longer timescales, downwelling and the associated steady increase of DIC can be more variable as the parcel travels from the mixed layer to NASTMW. This causes longer periods of enrichment to be more easily interspersed by depletion.

#### **Text S4. Sensitivity of $\Delta\rho$ for Export Pathways**

Figures S19 – S22 show the results for exported parcels, where we use  $\Delta\sigma = 0 \text{ kg m}^{-3}$  and  $0.05 \text{ kg m}^{-3}$  instead of  $\Delta\sigma = 0.01 \text{ kg m}^{-3}$  as used in the main text. When we lower  $\Delta\sigma$  to  $0 \text{ kg m}^{-3}$ , the number of parcels that are considered exported is reduced by about a factor 3 (from 15.3% to 4.7% of all parcels). When increasing  $\Delta\sigma$  to  $0.05 \text{ kg m}^{-3}$ , the number of parcels doubles to 30.6%. However, the distribution and mean of  $\Delta\text{DIC}$  in both cases remain approximately equal to that found for  $\Delta\sigma = 0.01 \text{ kg m}^{-3}$  (comparing Figures S19a-c and S21a-c to Figure 9a-c from the main text). This is also the case for the timescale distribution and magnitudes (comparing Figures S20 and S22 to Figure 10 in the main text). The monthly contributions exhibit similar patterns, although vary in magnitude, with ranges generally being stronger given stricter criteria (Figures S19d-f and S21d-f to Figure 9d-f from the main text). However, since the residual contributes significantly more to  $\Delta\text{DIC}$  in the export pathways than for the other NASMTW pathways, the disentanglement of the DIC rate of change into its components is less well-constrained.

#### **Text S5. Varying Smoothing Window Widths**

The width of the window by which we smooth our DIC anomaly time series will influence the timescales of the regimes that we detect using the method presented in section 2.6 of

the main text. After all, smoothing will filter out minor fluctuations in the DIC anomaly, such that, if they are small in magnitude, brief periods of enrichment and depletion are smoothed out. Inherently, the smoothing window width thus influences the timescale distributions that we find. In the main text, we focus on a window width of ten days.

250 Here, we show regime timescale results when we identify regimes without smoothing, as well as by applying a smoothing window of 6 and 20 days.

The results without smoothing are found in Fig. S23 (subduction), S24 (persistence), S25 (ventilation), and S26 (export). In each of the cases, we see that the distribution of depletion and enrichment timescales is largely concentrated at timescales of 10 days or  
255 less. The partitioning of the contribution of each process to the events, however, remains roughly similar at each timescale. For subduction, persistence, and export, we no longer see a net depletion at any timescale. In the case of a 10-day smoothing window, short depletion events would be interspersed with longer enrichment, causing net depletion for short scales (below 10 to 40 days, depending on the pathway), and enrichment at  
260 longer scales. Without smoothing, brief small depletion events are included that could be smoothed out for longer timescales. These brief depletion events can break up a steady background enrichment that would have been identified if timescale smoothing was applied. This thus serves to illustrate how smoothing acts as a lens by which small, brief fluctuations, which may be due to numerical noise, are ignored.

265 The results with 6-day smoothing are found in Fig. S27 (subduction), S28 (persistence), S29 (ventilation), S30 (export), while the results using a 20-day smoothing window are found in Fig. S31 (subduction), S32 (persistence), S33 (ventilation), S34 (export). When comparing these timescale distributions to those found using a 10-day smoothing window

in the main text, we see that generally speaking, the distributions are qualitatively similar, but with their modes and tails shifted towards longer timescales. This further illustrates how the smoothing window simply acts as a lens by which short-term fluctuations can be filtered out.

### **Text S6. Statistics for All Trajectories**

Figure S35 shows the  $\Delta$ DIC for all forward trajectories starting in NASTMW, while Figure S36 shows the distribution of associated enrichment and depletion timescales. From these two figures, it can be seen that mixing largely acts to deplete parcels of DIC. This is concentrated around the winter months when the mixed layer deepens (Fig. S35f). The soft-tissue contribution is dominated by the remineralization of organic material, mostly from March onward (Fig. S35f). Qualitatively, the monthly contributions of each term resemble those of persisting, ventilating, and exporting parcels. The net negative contribution of mixing and positive contributions of the biogeochemical terms are also qualitatively similar to these three pathways. The regimes with durations  $> 30$  days are largely made up of this (Fig S36a). Qualitatively, this distribution resembles that of parcels persisting of NASTMW (Main Text Fig. 7), which is the most prevalent pathway found in this study, albeit with a smaller tail in the longer regime durations.

Figure S37 shows the  $\Delta$ DIC for all backward trajectories ending up in NASTMW, while Figure S38 shows the distribution of associated enrichment and depletion timescales. The net effect of mixing is negative and that of soft-tissue processes is positive (Fig. S37c), similar to what we find for the forward trajectories. This corresponds to our finding that of our four pathways, the persistence pathway is the most occurring one, implying that many of the backward trajectories are, or are at least similar to, parcels that persisted in

NASTMW. Qualitatively this is also similar to what we see for ventilating parcels (Main Text Section 3.3). There are, however, two differences with the forward trajectories. First, the distribution of  $\Delta\text{DIC}$  in Figure S37 shows a long, thin positive tail, where the contribution of mixing becomes dominant towards the tail end. This corresponds to our findings for the subduction pathway with high mixing and high  $\Delta\text{DIC}$  (Main Text Section 3.1). Second, the positive mixing at timescales  $> 100$  days in this case (Fig. S38a) is larger than what we find for the persistence and ventilation pathways (Fig. 7a and 9), which is in agreement with a DIC enrichment through vertical mixing during subduction occurring at these longer timescales (Fig. 5a). This points toward the aggregate of all backward trajectories qualitatively resembling our findings for the forward trajectories, but with subduction superimposed.

## References

- Bates, N. R., Best, M. H. P., Neely, K., Garley, R., Dickson, A. G., & Johnson, R. J. (2012). Detecting anthropogenic carbon dioxide uptake and ocean acidification in the North Atlantic Ocean. *Biogeosciences*, *9*(7), 2509–2522. doi: 10.5194/bg-9-2509-2012
- Billheimer, S., & Talley, L. D. (2016). Annual cycle and destruction of eighteen degree water. *Journal of Geophysical Research: Oceans*, *121*(9), 6604–6617. doi: 10.1002/2016JC011799
- Boyer, T. P., García, H. E., Locarnini, R. A., Zweng, M. M., Mishonov, A. V., Reagan, J. R., ... Smolyar, I. V. (2018). *[Dataset] World Ocean Atlas 2018, Mixed Layer Depth - statistical mean on 1/4° grid for 2005-2017*. NOAA National Centers for En-

Environmental Information. Retrieved from <https://www.ncei.noaa.gov/archive/accession/NCEI-WOA18> (Accessed on 1 March 2023)

315 Bryan, F. O., Hecht, M. W., & Smith, R. D. (2007). Resolution convergence and sensitivity studies with North Atlantic circulation models. Part I: The western boundary current system. *Ocean Modelling*, *16*(3-4), 141–159. doi: 10.1016/j.ocemod.2006.08.005

320 Chassignet, E. P., & Marshall, D. P. (2008). Gulf Stream separation in numerical ocean models. In M. W. Hecht & H. Hasumi (Eds.), *Geophysical Monograph Series* (Vol. 177, pp. 39–61). Washington, D. C.: American Geophysical Union. doi: 10.1029/177GM05

Flato, G., Marotzke, J., Abiodun, B., Braconnot, P., Chou, S., Collins, W., ... Rummukainen, M. (2013). Evaluation of climate models. In T. Stocker et al. (Eds.), *Climate change 2013: The physical science basis. contribution of Working Group I to the fifth assessment report of the Intergovernmental Panel on Climate Change*. Cambridge, United Kingdom and New York, NY, USA: Cambridge University Press. Retrieved from <https://doi.org/10.1017/CB09781107415324> doi: 10.1017/CBO9781107415324

330 Forget, G., Maze, G., Buckley, M., & Marshall, J. (2011). Estimated Seasonal Cycle of North Atlantic Eighteen Degree Water Volume. *Journal of Physical Oceanography*, *41*(2), 269–286. doi: 10.1175/2010JPO4257.1

335 Fratantoni, D. M., Kwon, Y.-O., & Hodges, B. A. (2013). Direct observation of subtropical mode water circulation in the western North Atlantic Ocean. *Deep Sea Research Part II: Topical Studies in Oceanography*, *91*, 35–56. doi: 10.1016/j.dsr2.2013.02.027

- Joyce, T. M. (2012). New perspectives on Eighteen-Degree Water formation in the North Atlantic. *Journal of Oceanography*, *68*(1), 45–52. doi: 10.1007/s10872-011-0029-0
- Joyce, T. M., Thomas, L. N., Dewar, W. K., & Girton, J. B. (2013). Eighteen Degree Water formation within the Gulf Stream during CLIMODE. *Deep Sea Research Part II: Topical Studies in Oceanography*, *91*, 1–10. doi: 10.1016/j.dsr2.2013.02.019
- 340 Kwon, Y.-O., Park, J.-J., Gary, S. F., & Lozier, M. S. (2015). Year-to-year reoutcropping of Eighteen Degree Water in an eddy-resolving ocean simulation. *Journal of Physical Oceanography*, *45*(4), 1189–1204. doi: 10.1175/JPO-D-14-0122.1
- 345 Kwon, Y.-O., & Riser, S. C. (2004). North Atlantic Subtropical Mode Water: A history of ocean-atmosphere interaction 1961–2000. *Geophysical Research Letters*, *31*(19), L19307. doi: 10.1029/2004GL021116
- McDougall, T. J., & Barker, P. M. (2011). *Getting started with TEOS-10 and the Gibbs Seawater (GSW) Oceanographic Toolbox*. SCOR/IAPSO WG127.
- 350 Park, T., Park, W., & Latif, M. (2016). Correcting North Atlantic sea surface salinity biases in the Kiel Climate Model: Influences on ocean circulation and Atlantic Multidecadal Variability. *Climate Dynamics*, *47*(7-8), 2543–2560. doi: 10.1007/s00382-016-2982-1
- Pickard, R. (2022). *[Dataset] CTD and DIC bottle data from Cruise 316N151\_3, WHP netCDF*. Version: WHP netCDF. CCHDO. Retrieved from [https://cchdo.ucsd.edu/cruise/316N151\\_3](https://cchdo.ucsd.edu/cruise/316N151_3) (Accessed on 1 March 2023)
- 355 Reagan, J. R., & NOAA National Centers for Environmental Information. (2023). *[Dataset] World Ocean Atlas 2023, NCEI Accession 0282728, Temperature - statistical mean on 1/4° grid for 1991-2020*. NOAA National Centers for Environmental

360 Information. Retrieved from <https://www.ncei.noaa.gov/archive/accession/0282728> (Accessed on 1 March 2023)

Sarmiento, J. L., & Gruber, N. (2006). *Ocean biogeochemical dynamics*. Princeton: Princeton university press.

365 Swift, J., Feely, R., & Wanninkhof, R. (2022). [Dataset] *CTD and DIC bottle data from Cruise 33AT20120419, WHP netCDF*. Version: WHP netCDF. CCHDO. Retrieved from <https://cchdo.ucsd.edu/cruise/33AT20120419> (Accessed on 1 March 2023)

Toole, J., & MacDonald, A. (2022). [Dataset] *CTD and DIC bottle data from Cruise 316N200309, WHP netCDF*. Version: WHP netCDF. CCHDO. Retrieved from <https://cchdo.ucsd.edu/cruise/316N200309> (Accessed on 1 March 2023)

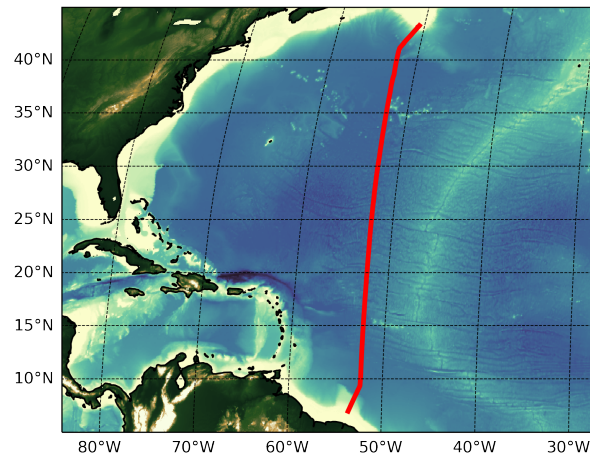


**Figure S1.** WOCE A20 section, used to compare CTD and bottle data with FREE-GLORYS2V4 (temperature, stratification, and salinity) and FREEBIORYS2V4 (DIC).

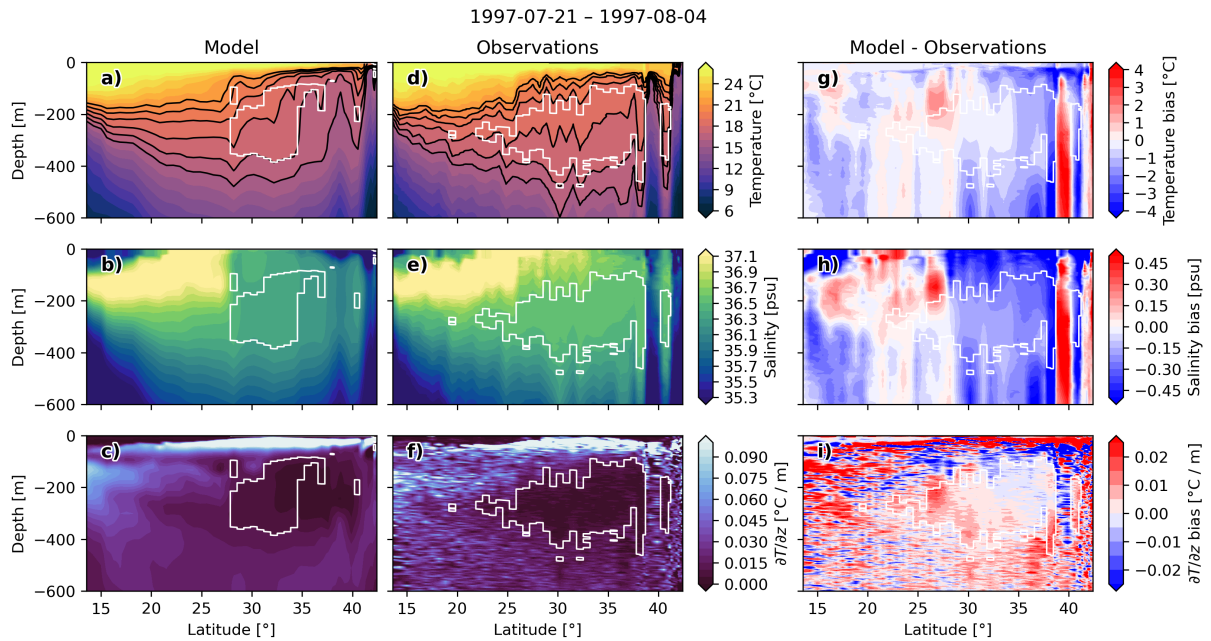


**Figure S2.** Model–observation comparison along the WOCE A20 section in 1997 at  $\sim 52^\circ\text{W}$  (Pickard, 2022). (a) Model temperature (b) salinity, and (c) temperature stratification snapshots are for 28 July 1997. White contours indicate modeled NASTMW with constraints  $17^\circ\text{C} < T < 20.5^\circ\text{C}$  and  $\partial T/\partial z < 0.01^\circ\text{C m}^{-1}$ . (d–f) show observed temperature, salinity and stratification at the corresponding observations along A20 between 21 Jul - 14 Aug 1997. Here the NASTMW constraint is follows a stricter typical definition:  $17^\circ\text{C} < T < 19^\circ\text{C}$  and  $\partial T/\partial z < 0.01^\circ\text{C m}^{-1}$ . Black lines in (a) and (d) indicate  $16 - 21^\circ\text{C}$  isotherms. (g–i) show the model bias (model - observations, with the NASTMW constraints from observations).

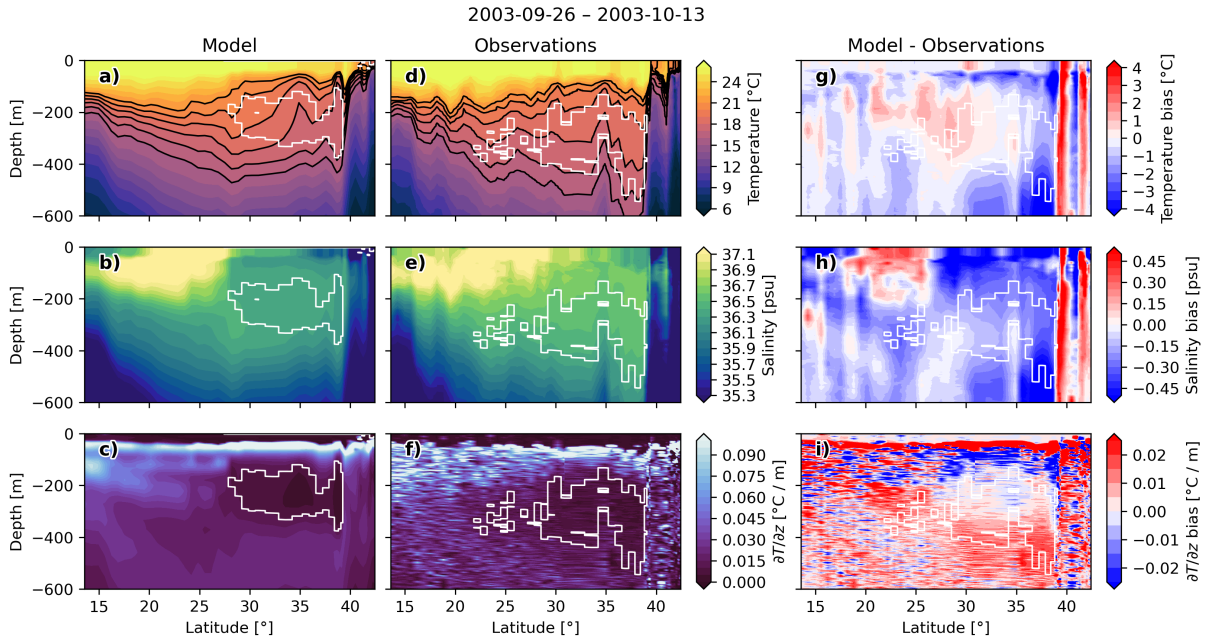


**Figure S3.** Similar to Figure S2, but for the CLIVAR A20 section in 2003 (Toole & MacDonald, 2022). Model sections (a–c) are taken at 3 October 2003. Observations (d–f) are taken between 26 September – 13 October 2003.

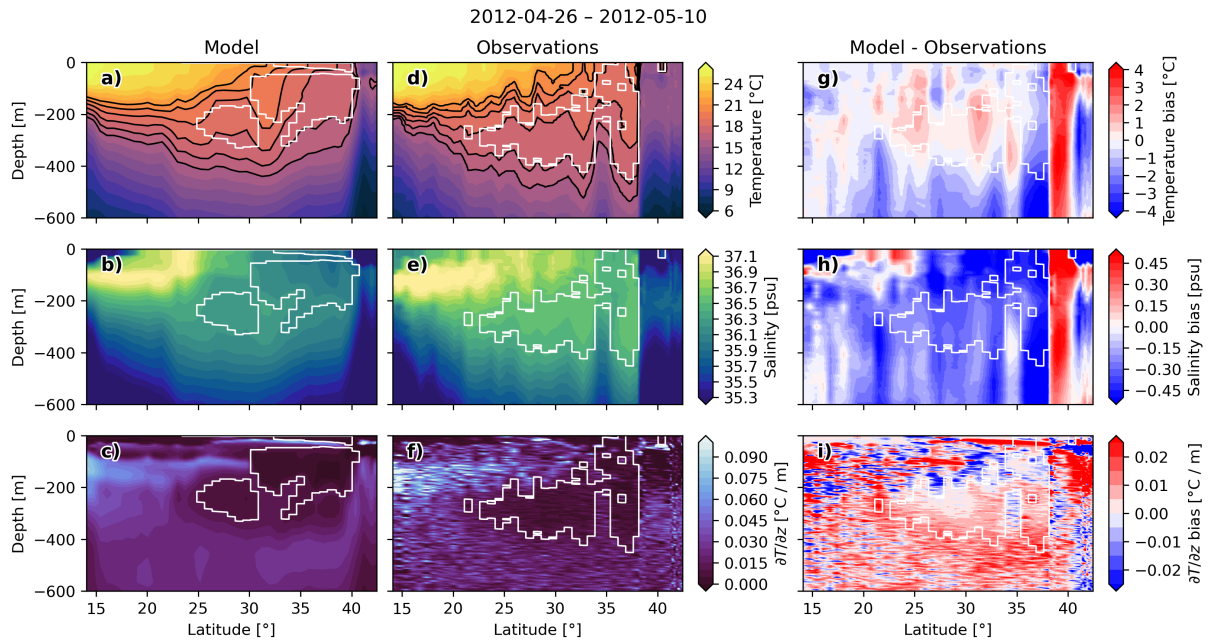


**Figure S4.** Similar to Figure S2, but for the CLIVAR A20 section in 2012 (Swift et al., 2022). Model sections (a–c) are taken at 2 May 2012. Observations (d–f) are taken between 26 April – 10 May 2012.

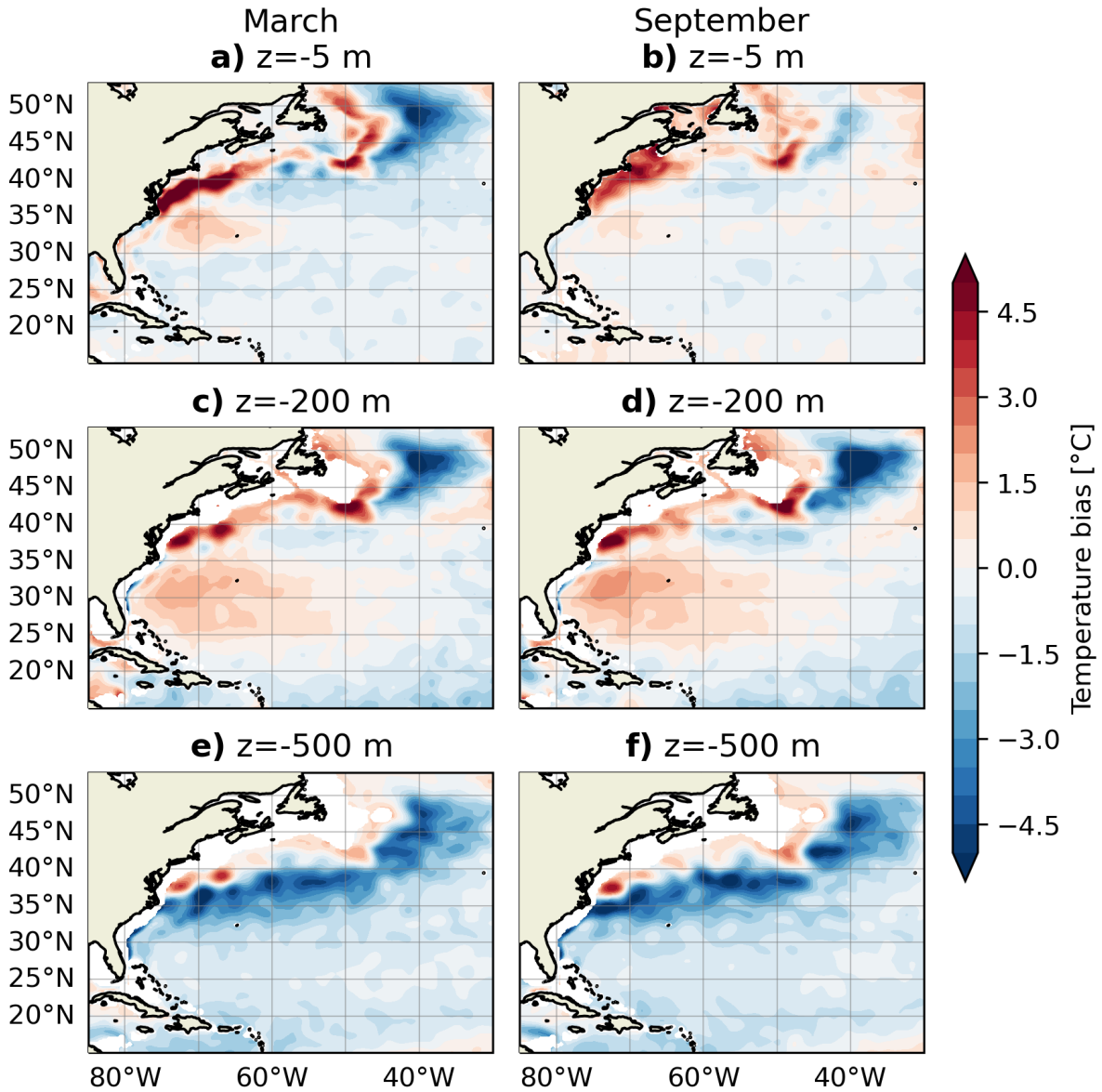


**Figure S5.** Model temperature bias. Computed by subtracting WOA23 climatological temperatures (1991–2020) from model temperature climatology (1995–2017).

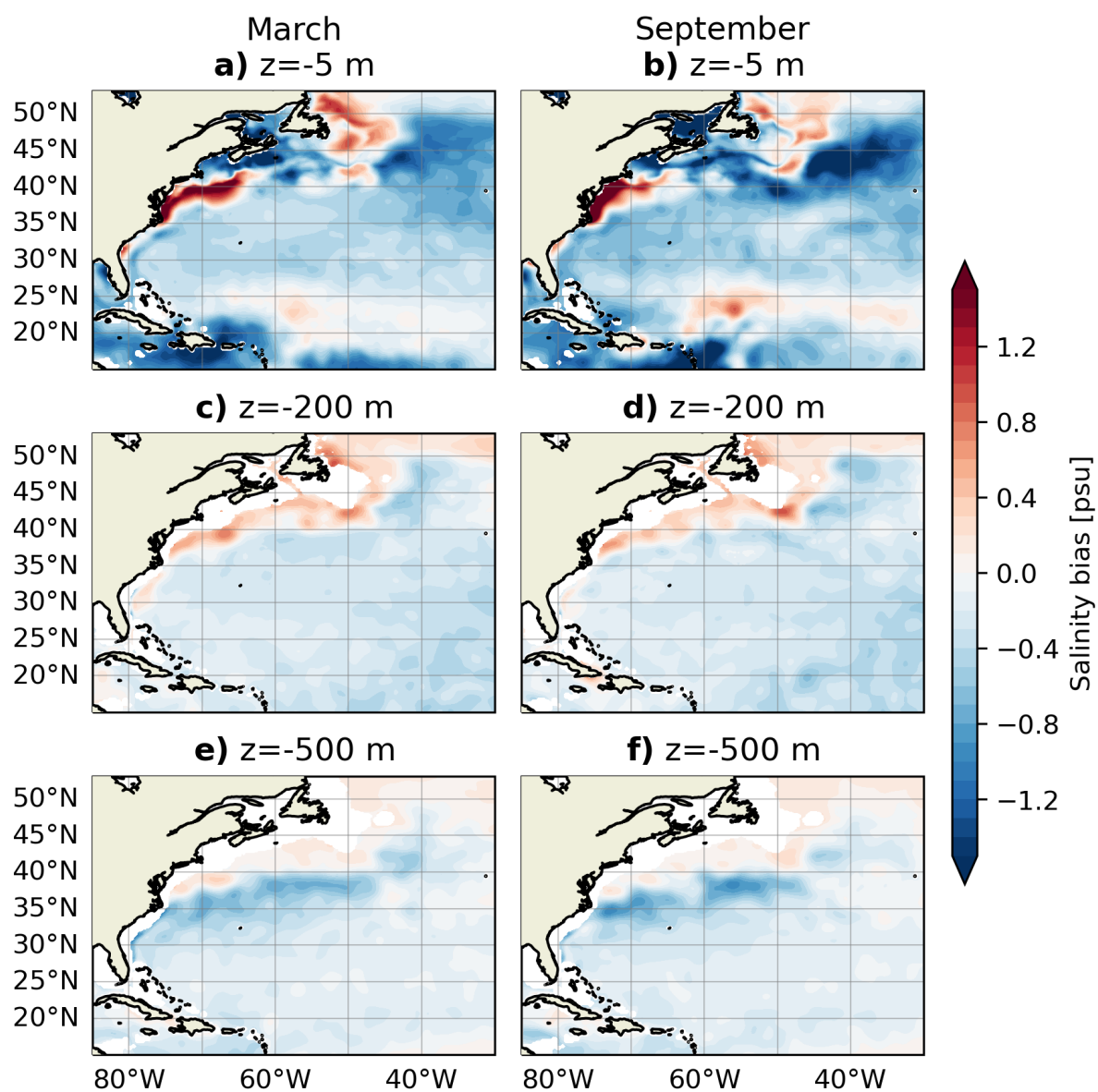


**Figure S6.** Model salinity bias. Computed by subtracting WOA23 climatological salinities (1991–2020) from model salinity climatology (1995–2017).

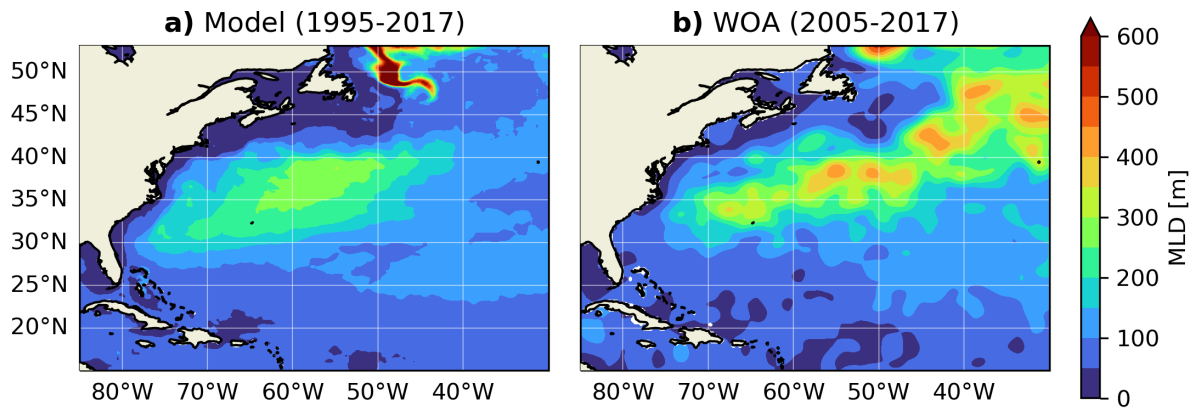


**Figure S7.** Climatological mixed layer depths from (a) FREEGLORYS2V4 (1995-2017) and (b) WOA18 (2005-2017).

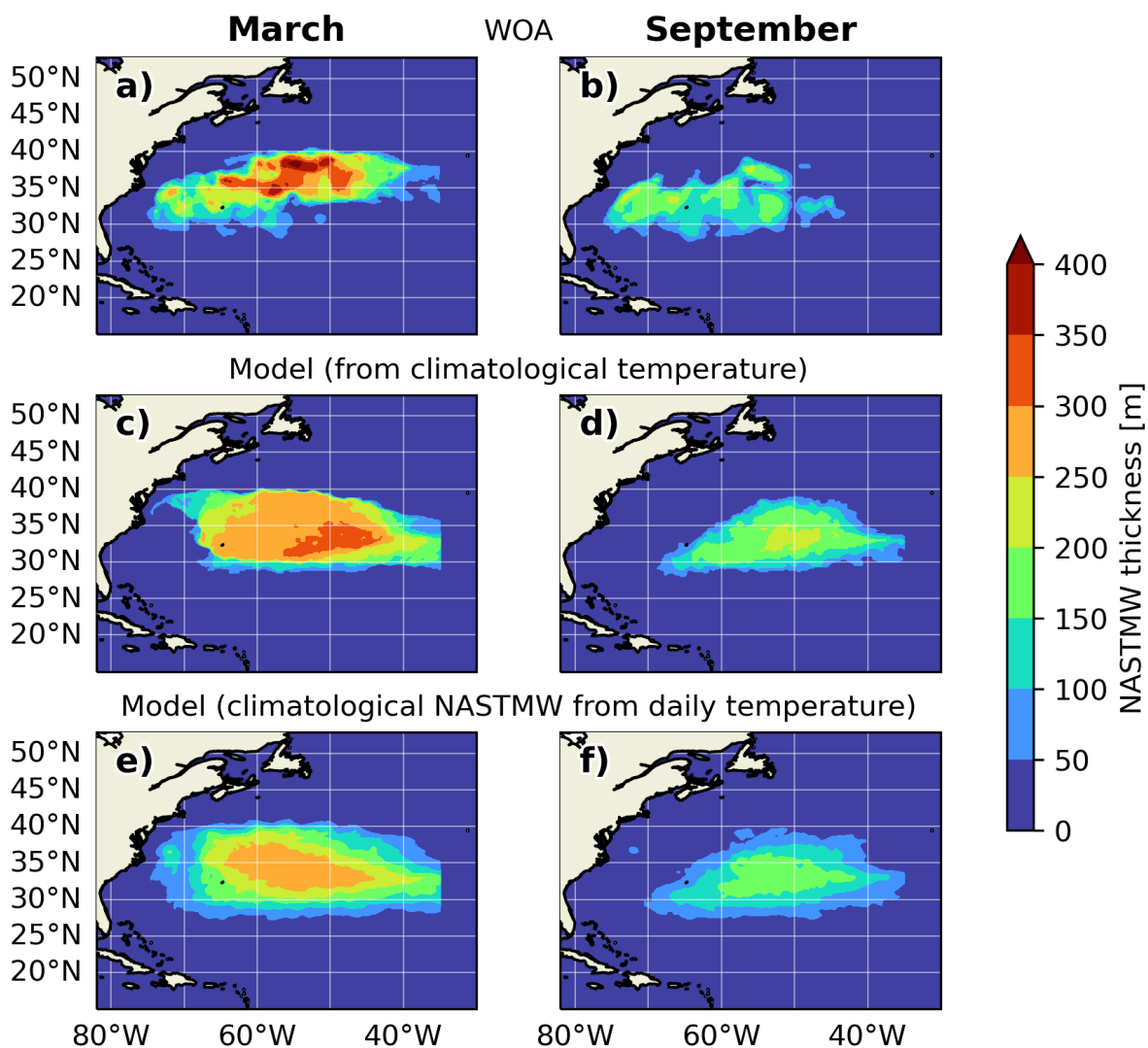


**Figure S8.** March and September NASTMW thickness computed using (a, b) WOA23 temperatures (1991-2020), and (c, d) climatological temperatures in FREEGLORYS2V4 (1995-2017). (e, f) Climatology of NASTMW computed from daily temperatures in FREEGLORYS2V4.

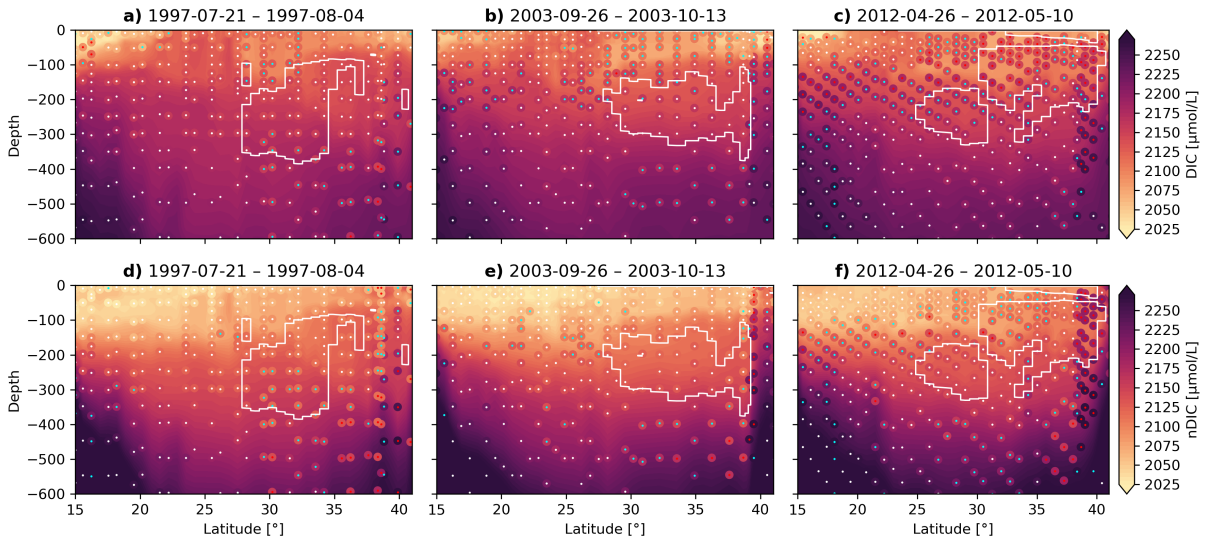


**Figure S9.** (a–c) Modeled and observed DIC concentrations along the A20 section. Modeled concentrations are plotted as a background field. Observations are plotted using colored dots. The center of the observations is marked white if the difference between the model and observations is less than  $25\ \mu\text{mol L}^{-1}$ , cyan if the difference is between  $25\ \mu\text{mol L}^{-1}$  and  $50\ \mu\text{mol L}^{-1}$  and red if the difference is larger than  $50\ \mu\text{mol L}^{-1}$ . Model DIC snapshots are taken at (a) 28 July 1997, (b) 3 October 2003, and (c) 2 May 2012. (d–f) Salinity-normalized DIC (nDIC) for the same dates. White contours indicate two of the NASTMW constraints in the modeled data:  $17^{\circ}\text{C} < T < 20.5^{\circ}\text{C}$  and  $\partial T/\partial z < 0.01^{\circ}\text{C m}^{-1}$ .

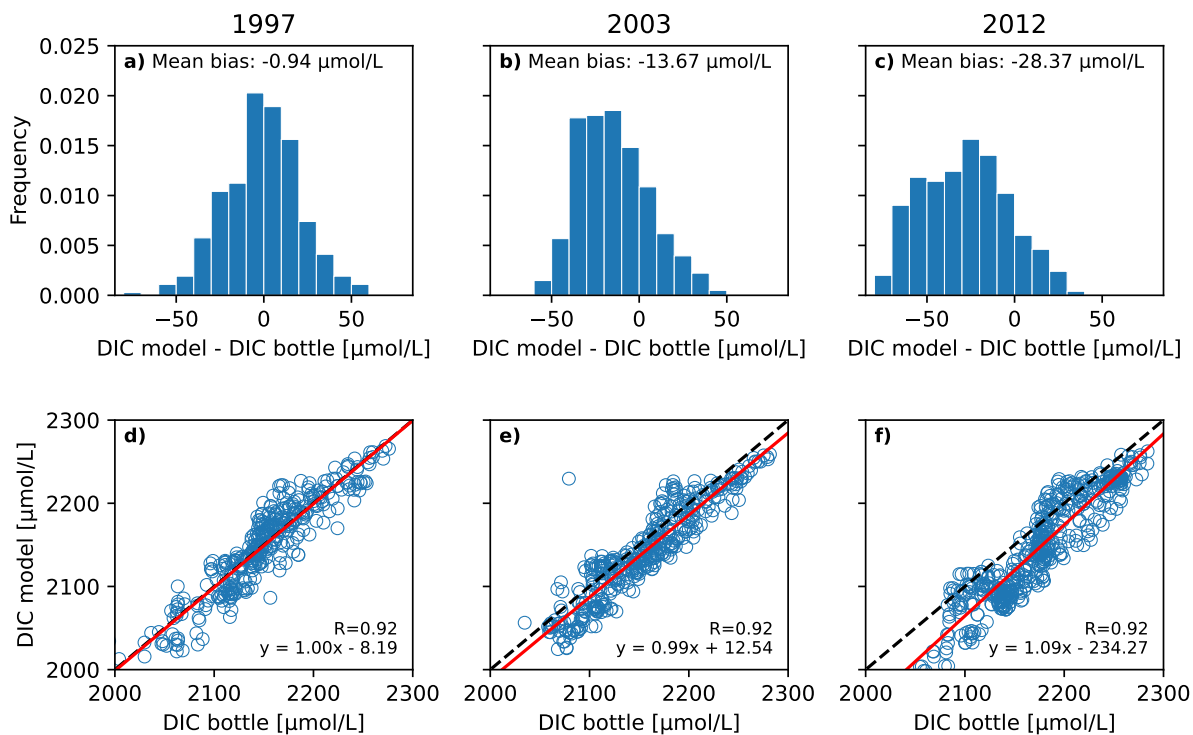


**Figure S10.** (a–c) Histograms with the difference in DIC between modeled and bottle DIC concentrations for each A20 transect year. Each observation is matched with the model DIC snapshot at the date and location of observation. (d–f) Scatter plot comparing observed and modeled DIC, including linear regression.  $R$  is the Pearson correlation coefficient.

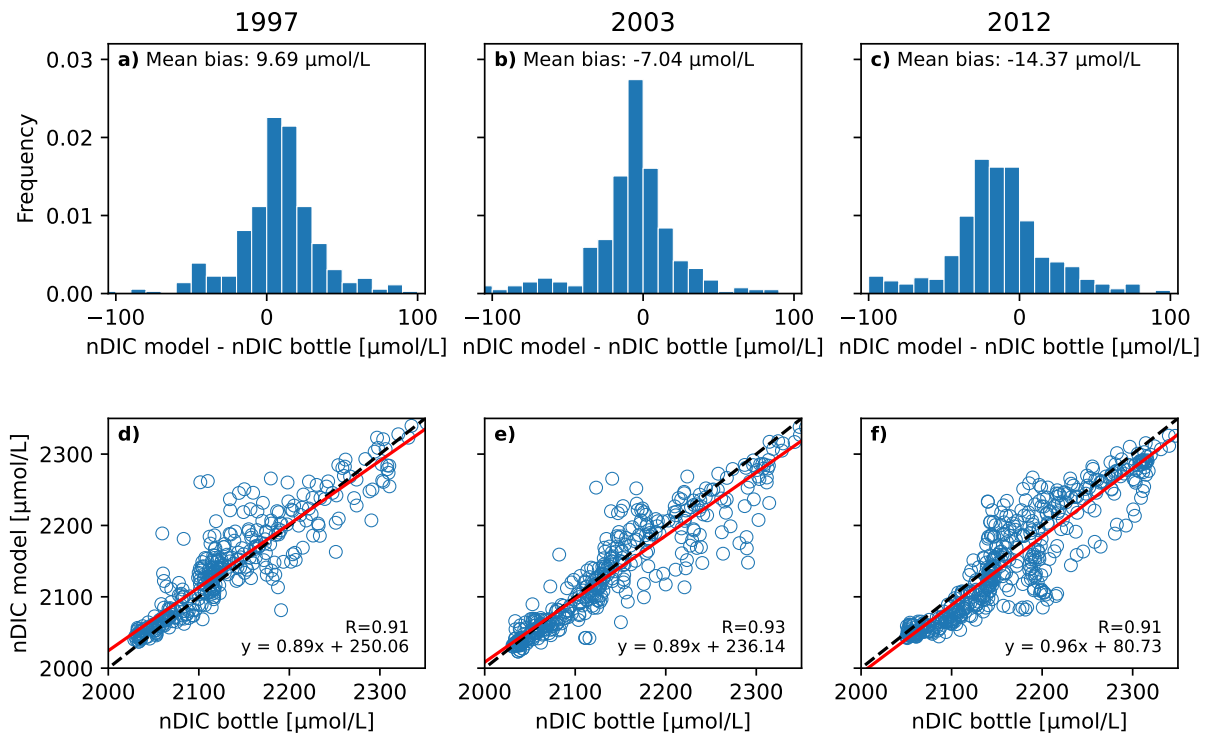


**Figure S11.** (a–c) Histograms with the difference in nDIC between modeled and bottle nDIC concentrations for each A20 transect year. Each observation is matched with the model nDIC snapshot at the date and location of observation. (d–f) Scatter plot comparing observed and modeled nDIC, including linear regression.  $R$  is the Pearson correlation coefficient.

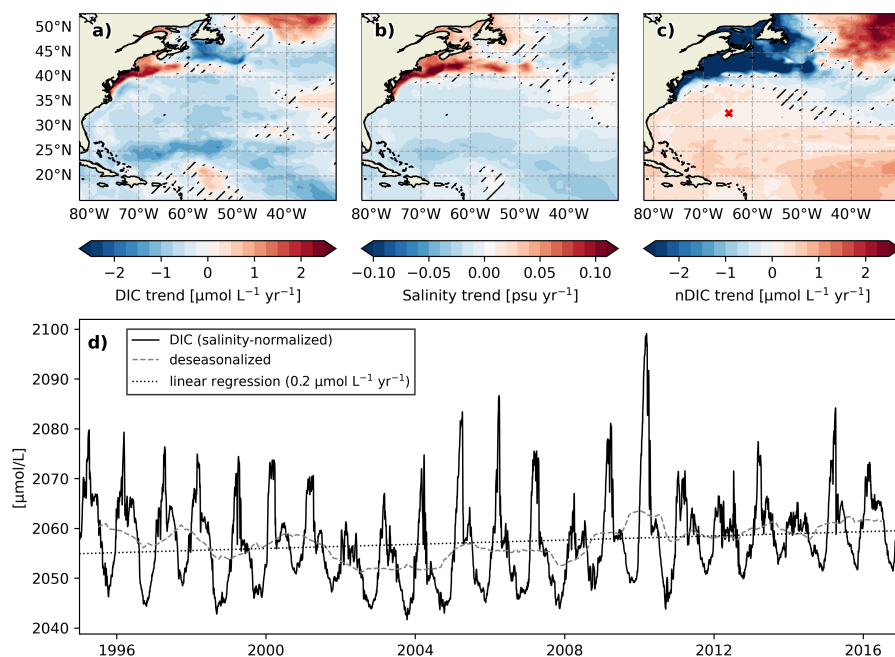


**Figure S12.** (a-c) Model trends between 1995 and 2017 at 10 m depth for (a) DIC, (b) salinity, and (c) nDIC. Hatched areas indicate trends that are not statistically significant ( $p > 0.05$ ). (d) Modeled nDIC concentration at 10 m depth at 32°42' N, 64°46' W, close to the BATS site (red X in (c)). All trends are computed after deseasonalization based on moving averages.

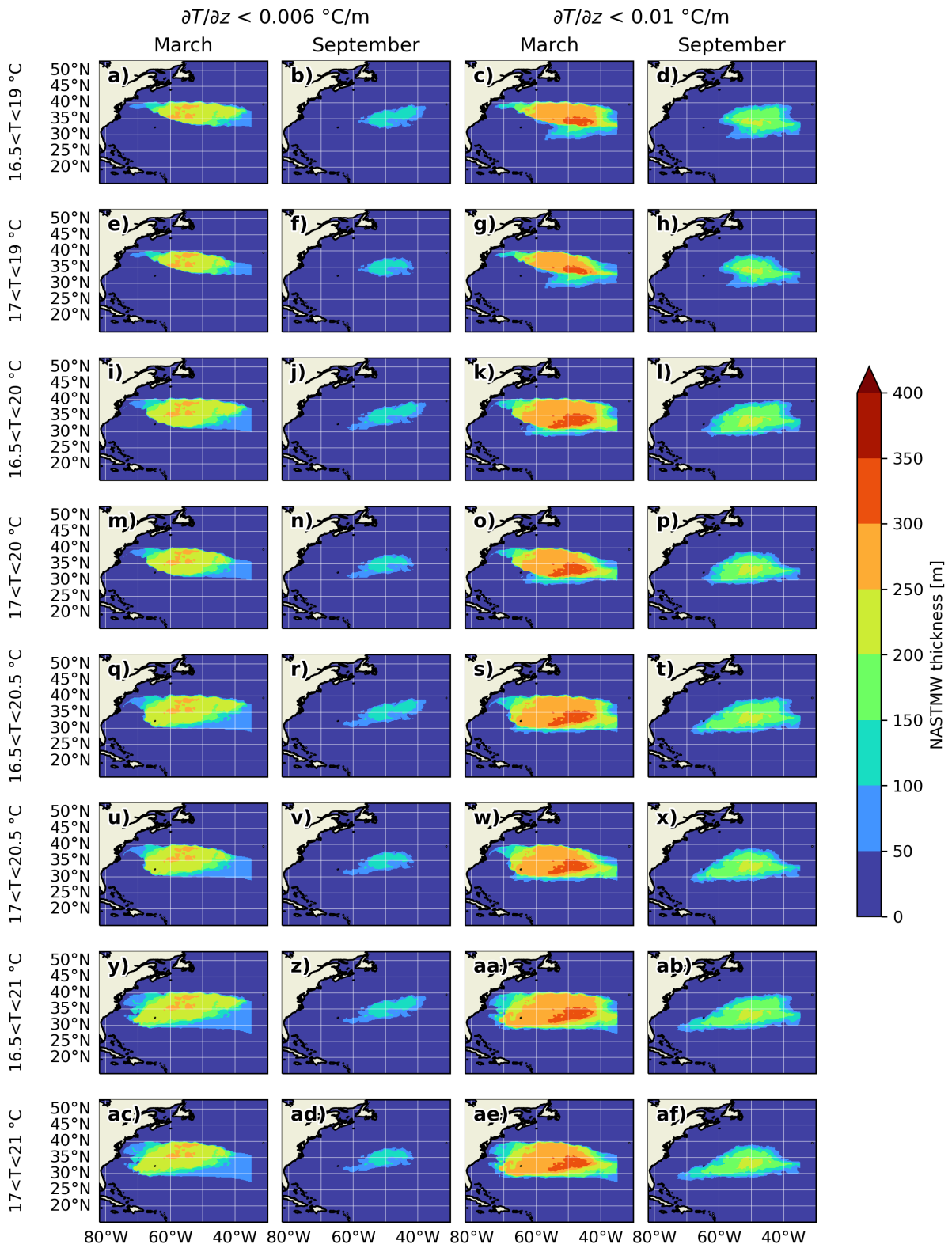


**Figure S13.** Model NASTMW thicknesses in March and September for different temperature and stratifications limits.

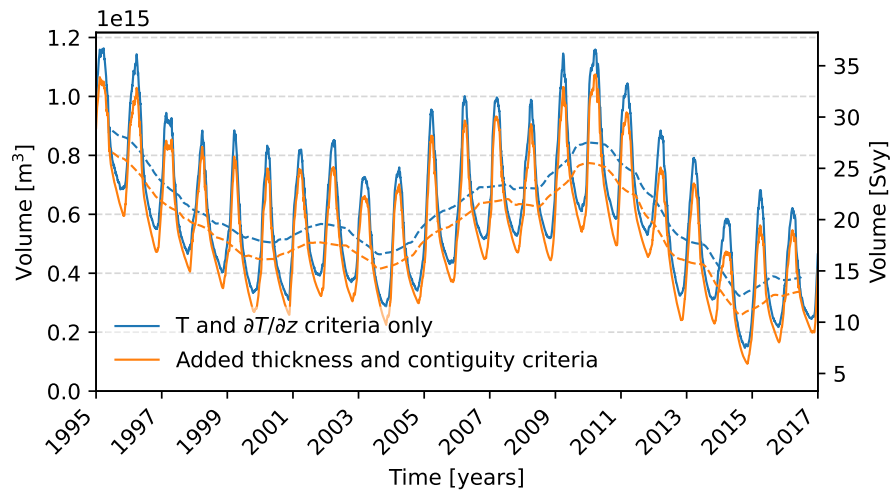


**Figure S14.** Modeled NASTMW volume with the definition criteria from section 2.2 of the main text. Dashed lines represent yearly averages.

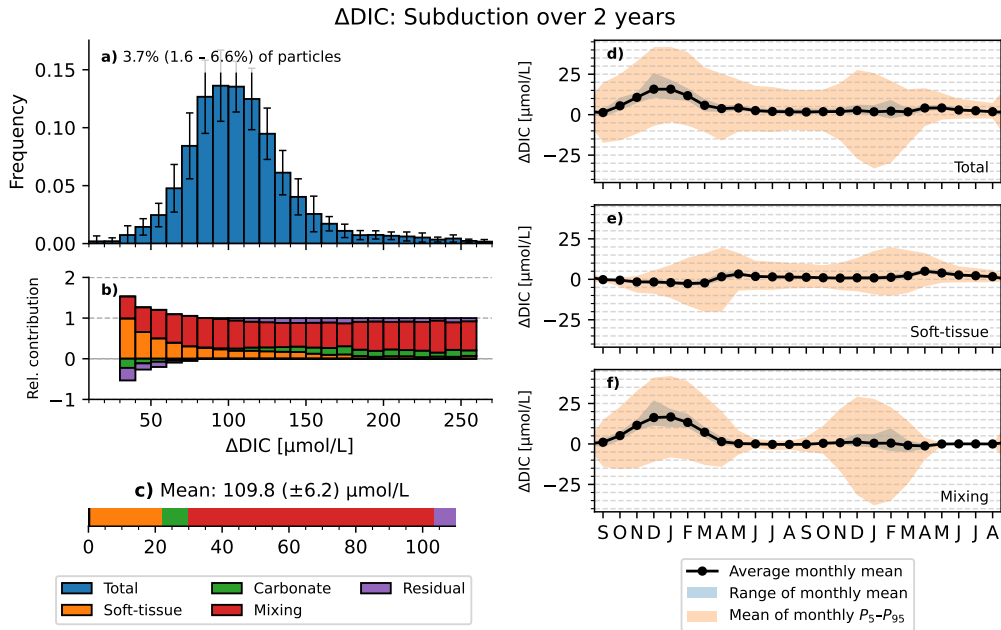


**Figure S15.** Transformation of DIC concentrations along pathways of subducting NASTMW parcels (allowing subduction to take place over the course of 2 years). (a) Distribution of total  $\Delta\text{DIC}$  per trajectory, averaged over initialization years 1996-2015. (b) Relative contribution of each process to the average  $\Delta\text{DIC}$ , for different  $\Delta\text{DIC}$  strengths. (c) Mean of yearly average  $\Delta\text{DIC}$  of all trajectories. (d-f) Mean monthly integrated DIC changes averaged across years for the total DIC rate of change (d), soft-tissue processes (e), and mixing fluxes (f).

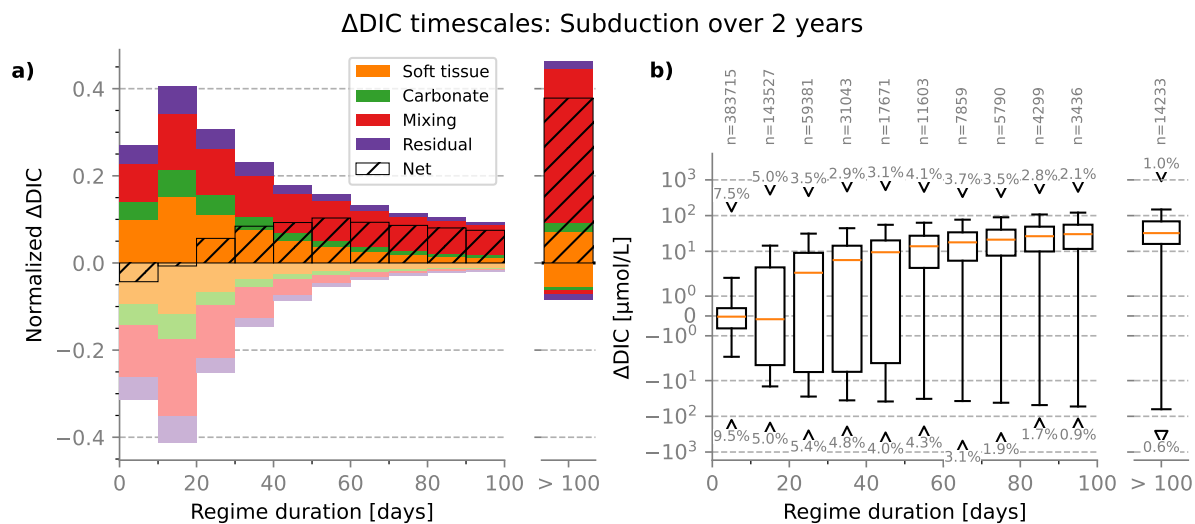


**Figure S16.**  $\Delta$ DIC contribution of each timescale for subducting NASTMW parcels (allowing subduction to take place over the course of 2 years). (a) Relative  $\Delta$ DIC of regimes of each timescale. (b) Boxplot of magnitudes of each regime for each timescale.

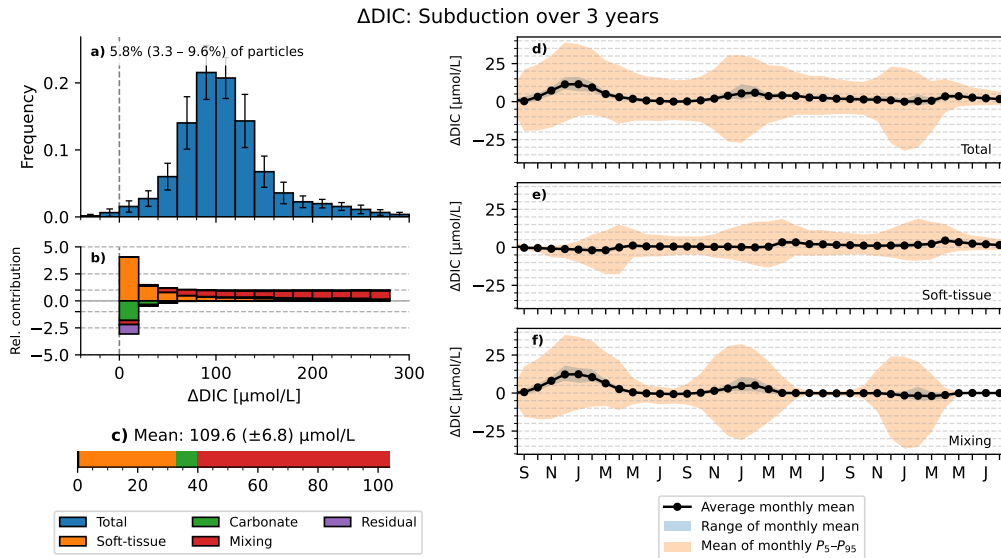


**Figure S17.** Transformation of DIC concentrations along pathways of subducting NASTMW parcels (allowing subduction to take place over the course of 3 years). (a) Distribution of total  $\Delta$ DIC per trajectory, averaged over initialization years 1996-2015. (b) Relative contribution of each process to the average  $\Delta$ DIC, for different  $\Delta$ DIC strengths. (c) Mean of yearly average  $\Delta$ DIC of all trajectories. (d-f) Mean monthly integrated DIC changes averaged across years for the total DIC rate of change (d), soft-tissue processes (e), and mixing fluxes (f).

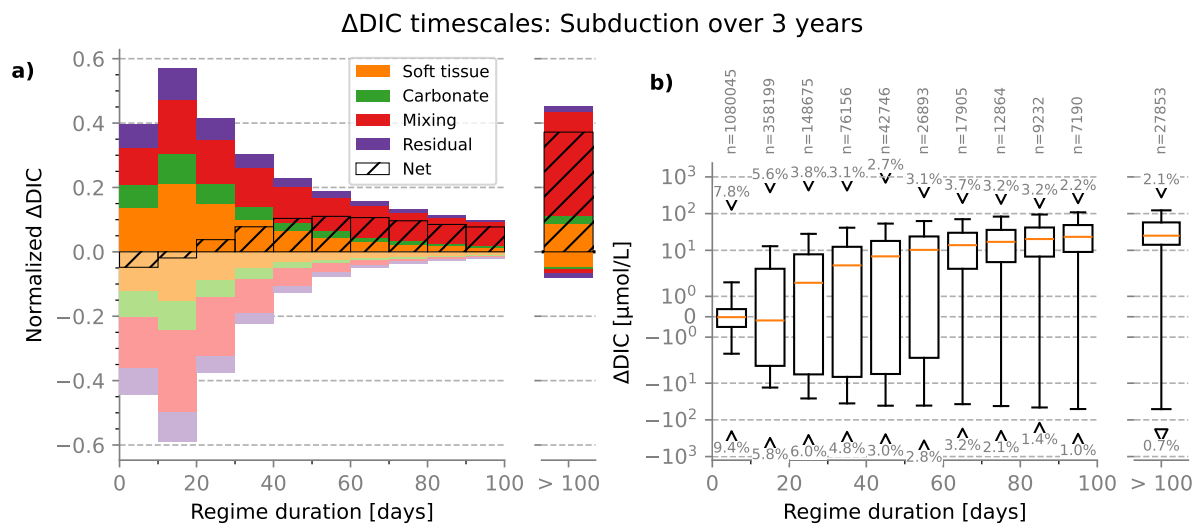


**Figure S18.**  $\Delta$ DIC contribution of each timescale for subducting NASTMW parcels (allowing subduction to take place over the course of 3 years). (a) Relative  $\Delta$ DIC of regimes of each timescale. (b) Boxplot of magnitudes of each regime for each timescale.

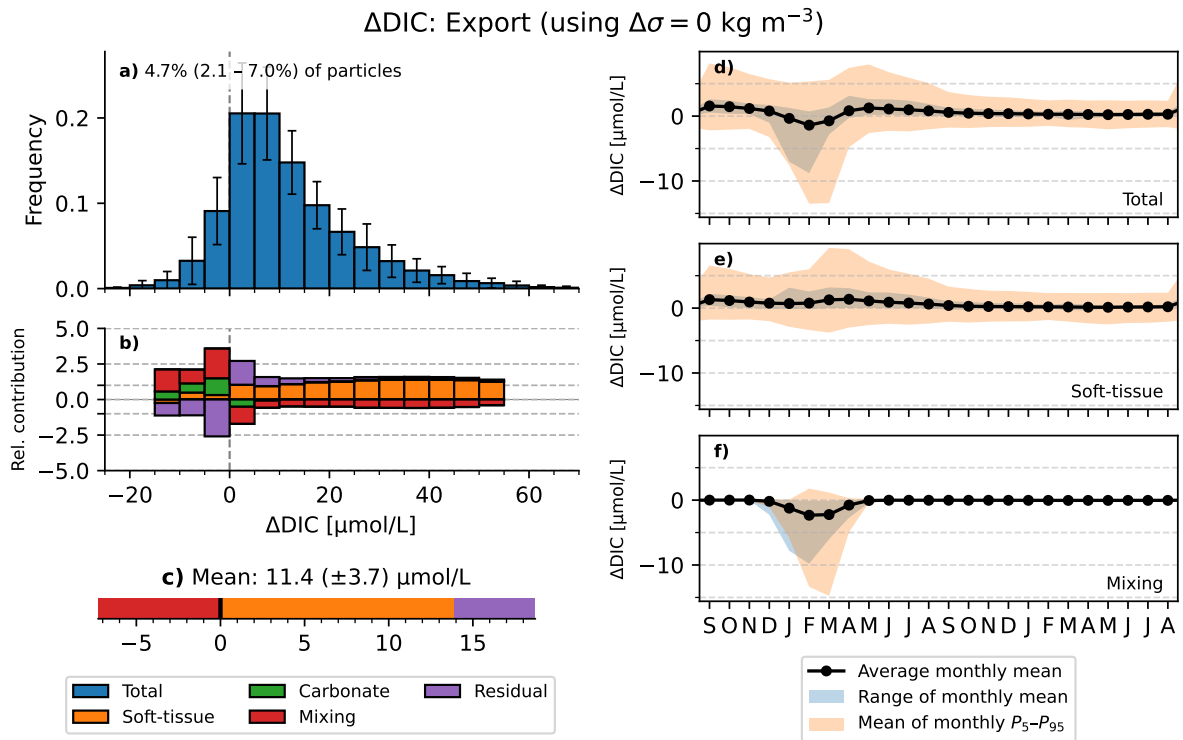


**Figure S19.** Transformation of DIC concentrations along pathways of exported NASTMW parcels, for  $\Delta\sigma = 0 \text{ kg m}^{-3}$ . (a) Distribution of total  $\Delta\text{DIC}$  per trajectory, averaged over initialization years 1995-2015. (b) Relative contribution of each process to the average  $\Delta\text{DIC}$ , for different  $\Delta\text{DIC}$  strengths. (c) Mean of yearly average  $\Delta\text{DIC}$  of all trajectories. (d-f) Mean monthly integrated DIC changes averaged across years for the total DIC rate of change (d), soft-tissue processes (e), and mixing fluxes (f).

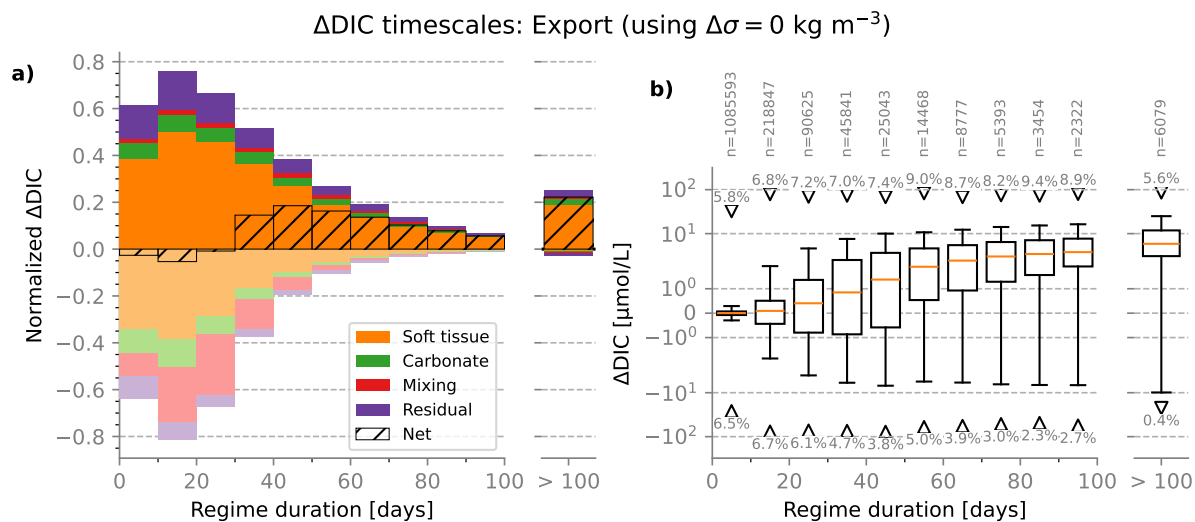


**Figure S20.**  $\Delta$ DIC contribution of each timescale for exported NASTMW parcels for  $\Delta\sigma = 0 \text{ kg m}^{-3}$ . (a) Relative  $\Delta$ DIC of regimes of each timescale. (b) Boxplot of magnitudes of each regime for each timescale.

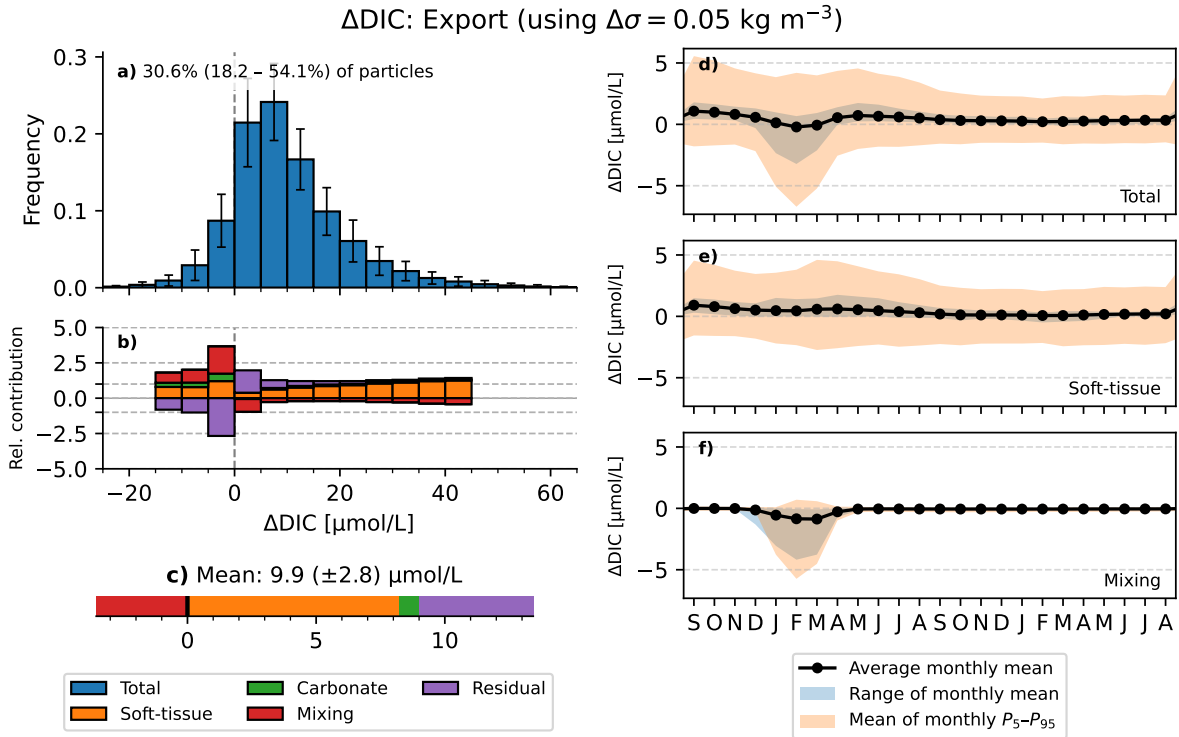


**Figure S21.** Transformation of DIC concentrations along pathways of exported NASTMW parcels for  $\Delta\sigma = 0.05 \text{ kg m}^{-3}$ . (a) Distribution of total  $\Delta$ DIC per trajectory, averaged over initialization years 1995-2015. (b) Relative contribution of each process to the average  $\Delta$ DIC, for different  $\Delta$ DIC strengths. (c) Mean of yearly average  $\Delta$ DIC of all trajectories. (d-f) Mean monthly integrated DIC changes averaged across years for the total DIC rate of change (d), soft-tissue processes (e), and mixing fluxes (f).

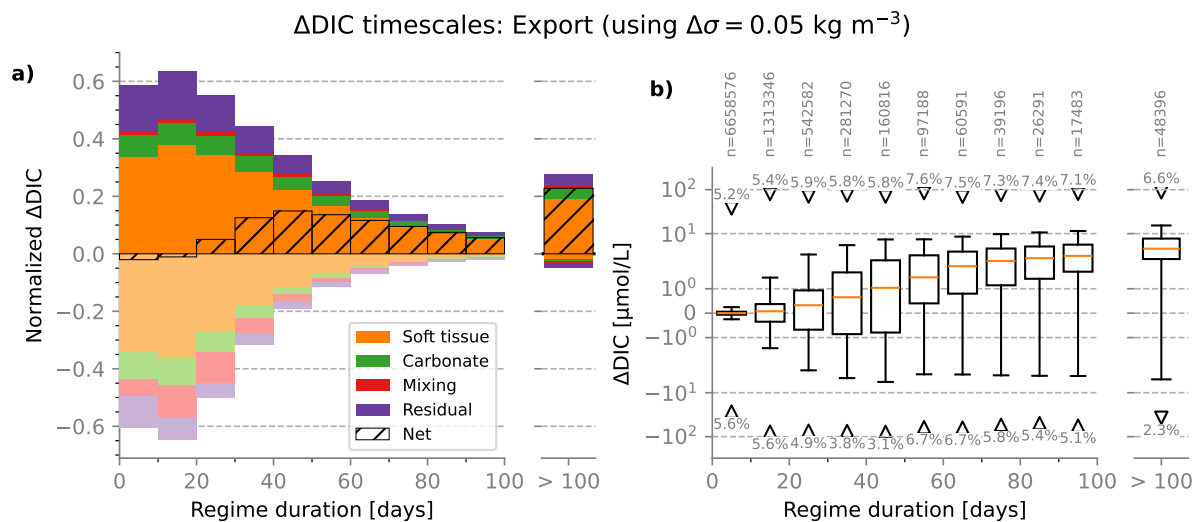


**Figure S22.**  $\Delta$ DIC contribution of each timescale for exported NASTMW parcels, for  $\Delta\sigma = 0.05 \text{ kg m}^{-3}$ . (a) Relative  $\Delta$ DIC of regimes of each timescale. (b) Boxplot of magnitudes of each regime for each timescale.

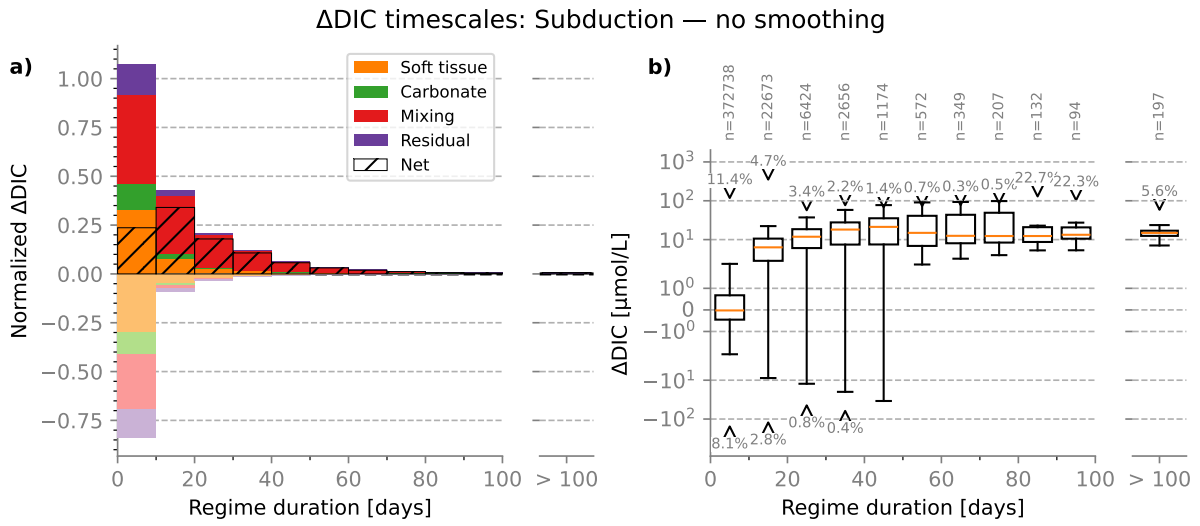


**Figure S23.**  $\Delta$ DIC contribution of each timescale for subducting NASTMW parcels, found without applying a smoothing window. (a) Relative  $\Delta$ DIC of regimes of each timescale. (b) Boxplot of magnitudes of each regime for each timescale.

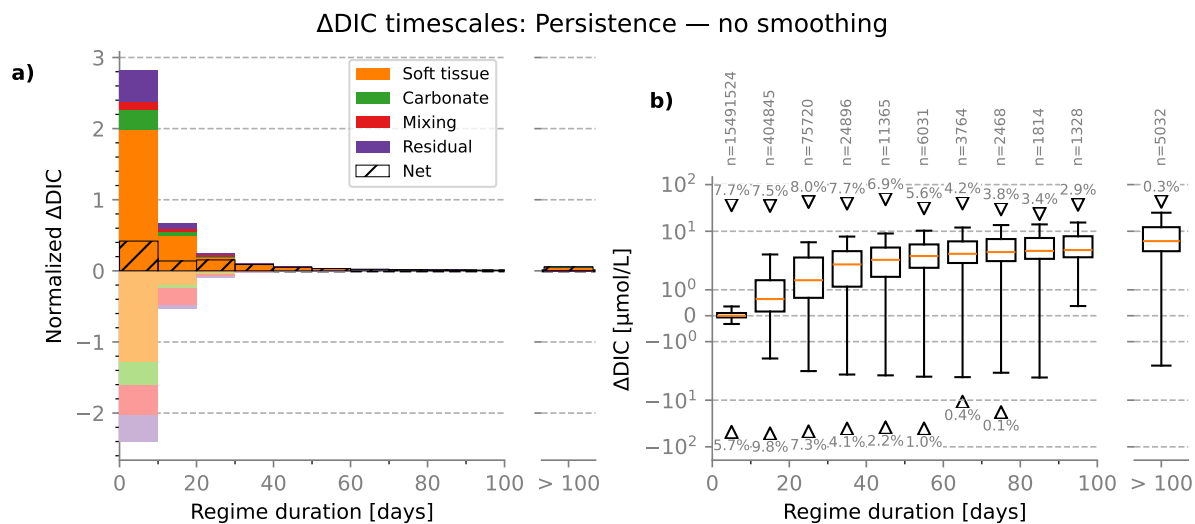


**Figure S24.**  $\Delta$ DIC contribution of each timescale for persisting NASTMW parcels, found without applying a smoothing window. (a) Relative  $\Delta$ DIC of regimes of each timescale. (b) Boxplot of magnitudes of each regime for each timescale.

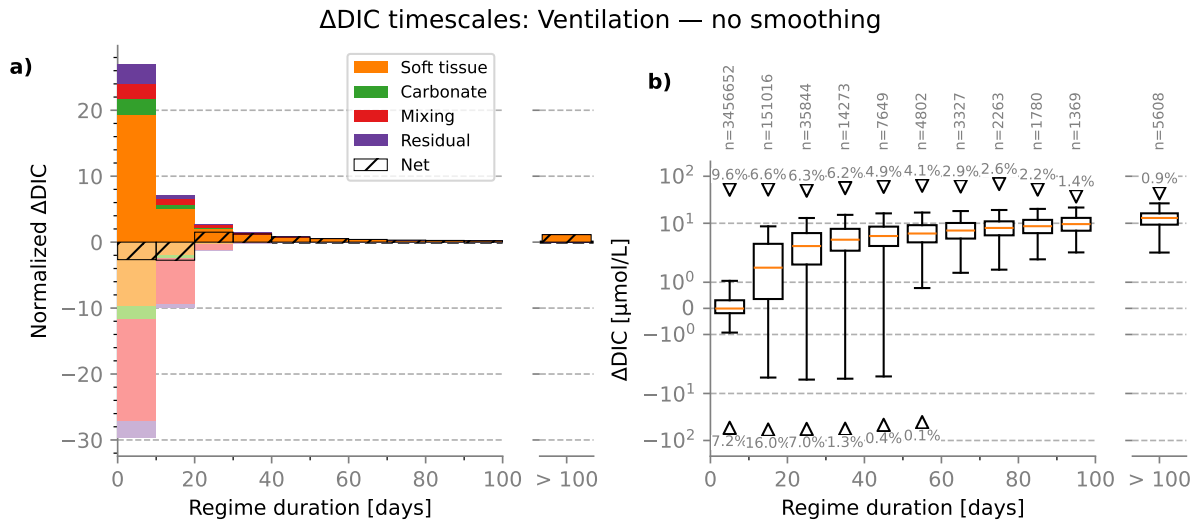


**Figure S25.**  $\Delta$ DIC contribution of each timescale for ventilating NASTMW parcels, found without applying a smoothing window. (a) Relative  $\Delta$ DIC of regimes of each timescale. (b) Boxplot of magnitudes of each regime for each timescale.

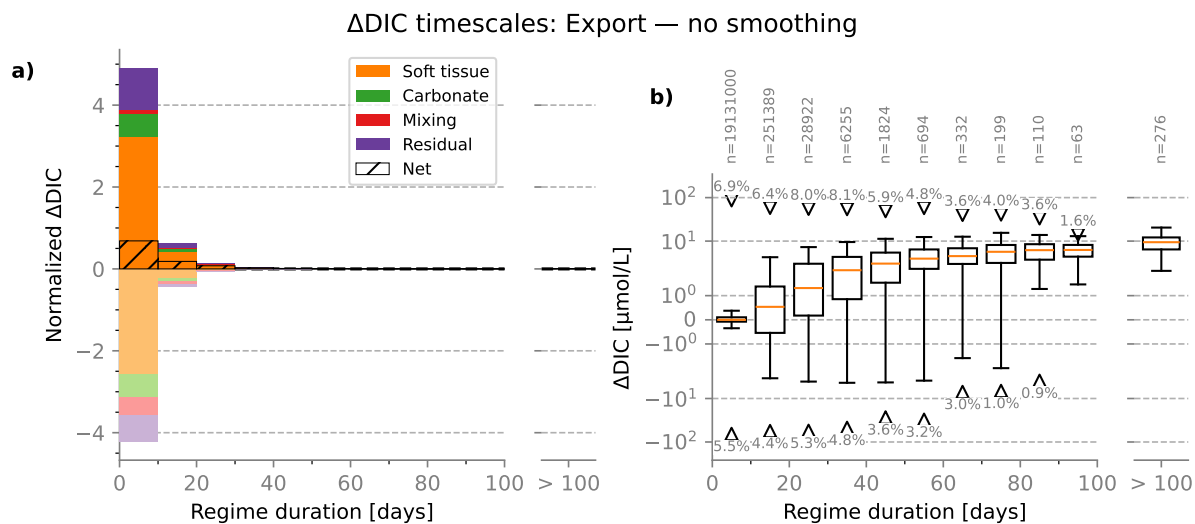


**Figure S26.**  $\Delta$ DIC contribution of each timescale for exporting NASTMW parcels, found without applying a smoothing window. (a) Relative  $\Delta$ DIC of regimes of each timescale. (b) Boxplot of magnitudes of each regime for each timescale.

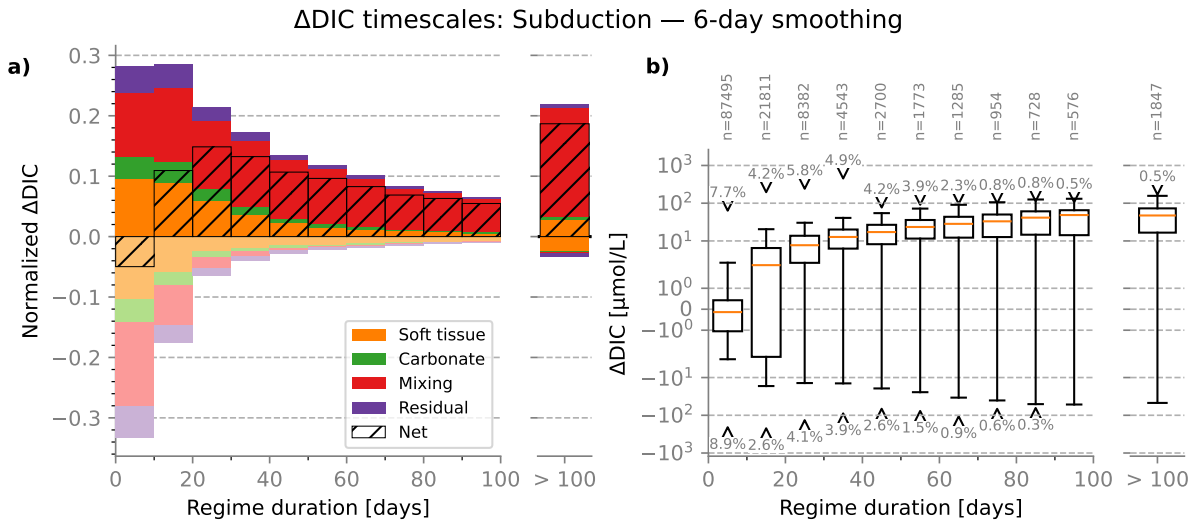


**Figure S27.**  $\Delta$ DIC contribution of each timescale for subducting NASTMW parcels, found when applying a 6-day smoothing window. (a) Relative  $\Delta$ DIC of regimes of each timescale. (b) Boxplot of magnitudes of each regime for each timescale.

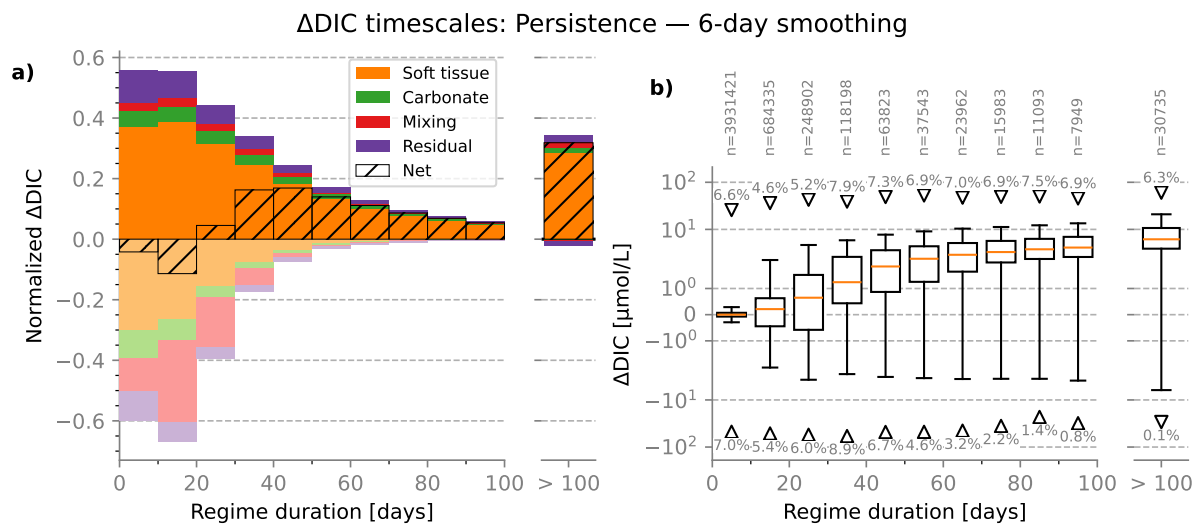


**Figure S28.**  $\Delta$ DIC contribution of each timescale for persisting NASTMW parcels, found when applying a 6-day smoothing window. (a) Relative  $\Delta$ DIC of regimes of each timescale. (b) Boxplot of magnitudes of each regime for each timescale.

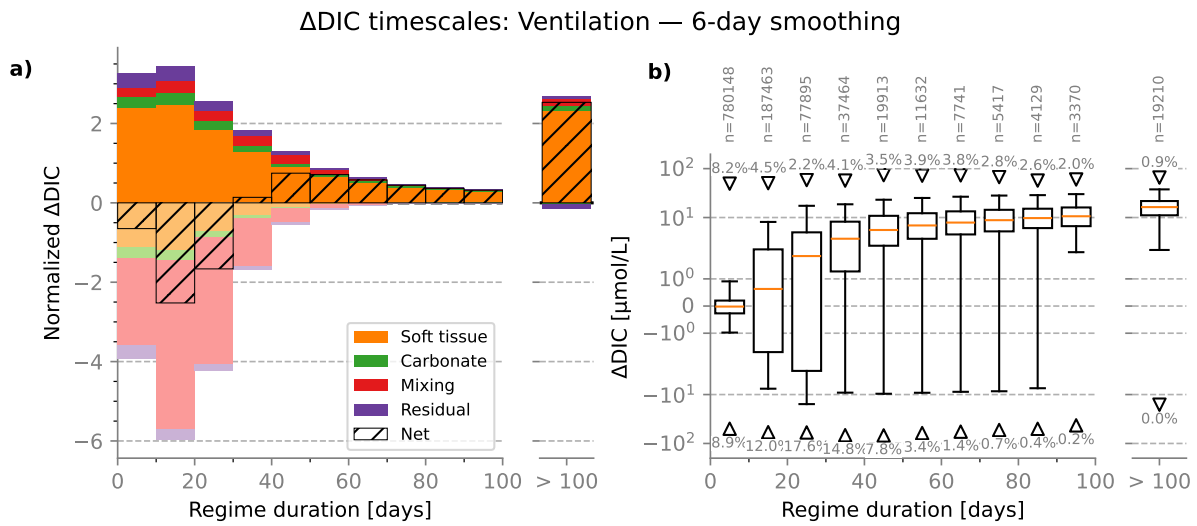


**Figure S29.**  $\Delta$ DIC contribution of each timescale for ventilating NASTMW parcels, found when applying a 6-day smoothing window. (a) Relative  $\Delta$ DIC of regimes of each timescale. (b) Boxplot of magnitudes of each regime for each timescale.

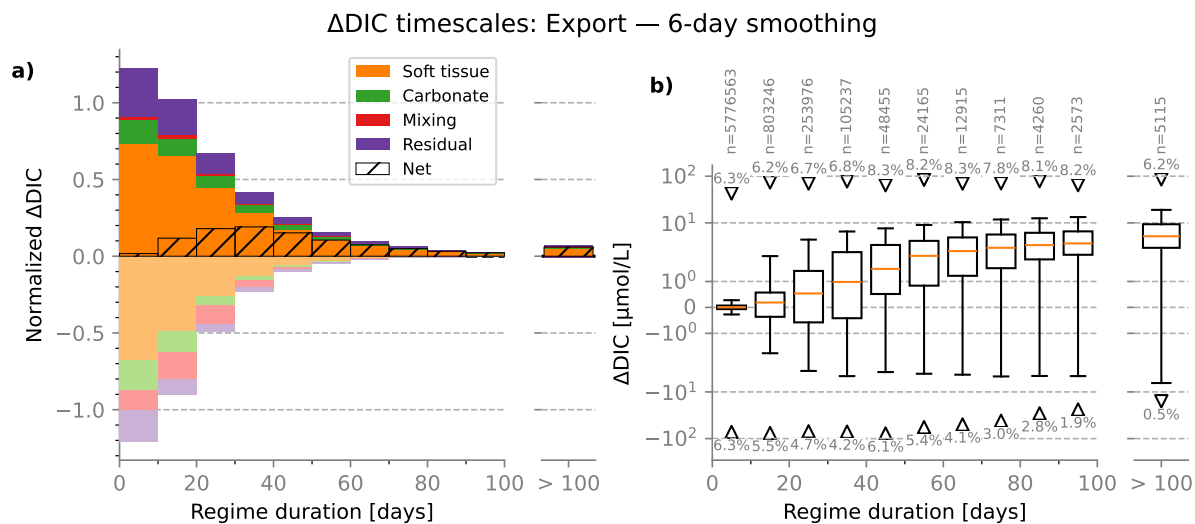


**Figure S30.**  $\Delta$ DIC contribution of each timescale for exporting NASTMW parcels, found when applying a 6-day smoothing window. (a) Relative  $\Delta$ DIC of regimes of each timescale. (b) Boxplot of magnitudes of each regime for each timescale.

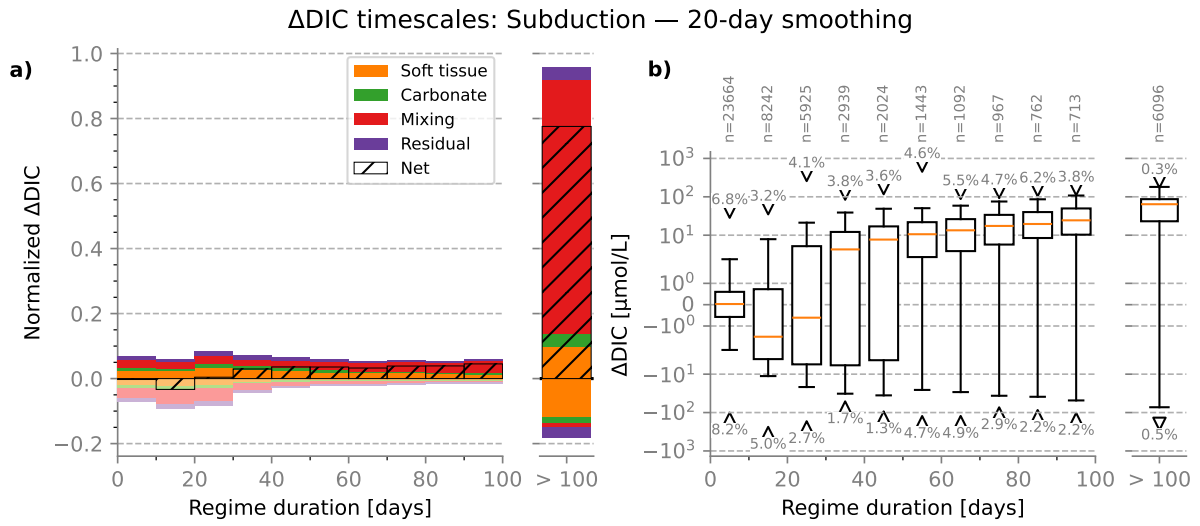


**Figure S31.**  $\Delta$ DIC contribution of each timescale for subducting NASTMW parcels, found when applying a 20-day smoothing window. (a) Relative  $\Delta$ DIC of regimes of each timescale. (b) Boxplot of magnitudes of each regime for each timescale.

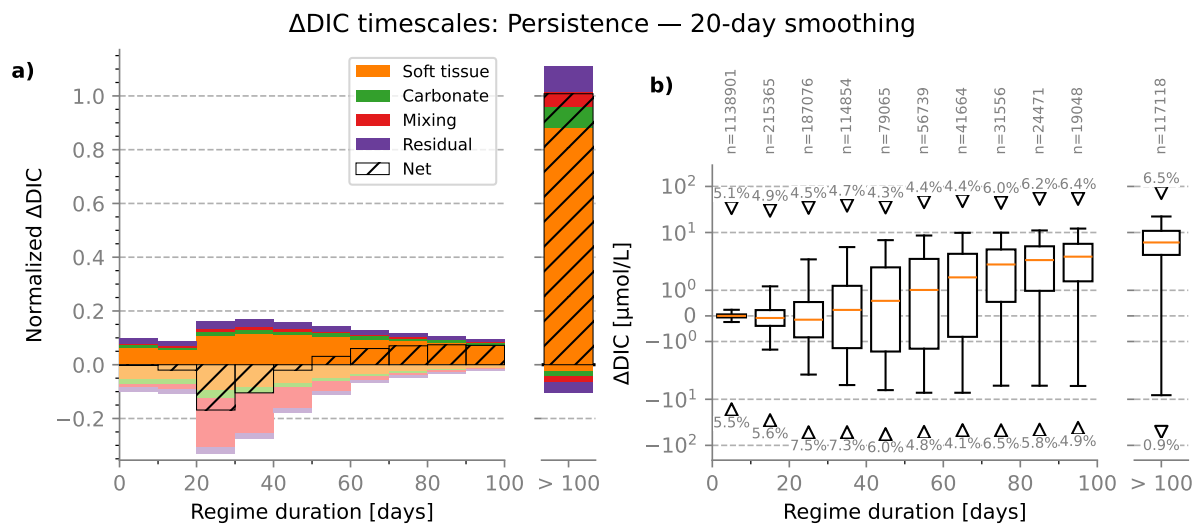


**Figure S32.**  $\Delta$ DIC contribution of each timescale for persisting NASTMW parcels, found when applying a 20-day smoothing window. (a) Relative  $\Delta$ DIC of regimes of each timescale. (b) Boxplot of magnitudes of each regime for each timescale.

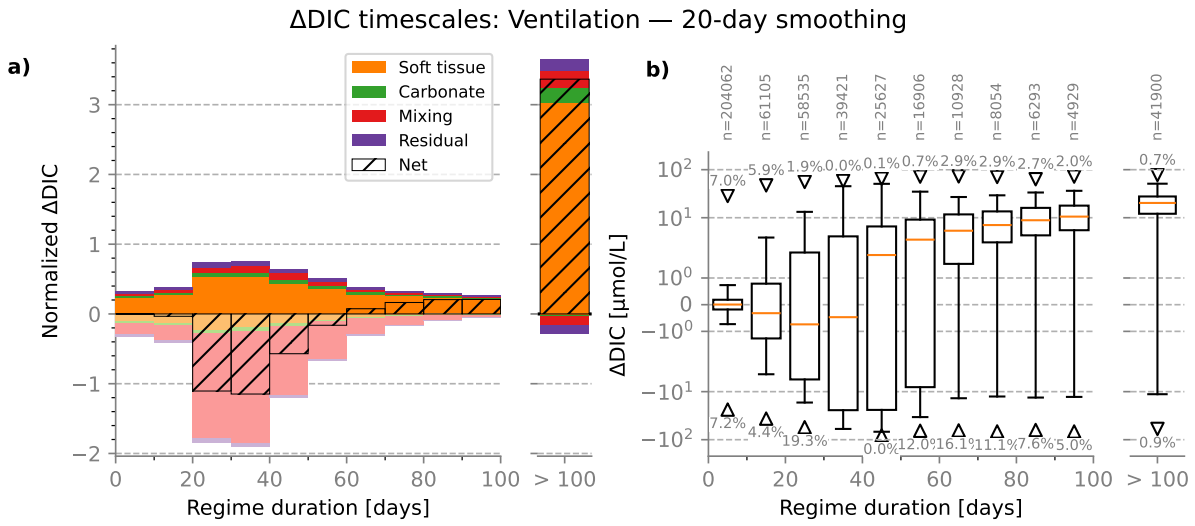


**Figure S33.** ΔDIC contribution of each timescale for ventilating NASTMW parcels, found when applying a 20-day smoothing window. (a) Relative ΔDIC of regimes of each timescale. (b) Boxplot of magnitudes of each regime for each timescale.

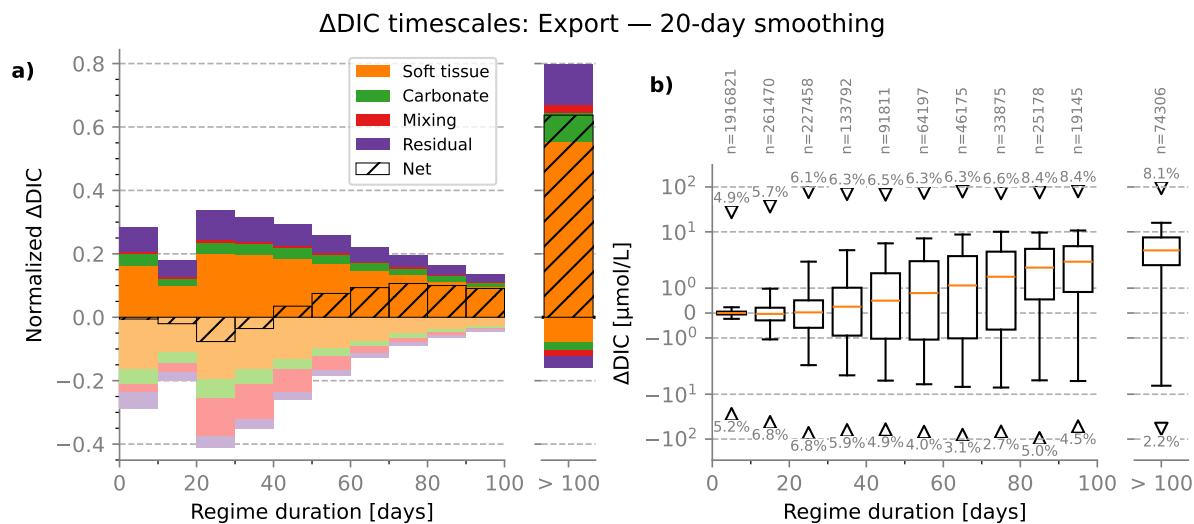


**Figure S34.**  $\Delta$ DIC contribution of each timescale for exporting NASTMW parcels, found when applying a 20-day smoothing window. (a) Relative  $\Delta$ DIC of regimes of each timescale. (b) Boxplot of magnitudes of each regime for each timescale.

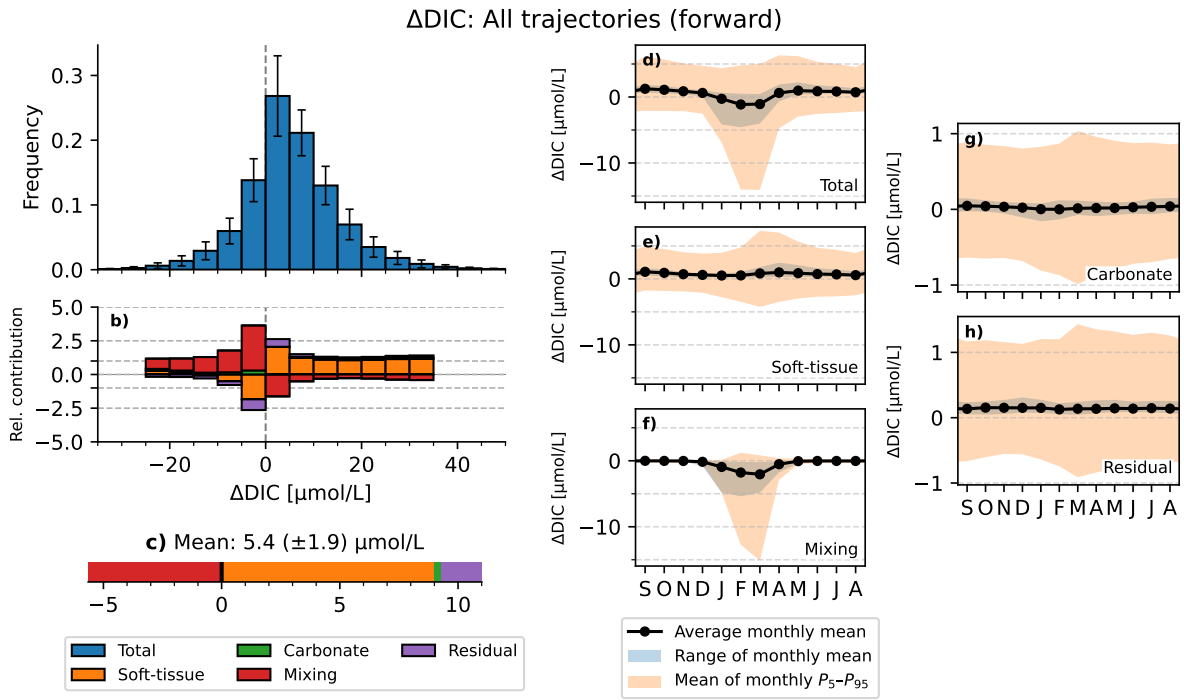


**Figure S35.** Transformation of DIC concentrations along all forward trajectories starting in NASTMW. (a) Distribution of total  $\Delta$ DIC per trajectory, averaged over initialization years 1995-2015. (b) Relative contribution of each process to the average  $\Delta$ DIC, for different  $\Delta$ DIC strengths. (c) Mean of yearly average  $\Delta$ DIC of all trajectories. (d-f) Mean monthly integrated DIC changes averaged across years for the total DIC rate of change (d), soft-tissue processes (e), mixing fluxes (f), carbonate processes (g), and residual terms (h).

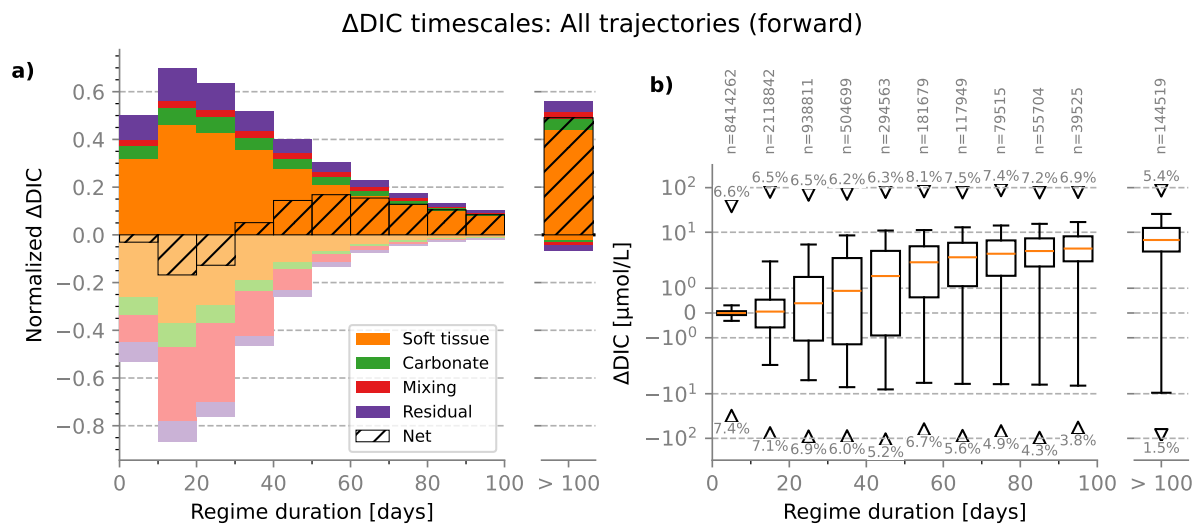


**Figure S36.**  $\Delta$ DIC contribution of each timescale for all forward trajectories starting in NASTMW. (a) Relative  $\Delta$ DIC of regimes of each timescale. (b) Boxplot of magnitudes of each regime for each timescale.

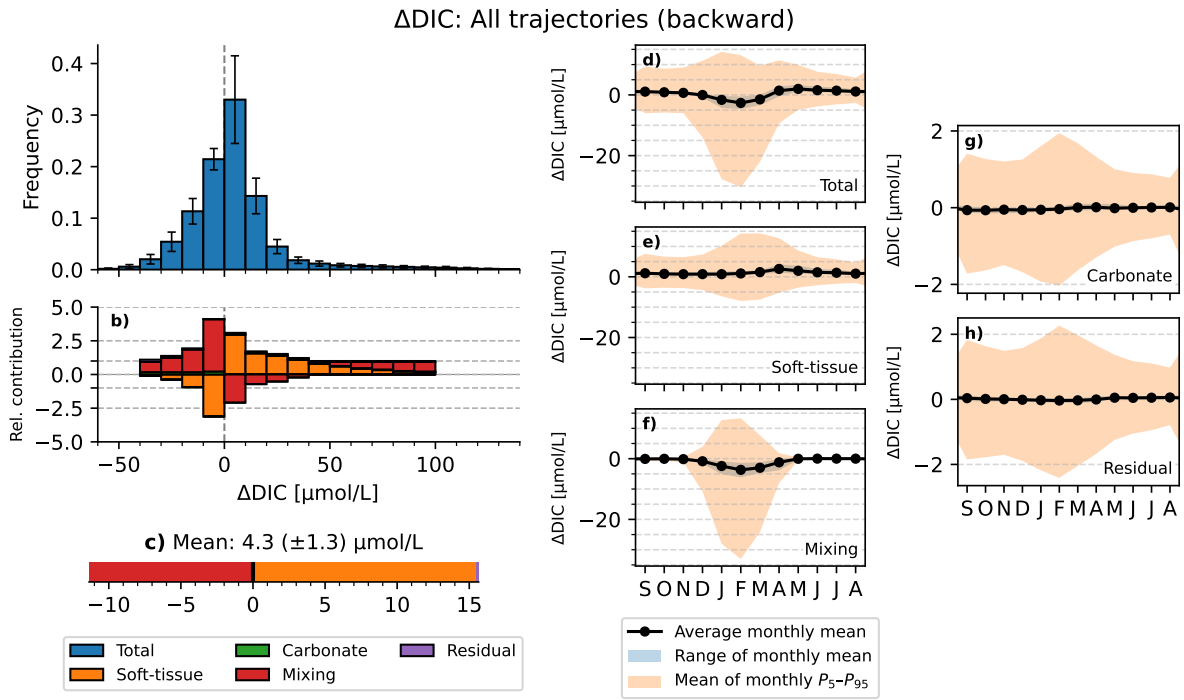


**Figure S37.** Transformation of DIC concentrations along all backward trajectories ending in NASTMW. (a) Distribution of total ΔDIC per trajectory, averaged over initialization years 1995-2015. (b) Relative contribution of each process to the average ΔDIC, for different ΔDIC strengths. (c) Mean of yearly average ΔDIC of all trajectories. (d-f) Mean monthly integrated DIC changes averaged across years for the total DIC rate of change (d), soft-tissue processes (e), mixing fluxes (f), carbonate processes (g), and residual terms (h).

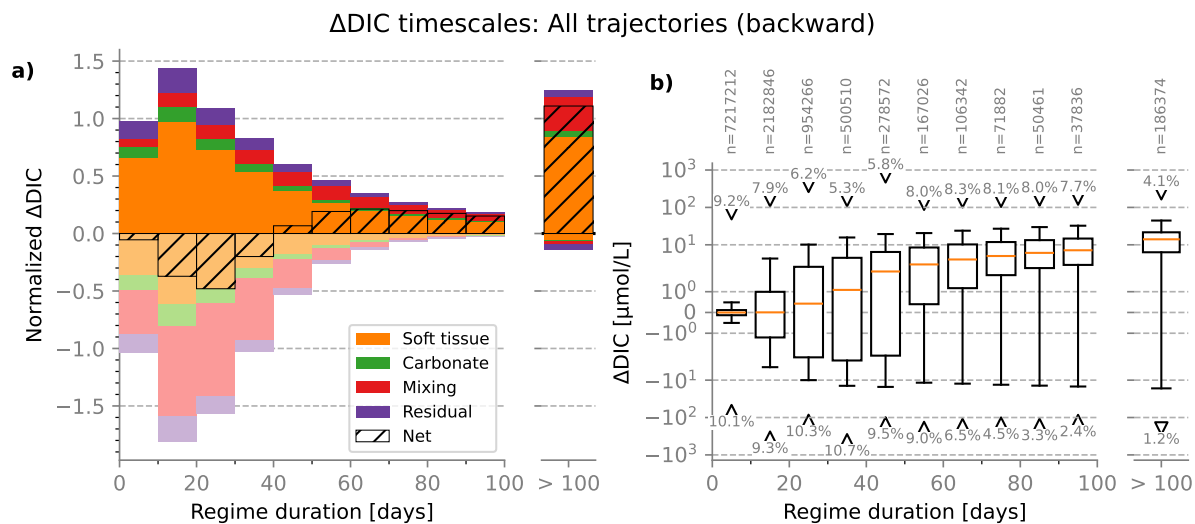


**Figure S38.**  $\Delta$ DIC contribution of each timescale for all backward trajectories ending in NASTMW. (a) Relative  $\Delta$ DIC of regimes of each timescale. (b) Boxplot of magnitudes of each regime for each timescale.

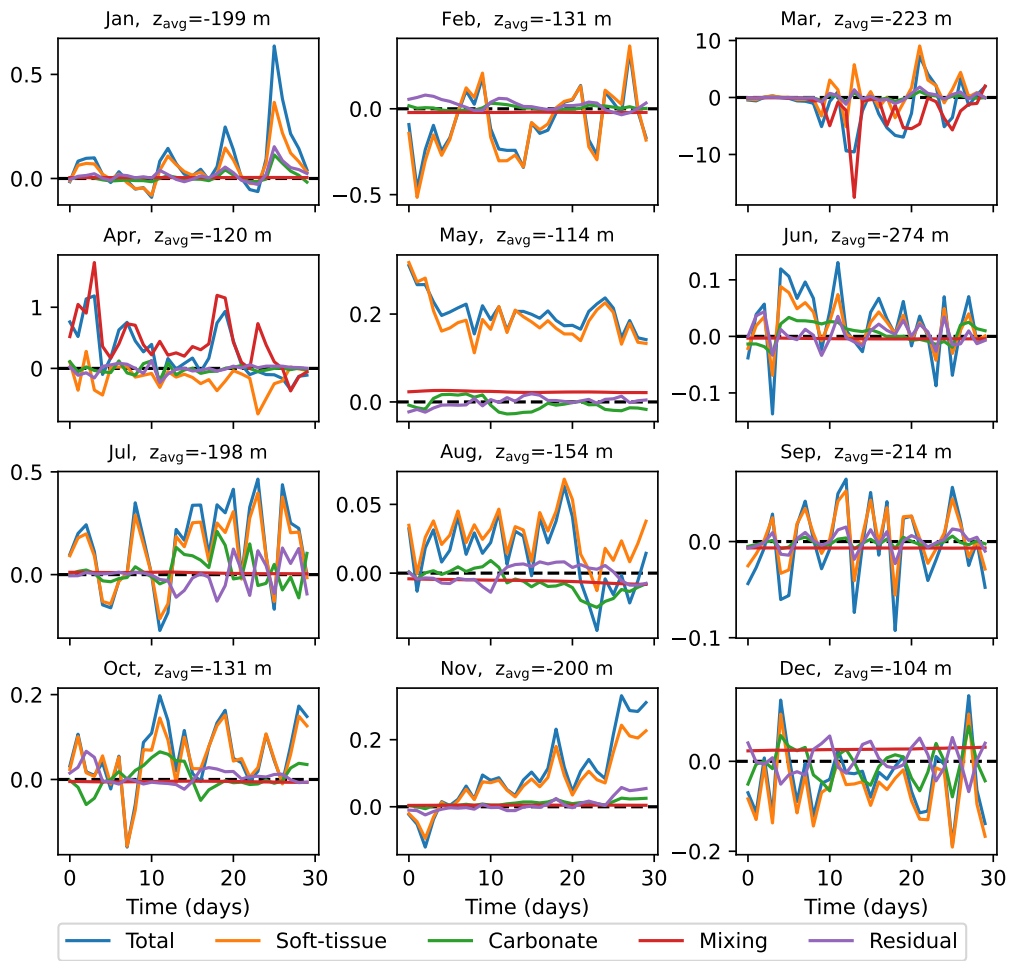


**Figure S39.** Daily DIC rates of change [ $\mu\text{mol L}^{-1} \text{d}^{-1}$ ] for 12 random trajectories in 12 months, from parcels that were initialized in September 2000. The soft-tissue term often dominates the signal, while the vertical mixing term is mainly relevant in when the parcel is in the mixing layer.

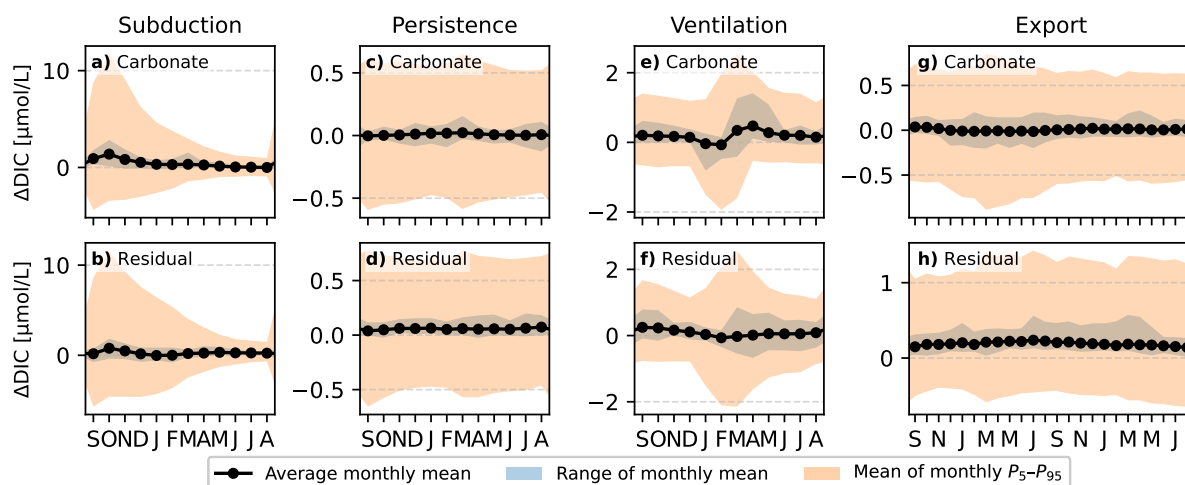


**Figure S40.** Yearly mean of the integrated DIC rate of change for carbonate and residual processes, integrated per month, as well as the range of the yearly mean, and the mean of the 5th and 95th percentile for the four NASTMW pathways discussed in the main text: (a, b) subduction, (c, d) persistence, (e, f) ventilation, and (g, h) export.

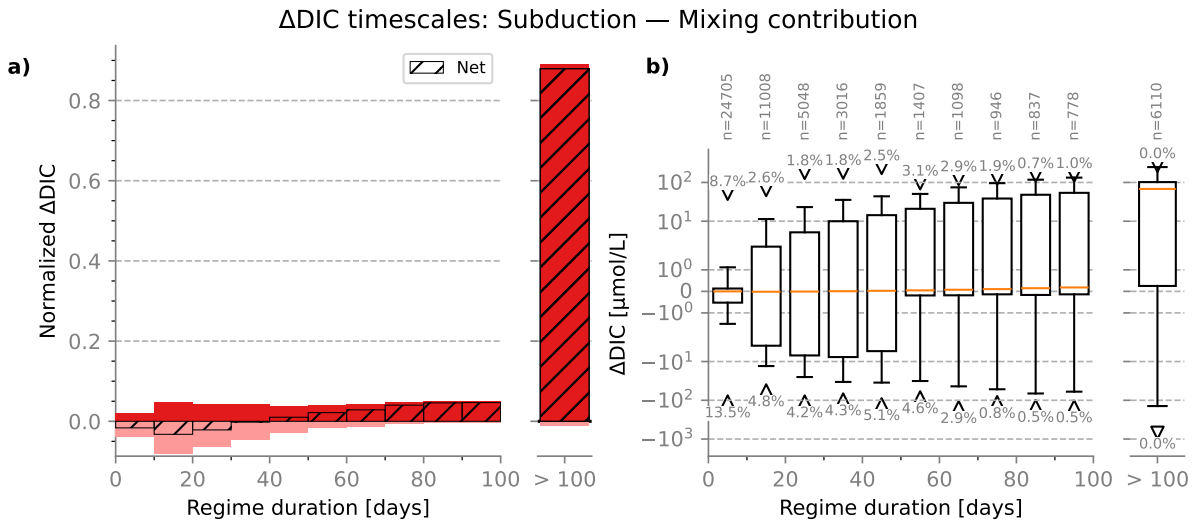


**Figure S41.**  $\Delta$ DIC contribution of each timescale for subducting NASTMW based on DIC anomalies from mixing processes. (a) Relative  $\Delta$ DIC of regimes of each timescale. (b) Boxplot of magnitudes of each regime for each timescale.

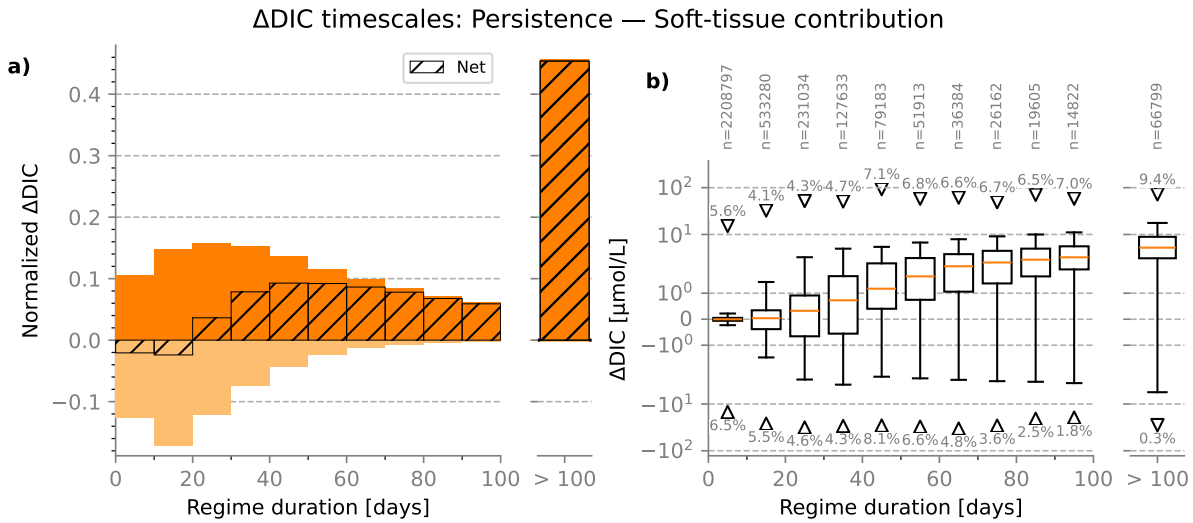


**Figure S42.**  $\Delta$ DIC contribution of each timescale for parcels persisting in NASTMW, based on DIC anomalies from soft-tissue processes. (a) Relative  $\Delta$ DIC of regimes of each timescale. (b) Boxplot of magnitudes of each regime for each timescale.

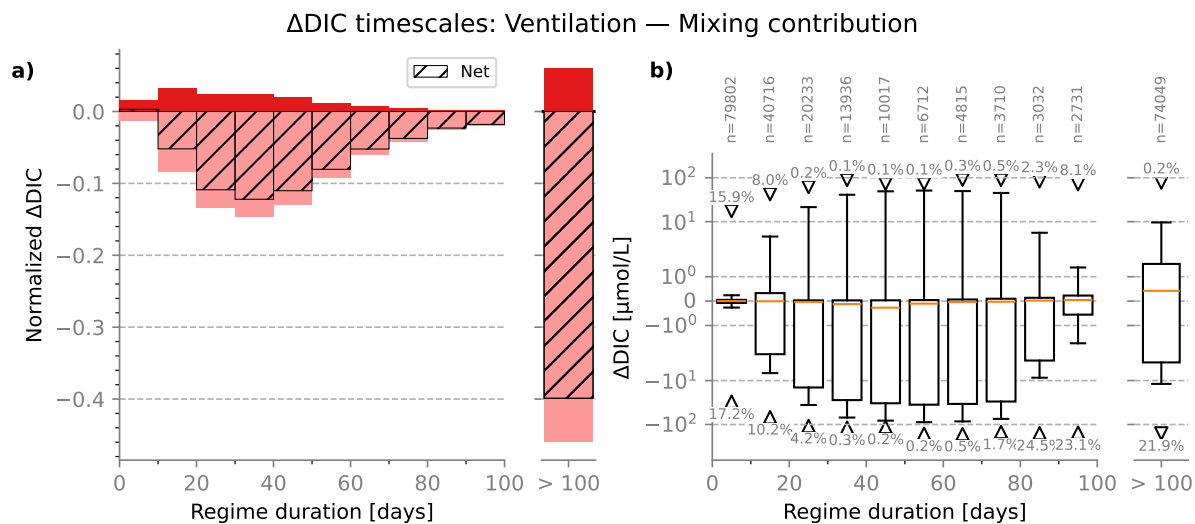


**Figure S43.**  $\Delta$ DIC contribution of each timescale for ventilating NASTMW based on DIC anomalies from mixing processes. (a) Relative  $\Delta$ DIC of regimes of each timescale. (b) Boxplot of magnitudes of each regime for each timescale.